ALMA MATER STUDIORUM - UNIVERSITÀ DI BOLOGNA
CAMPUS DI CESENA
SCUOLA DI INGEGNERIA E ARCHITETTURA

CORSO DI LAUREA MAGISTRALE IN INGEGNERIA BIOMEDICA

Elucidating the phenotypic variability of a single cardiac sodium channel mutation: a multiscale computational approach

Tesi in

Bioingegneria Molecolare e Cellulare LM

Relatore:
Prof. Stefano Severi
Co-relatori:
Dr. Xin Zhou
Dr. Alfonso Bueno-Orovio

Presentata da:
Francesca Margara

Anno Accademico 2016/2017

for
the arms
that hold me
(Rupi Kaur)

Acknowledgements

I would like to thank my supervisors, Prof. Stefano Severi, Dr. Alfonso Bueno-Orovio, and Dr. Xin Zhou for all their support and guidance throughout the work of my thesis. I want to thank Prof. Stefano Severi for inspiring my interest and passion on the fascinating world of Computational Cardiology. I want to thank Alfonso for guiding me during this work and sharing with me his immense knowledge with constant positivity. I would like to give special thanks to Xin for her valuable input and suggestions, and especially for being always ready to help me and listening to my questions. I also want to thank Prof. Blanca Rodriguez and everyone in the Computational Cardiovascular Science group, it has been (and it will be) a pleasure being part of your research group. Thanks a lot for welcoming me with open arms from the first day!

I want to acknowledge the clinical collaborators from the Department of Experimental Cardiology, University of Amsterdam. In particular, Dr. Carol Ann Remme for providing the clinical data for my work.

Abstract

Descritta per la prima volta nel 1999, la mutazione *SCN5A-1795insD* compromette l'inattivazione veloce della corrente del sodio e ne riduce drasticamente il picco. Ciò si riflette a livello macroscopico in una insolita combinazione di sintomi tipici delle sindromi long-QT di tipo 3 e Brugada. Nonostante i notevoli progressi, si registrano ancora numerose questioni irrisolte relative sia agli aspetti genetici e biofisici di questa condizione, sia alla variabilità fenotipica attraverso cui questa patologia si manifesta.

Utilizzando un approccio computazionale e multi-scala abbiamo acquisito una conoscenza più approfondita circa questa condizione potenzialmente mortale. Partendo dalla versione aggiornata del modello di elettrofisiologia cellulare O'Hara-Rudy dynamic (ORd) e sfruttando la metodologia delle popolazioni di modelli, abbiamo costruito quattro popolazioni di cellule e due popolazioni di fibre rappresentanti soggetti sani e malati, incorporando nella modellazione dati sperimentali e clinici.

I risultati delle simulazioni riproducono la variabilità fenotipica di questa patologia, evidenziando difetti di conduzione e ripolarizzazione. Tali risultati sottolineano il ruolo della componente veloce della corrente di sodio nel sostenere la conduzione in tessuto. Dall'analisi dei coefficienti di correlazione parziale si evince che entrambe le componenti della corrente di sodio, lenta e veloce, sono fondamentali nel determinare il prolungamento dell'intervallo QT. Lo studio degli effetti transmurali della mutazione mostra una dispersione nella durata del potenziale d'azione che si riflette in tessuto attraverso una maggiore dispersione transmurale di ripolarizzazione (TDR). Tale TDR potrebbe rappresentare un nuovo biomarker per la diagnosi clinica di quei portatori della mutazione che altrimenti mostrerebbero biomarkers del tutto sovrapponibili a quelli di soggetti sani. Questo studio individua potenziali target terapeutici, supportando l'utilizzo di bloccanti della componente lenta della corrente di sodio per accorciare l'intervallo QT e ridurre la TDR, così come bloccanti della corrente transitoria uscente di potassio (I_{to}) per ripristinare la velocità di conduzione (CV). I risultati mostrano una potenziale inefficacia dei bloccanti della corrente di calcio. Questo studio fornisce inoltre evidenze in supporto alla teoria di depolarizzazione come meccanismo causale per la sindrome di Brugada, mostrando come la I_{to} sia principalmente coinvolta nel modulare la CV e il layer endocardico risulti essere il layer maggiormente affetto dalla mutazione. Infine, le analisi confermano il ruolo svolto dalla frequenza cardiaca nel prolungare l'intervallo QT nei pazienti portatori della mutazione.

Abstract

First described in 1999, the *SCN5A-1795insD* mutation disrupts sodium fast inactivation and drastically reduces the peak sodium current density. As a consequence, family members show a unique overlap of long-QT type 3 and Brugada syndromes. Up to date there are still multiple unresolved questions regarding the understanding of the genetic and biophysical aspects of cardiac sodium channelopathies. Moreover, there is a lack of knowledge concerning the phenotypic variability observed in patients carrying *SCN5A* gene related mutations.

Using a multi-scale computational approach, we derived further insights into this type of high risk life-threatening disease. Starting from the most updated version of the O'Hara-Rudy dynamic (*ORd*) model, we built four single cell populations and two populations of fibres in both healthy and mutation-carrier conditions, incorporating information from experimental and clinical data.

Simulation studies at the single cell and tissue levels recapitulated the phenotypic manifestations of the disease and its population variability. We highlighted the key role of the fast sodium current in sustaining a proper conduction in the fibre. From the PPC analysis between the model parameters and the tissue biomarkers we showed that the G_{NaL} and G_{Na} were the main responsible to prolong the QT interval. Combining the simulation results at the single cell and tissue levels we additionally gained further insights on the transmural effects of the mutation. We showed that this mutation produces an APD dispersion between the endocardial and epicardial layer, which is manifested in tissue through a more pronounced transmural dispersion of repolarisation (TDR). The TDR could constitute a novel and unique biomarker for the clinical diagnosis of mutation carriers, otherwise overlapping with the healthy population. We gained additional insights on therapeutic targets for this group of patients, supporting the use of late sodium current blockers to shorten the QT interval and to reduce the TDR, as well as the use of I_{to} blockers to improve the conduction velocity (CV). On the other hand, our understanding about L-type calcium current blockers suggests that their use might be less effective in these patients. We supplied further evidence in support of the depolarisation hypothesis as the causal mechanism of Brugada syndrome, showing that the I_{to} was mainly involved in modulating the CV and that the main electrophysiological manifestations of the mutation were reflected on the endocardial layer. In conclusion, our results further confirmed and explored the role of the heart rate in prolonging the QT interval of *SCN5A-1795insD* mutation carriers.

Contents

List of Figures

List of Tables

1 Introduction

Contents

1.1 Motivation

Mutations in the *SCN5A* gene cause cardiac sodium channel dysfunctions and may lead to arrhythmia syndromes, including long *QT* syndrome type 3 (*LQT3*), Brugada syndrome (*BrS*) and cardiac conduction disease.

Traditionally, in order to investigate the biophysical properties of mutant channels and correlate them to the clinical disease phenotype, heterologous expression systems have been frequently used and they have been very informative. Results from these cell lines have increased knowledge about the mutations, however those studies may not always be relevant to the cardiomyocyte environment. For example, in the case of *1795insD* mutation, scientists obtained opposing and inconclusive effects on sodium current density and kinetics when they studied the *SCN5A-1795insD* mutation in *Xenopus* oocytes and *HEK293* [2] [61]. As a consequence of the different results obtained from these two systems, an analysis of the biophysical

properties of this mutation in the native myocyte environment was necessary. The subsequent transgenic mouse studies [45] further showed the risk of over-interpretation of biophysical properties of a certain mutation using solely studies in heterologous expression systems.

Cardiomyocytes derived from human induced pluripotent stem cells (*hiPSCs*) may constitute an alternative way to study mutations in a more physiological environment. *hiPSCs* have already proven suitable candidates for investigation of patient- and disease-specific consequences for electrophysiology and pharmacology [22]. Some reports have shown that *hiPSC*-derived cardiomyocytes from human *SCN5A* mutation carriers and *SCN5A* transgenic mice can recapitulate the disease phenotype [27] [13] [56]. Despite these advances, this kind of cells remains a controversial tool due to its certain electrophysiological immaturity.

Up to date there are still questions left to be resolved regarding the understanding of the genetic and biophysical aspects of cardiac sodium channelopathies. In particular there is a lack of knowledge regarding the phenotypic variability observed in patients carrying *SCN5A* gene related mutations.

We believe that a significant contribution for a better understanding of these disease mechanisms can come from mathematical models and computer simulations. In particular, the methodology of experimentally-calibrated populations of models has proven useful in exploring and characterising variability inherent in complex systems such as cardiac electrophysiology, both in physiological and pathological conditions. Hence, the goal of this project is to use population of human ventricular cell models both at single cell level and at tissue level to explore the effect of variability on *SCN5a-1795insD* mutation.

1.2 Contribution

The work described in this thesis has been entirely developed and implemented during my research stay in the Computational Cardiovascular Science Group, Department of Computer Science, University of Oxford, in the context of the well-established academic collaboration between this group and the Department of

Electrical, Electronic, and Information Engineering "Guglielmo Marconi", University of Bologna, where I am enrolled as a Biomedical Engineering MSc student. Moreover, this dissertation is based on the experimental data provided by the collaborators from the Department of Experimental Cardiology, Academic Medical Center, University of Amsterdam, who performed the electrophysiological experiments.

2
Background

Contents

After a brief introduction (Section 2.1), this chapter is divided in two main sections, the first one (Section 2.2) is focused on the clinical scenario and will provide an overview on the basic aspects of cardiac electrophysiology (Subsection 2.2.1) as well as on the *SCN5A-1795insD* mutation (Subsection 2.2.2), including the clinical characteristics of family members and the experimental electrophysiological studies performed. Moreover, the Subsections 2.2.3 and 2.2.4 will present the clinical manifestation of the two main syndromes (*BrS* and *LQT3*) characterising the mutation under investigation. The second main section (Section 2.3) will describe the mathematical models and computer simulations used in cardiac electrophysiology.

2.1 Introduction

SCN5A is one of 10 genes encoding sodium channel alpha subunits. Of these subunits, $Na_V 1.5$ subunit encoded by *SCN5A* gene is the main component of sodium channel in the heart. The influx of sodium ions through this channel generates the cardiac sodium current, that underlies the fast upstroke of the cardiac Action Potential (AP) and plays a crucial role in cardiac electrophysiology [60]. Genetic studies have shown that mutations in *SCN5A* gene are associated with various arrhythmia syndromes (e.g. *BrS*, long QT (LQT) syndromes, conduction disease and cardiomyopathy) by modulating various gating and other functional properties of the sodium channel [62]. During the past decades, the understanding of these sodium channelopathies has increased strongly, but there still is a lack of knowledge regarding the biophysical properties of the mutant sodium channels and how these properties reflect themselves in patients' clinical symptoms. Initially, the syndromes caused by these mutations were considered different clinical entities, even though they were caused by mutations in the same ion channel [47]. In 1999 Bezzina et al. described for the first time a single, large *SCN5A*-linked family with phenotypic characteristics of both *LQT3* and *BrS* in the same patients [2]. After that, many other reports demonstrated that one particular mutation may lead to a mixed clinical phenotype in one carrier and to a single arrhythmia syndrome (either *LQT3*, *BrS*, or conduction disease) in another (see the extensive review of literature done in [47] for more details). Nowadays there is a raised awareness regarding a bigger overlap in these syndromes than traditionally appreciated, even though the underlying mechanisms are still unclear. This spectrum of *SCN5A*-related arrhythmia syndromes is generally referred to as *overlap syndromes of cardiac sodium channel disease* [46]. Identification of the mechanisms underlying this variability in the manifestation of the disease, together with a deeper insight regarding possible dysfunction and dysregulation of the cardiac sodium channel, is crucial to achieve improved diagnosis, more accurate risk stratification and effective treatment strategies.

In this dissertation, we focused on a particular *overlap syndrome of cardiac sodium channel disease*, the *SCN5A-1795insD* mutation, described for the first time

in 1999 by Bezzina and colleagues. It is caused by an insertion of 3 nucleotides (*TGA*) at position 5537 in the *SCN5A* gene, that results in the insertion of aspartic acid (*1795insD*) in the C-terminal domain of the protein. The functional consequences of the mutation are a sustained sodium current throughout the *AP* plateau that prolongs cardiac repolarisation and a drastic reduction in peak sodium current density. Patients suffering from this mutation show several abnormalities in their electrocardiogram (*ECG*) traces, in particular those similar to patients suffering from *LQT3* and *BrS*. Our final aim was to derive further insights based on mathematical modelling and computer simulations into this type of high risk life-threatening disease. We therefore used the populations of models methodology that is capable to reproduce and explore the variability in terms of disease expression and severity. In addition, we exploited a multi-scale approach in order to study the mutation effects on both single cell and fibre populations to generate simulated data that could be compared to the clinical one.

2.2 Electrophysiological and clinical background

2.2.1 Basic cardiac electrophysiology

The heart is a double pump electrically driven and coordinated. The right heart pumps blood through the pulmonary circulation, via the pulmonary valve, to the lungs and then back to the heart, while the left heart pumps the oxygenated blood through the systemic circulation, via the aortic valve, around the body [16]. The passage of blood through the heart is shown in Figure 2.1. The heart consists of four chambers: the interatrial septum separates the two atria, the upper chambers, while the two ventricles, the lower chambers, are separated by the interventricular septum. The atrioventricular septum separates the atria from the ventricles and contains the tricuspid valve in the right heart and the mitral valve in the left heart. The ventricular walls are externally lined by a thin connective layer called epicardium and internally by the endocardium.

The electrical activation of cardiac cells is coupled with their mechanical contraction. For most cardiac cell types, the excitation of a myocytes is initiated

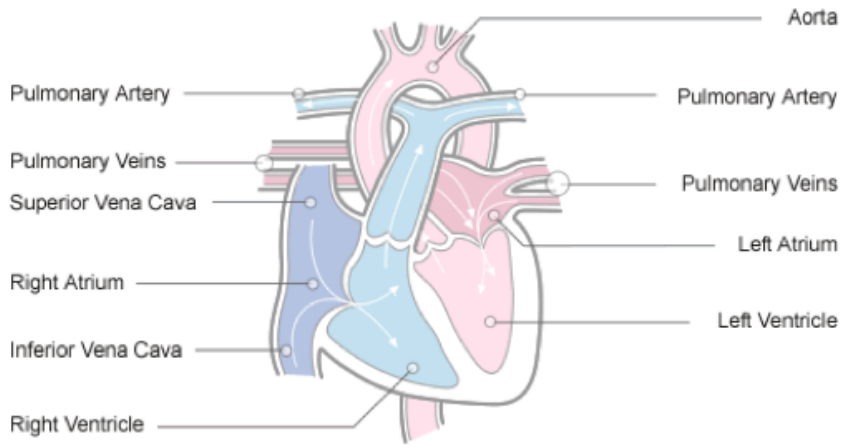

Figure 2.1: The passage of blood through the heart [32].

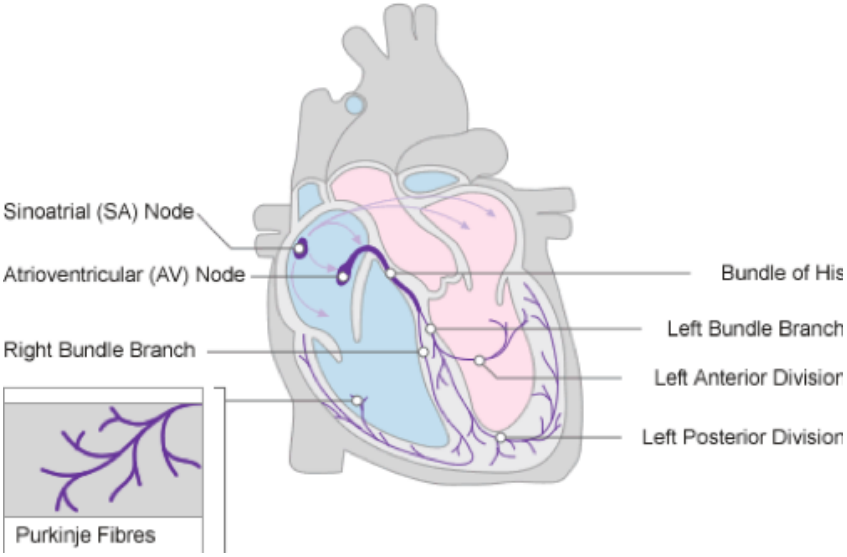

Figure 2.2: The cardiac conduction system [32].

by a stimulus current. When the stimulus is strong enough, the transmembrane potential which is the potential difference across the cell membrane rapidly increases from the negative resting value to a positive value, remains positive for a certain period, and then gradually returns to the negative resting value. This event is called an action potential (AP), while the rapid increase of transmembrane potential is called depolarisation, and the slow decrease of the potential is called repolarisation. The main phases of a typical ventricular AP are (Figure 2.3):

- Phase 0. Myocytes undergo a rapid depolarisation due to the opening of the fast Na^+ channels. This causes a rapid increase in the membrane conductance

and thus a rapid influx of Na^+ ions into the cell, the Na^+ current.

- Phase 1. Inactivation of the fast sodium channels. The transient net outward current that causes the small downward deflection of the AP is due to K^+ and Cl^- ions carried by the I_{to1} and I_{to2} currents, respectively.

- Phase 2. Plateau phase. It is sustained by a balance between inward movement of Ca^{2+}, the I_{CaL} current through L-type calcium channels, and outward movement of potassium ions K^+, the I_{Ks} current through the slow delayed rectifier potassium channels.

- Phase 3. Rapid repolarisation phase of the AP. The L-type Ca^{2+} channels close while the slow delayed rectifier (I_{Ks}) K^+ channels are still open. This ensures a net outward current, corresponding to negative change in membrane potential allowing more types of K^+ channels to open. These are primarily the rapid delayed rectifier K^+ channels (I_{Kr} current) and the inward rectifier K^+ current I_{K1}. This net outward, positive current causes the cell to repolarize. The delayed rectifier K^+ channels close when the membrane potential is restored to about -80 to -85 mV, while I_{K1} is maintained throughout phase 4, contributing to set the resting membrane potential.

- Phase 4. Resting phase. The transmembrane potential remains at the resting value of about -84 mV.

Apart from the above currents, the sodium-calcium exchanger current I_{NaCa} and the sodium/potassium pump current I_{NaK} also play important roles throughout the AP, contributing to the homeostasis of intracellular calcium, potassium and sodium ions.

In physiological conditions, the sinoatrial node (SAN) cells located on the right atrium generate an AP that propagates throughout the right atrium and to the left atrium, producing the contraction of both atria. The atrioventricular node (AVN) is then reached by the activation front and it is the main responsible for the conduction delays between the contraction of atria and ventricles . The delay timing is extremely important in order to optimize the atrial pump activity and to

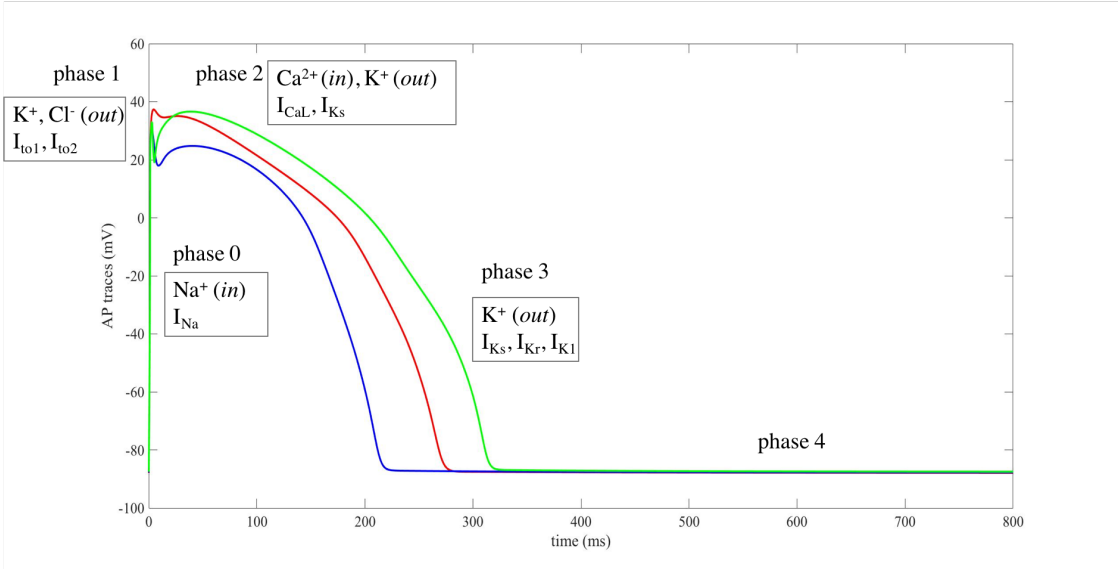

Figure 2.3: Different phases of the cardiac AP and main ionic currents involved. The AP traces represent an endocardial (red), M (green) and epicardial (blue) cell, simulated with the baseline cell model used in this investigation.

avoid a too early stimulation in the ventricles. The AVN conducts the AP through the atrioventricular septum, activating the *His* and the *Purkinje* network and the stimulus ends on the endocardial surface of the ventricles. The cardiac conduction system is reported in Figure 2.2. Cardiac APs differ significantly in different regions of the heart. Indeed, APs from atrial, ventricular and specialized conduction myocytes exhibit different waveforms [16]. Moreover, different AP morphologies have been observed in the epicardial, midmyocardial (M-cells), and endocardial isolated myocytes (transmural heterogeneity) and also along the apex-to-base direction of the ventricle (apex-to-base heterogeneity). The sequence of repolarisation and the actual AP duration distribution in the entire myocardial wall are affected by the heterogeneous properties of these myocytes (spatial dispersion of AP duration).

The ECG is the registration of the extracellular potential on the body surface due to the propagation of cardiac APs (Figure 2.4). The recording electrodes are usually placed at standard positions and the resulting various deflections in the ECG signal are commonly denoted in alphabetic order as P, Q, R, S, T, U. The temporal sequence of these waves remains constant, but their amplitude and sign can vary depending on the recording electrode position on the thorax:

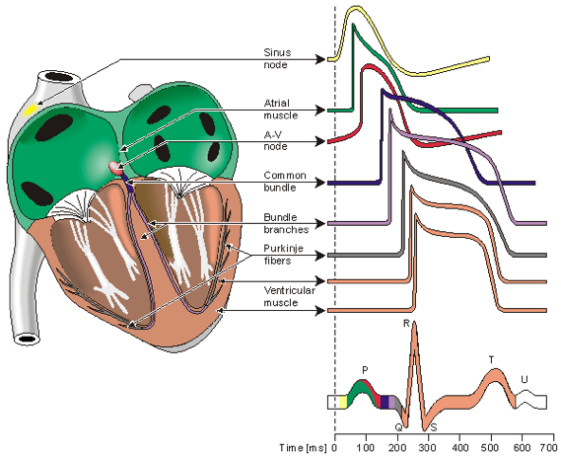

Figure 2.4: Electrophysiology of the heart. The different waveforms for each of the specialised cells of the heart [38].

- P wave. Atrial depolarisation (it continues during the subsequent PQ segment). The atrial repolarisation is not visible in normal $ECGs$ because hidden by the QRS complex. The PQ segment is also associated with the atrioventricular conduction delay.

- QRS complex. Activation sequence of the ventricles. The Q wave corresponds to the activation of the interventricular septum, the R wave corresponds to the septum activation completion and the apex activation, the S wave corresponds to the activation of the ventricular free walls and the basal region.

- ST segment. Isoelectric interval, all cells are depolarized during the plateau of the AP. It starts at the end of the QRS complex (the so-called J point) and ends at the beginning of the T wave.

- T wave. Ventricular repolarisation. In normal hearts, the start of the T wave is thought to correlate with the plateau ending of the epicardial cells, the T wave peak with the full repolarisation of the epicardium, the end of the T wave with the end of repolarisation of the myocardium.

- QT interval. The QT interval is measured from the beginning of the QRS complex to the end of the T wave. Since the QT interval is strongly frequency

dependent, a corrected QT interval QTc is sometimes defined, for example by normalizing it as $QTc = QT/\sqrt{RR}$.

- U wave. After the T wave, it is sometimes present a smaller diastolic deflection known as U wave. Some authors explain the U wave as due to repolarisation of the papillary muscles or *Purkinje* fibres, while others explain it as due to late repolarisation of M-cells or yet to afterpotentials caused by ventricular stretch.

2.2.2 The *SCN5A-1795insD* mutation

In 1999, Bezzina and colleagues provided the first evidence that a single mutation in the *SCN5A* gene may lead to multiple rhythm disturbances within the same family. The *SCN5A-1795insD* mutation was characterized in a large multigenerational Dutch family showing a wide variability in type and severity of symptoms, including *BrS*, *LQT3*, sinus node dysfunction, bradycardia and conduction disease, either in isolation or in combinations thereof [2]. Due to the presence of this overlap in the clinical manifestation, this syndrome is one of the *overlap syndromes of cardiac sodium channel disease* mentioned above and it is also generally referred to as *The Human Overlap Syndrome*.

Clinical characteristics of family members

In 1958, a 16-year-old male went to the hospital (Department of Internal Medicine, University Hospital, Groningen) for a routine sports examination. His electrocardiogram showed some abnormalities (Figure 2.5). He revealed an abnormal T wave configuration (biphasic T wave) with a severely prolonged QTc interval ($520ms$) [58]. The patient did not have any symptoms and no structural cardiac disease was apparent. His family history included the unexpected (nocturnal) death of his mother (aged 54 years), two sisters (aged 15 and 26 years) and a brother (aged 21 years) and similar abnormal ECG features were displayed by many of his family members. The most profound repolarisation abnormalities were always

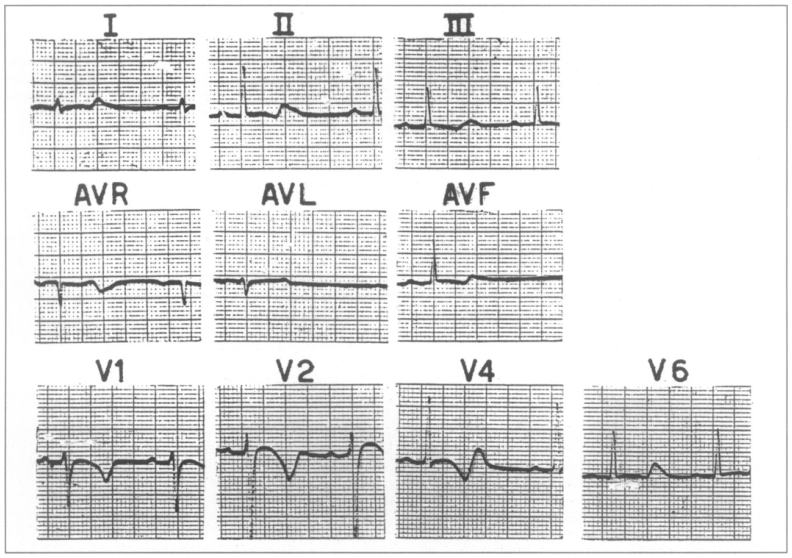

Figure 2.5: Original electrocardiogram of the 16-year-old boy at presentation in 1958. The QT interval and QTc are prolonged ($0.60s$ and $0.55s$, respectively). Other prominent features are a long isoelectric ST segment preceding a sharp T wave in lead I and V_6 and biphasic and negative T waves in leads I, V_2 and V_4 [58].

found at the lowest heart rates, coherently with the nocturnal deaths. Soon it became clear that it was a familial disease.

In subsequent years the group of M.P. van den Berg started collecting clinical data in as many family members as possible [58], performing standard *ECG*, 24-hour ambulatory electrocardiographic (*Holter*) monitoring, ergometry, signal-averaged *ECG* and echocardiography. Electrophysiological studies were also considered in selected cases and, after the identification of the mutation (1998), genotyping was performed diagnostically. In May 2002, data on phenotype and genotype were available on 232 family members of whom 114 were mutation carriers and 118 were non-carriers. Since 1905 sudden death occurred in 29 family members. Besides sudden death, symptomatology was rather limited [58]. In 2009, they had clinical data on 378 family members of whom 149 carry the *SCN5A-1795insD* mutation [43]. Nowadays this family consists of 400 members in total.

ECGs from patients carrying the mutations were characterised by a relatively slow heart rate and prolongation of the PQ interval and QRS duration. However, electrocardiographic markers of ventricular repolarisation were always the most remarkable features, together with a markedly prolonged QT interval corrected

for heart rate. Notably, the *ECG* traces also showed a long iso-electric *ST* segment preceding a sharp *T* wave, and many patients demonstrated biphasic *T* waves in one or more precordial leads. Slight elevation of the *ST* segment in the right precordial leads was also present in a large subset of carriers (49%), similar to patients suffering from the *BrS*. Holter recordings were characterised by relative bradycardia (throughout the entire day) and excessive prolongation of the *QT* interval at slow heart rates. Initially, when the diagnosis was still elusive, clinicians considered structural heart disease as a possibility. Later, using the echocardiography, structural abnormalities were not found in any of the carriers. However, evidence is now accumulating that sodium channelopathy may be involved in cardiac fibrosis, dilatation, and hypertrophy. This has been shown both in patients [3] [12] [17] and in *SCN5A* mouse models [49] [66].

In subsequent years, considerable progress has been made in terms of preventive treatment. Initially the exact origin of the premature deaths was unknown, and only after 20 years with a lack of treatment options, antibrady-pacing was introduced in the family in 1978. During 23 years of follow-up up to 2001 no more patients died [59]. When few patients died despite the pacemaker, researchers hypothesized that these patients suffered from a tachyarrythmic event which could expectedly not be treated by the device. In fact, in all cases there was no (brady)arrhythmic event recorded by the device. For this reason, the currently treatment consits in implantable cardioverter-defibrillators (*ICDs*). Notably, when the pacemaker was introduced, the exact mechanism underlying the disease was still not known. Only in 1998, genetic studies were performed and the mutation linked to the *ECG* abnormalities was uncovered (*SCN5A-1795insD*) [2]. Bezzina and colleagues showed that linkage analysis in a subset of the family revealed linkage to *SCN5A* gene, whereas no linkage was detected to other *LQT* syndrome loci. The insertion of 3 nucleotides (*TGA*) at position 5537 caused the insertion of aspartic acid (*1795insD*) in the *C*-terminal domain of the protein. These 3 nucleotides were identified in all electrocardiographically affected family members. It is worth mentioning that in the same period the *SCN5A* gene had just been reported to be implicated in

LQT3, *BrS*, and in progressive cardiac conduction defects. This was consistent with the fact that affected family members could display features related to all three of these syndromes. In this way, an arrhythmia overlap syndrome resulting from a single cardiac ion channel mutation was described for the first time [2].

Experimental electrophysiological studies

To summarize, the Dutch family carrying the *SCN5A-1795insD* mutation displays profound variability in type and severity of symptoms, including *ECG* features of *BrS* (*ST* segment elevation), and *LQT* syndrome (*QT* interval prolongation), in addition to sinus node dysfunction, bradycardia and conduction disease, either in isolation or in combinations thereof. Among these patients there is a huge variability in disease severity, in spite of having the same primary genetic defect. Electrocardiographic signs of the disease may be displayed from some patients, some others may be unaffected. It is also common that some mutation carriers remain symptom-free throughout life while some individuals present with arrhythmia, even though all of them are electrocardiographically affected family members. Thus, identification of mutation carriers at risk for serious cardiac events is challenging.

To achieve more insights in understanding the mechanisms underlying the mutation, experimental electrophysiological studies were performed. Expression studies in *Xenopus* oocytes revealed the presence of reduced sodium current density, with a negative shift in voltage dependence of inactivation, but no persistent inward current [2]. On the other hand, when expressed in human embryonic kidney (*HEK293*) cells, the mutation caused a disruption of fast inactivation, resulting in a sustained inward sodium current, in addition to an increased slow inactivation leading to decreased sodium channel availability under conditions mimicking fast heart rates [61]. These characteristics were also introduced in a computational simulation model of a ventricular myocyte, showning that the *1795insD* mutation is strongly related to the heart rate, causing both *LQT* and *BrS* [9]. Since researchers that studied the mutation in the two different expression systems mentioned above obtained different results, the necessity of analysing the

biophysical properties of this mutation in the native myocyte environment was evident. Therefore, transgenic mice carrying the heterozygous *SCN5A-1798insD* mutation (equivalent to human *SCN5A-1795insD*) were generated by the group of Carol Ann Remme. Results from this mouse model showed that it recapitulates faithfully the phenotype observed in patients [45]. They observed signs of sinus node dysfunction, in addition to prolonged *PQ*, *QRS*, and *QTc* intervals on surface *ECGs*. Epicardial mapping experiments on isolated hearts showed conduction slowing predominantly in the right ventricle, considered a hallmark of *BrS*. Patch-clamp analysis of *AP* characteristics in isolated myocytes was in accordance with Veldkamp et al. [61] and Clancy and Rudy [9], in terms of heart rate-depentent coexistence of both *LQT3* and *BrS*, with a prolongation of cardiac repolarisation, predominantly at slow rates and decreased sodium channel availability, especially at high frequencies. Generating the *SCN5A-1798insD* mouse, they created the first transgenic model of a sodium channelopathy evoking multiple cardiac rhythm disturbances. This was the confirmation that an overlap syndrome of cardiac sodium channel disease can be caused by a single *SCN5A* mutation. However, from these findings, it is even more clear that interpreting biophysical properties of a certain mutation using entirely data from studies in heterologous expression systems is dangerous and a native enviroment should be considered.

Furthermore, it is worth mentioning the work done by Davis et al. in 2012 [13] on *iPSCs*. They demonstrated that both embryonic stem cell- and *iPSC*-derived cardiomyocytes can recapitulate the characteristics of a combined gain- and loss-of-function Na^+ channel mutation.

According to the results presented here, we decided to model the effects of the mutation through a drastic reduction in peak sodium current density and a persistent (late) sodium current (as shown in Figure 2.6), both can in fact explain the observed multiple phenotypes.

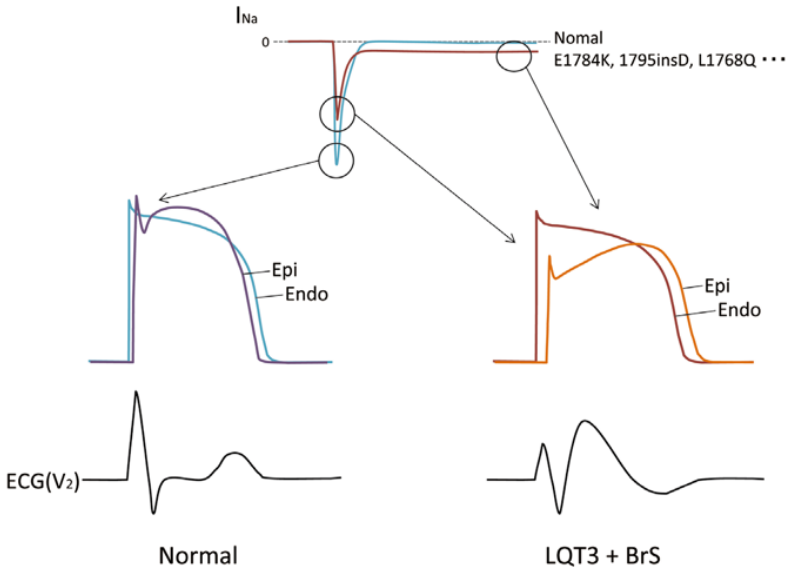

Figure 2.6: Schematic of the electro-physiological mechanisms underlying the overlap phenotype of *LQT3* and *BrS* caused by a single *SCN5A* mutation. A persistent (late) inward Na^+ current during the *AP* plateau phase can lead to prolongation of the *QT* interval. A reduction of the peak Na^+ current, especially in epicardial (*Epi*) ventricular cells, may produce Brugada-type *ST* elevation on the *ECG* [34].

2.2.3 Brugada syndrome

BrS is an inherited disease characterized by an increased risk of sudden cardiac death in the absence of structural heart abnormalities [50]. It was described in 1992 for the first time but, to date, the mechanisms underlying the syndrome remain unclear. Several hypothesises have been proposed, but there are no studies proving evidences in support of a theory excluding all the others. The theories proposed involve abnormalities in both repolarisation and depolarisation processes. Since patients suffering from the syndrome show variability in the electrocardiographical manifestation it could be that the same mechanism might not be responsible for the disease in all patients. Numerous different pathophysiological mechanisms may cause the phenotype known as Brugada [50]. To date, scientists are moving towards the idea that the repolarisation-depolarisation abnormalities underlying the *BrS* phenotype are all part of a complex polyfactorial pathological system that cannot be simplified by a single causal mechanism [14]. Zhang and colleagues [65] demonstrated, making use of non-invasive *ECG* imaging (*ECGI*), that both abnormal repolarization and abnormal conduction are present in the electrophysiological substrate in *BrS*

patients, especially in the right ventricle outflow track ($RVOT$), supporting the idea of the coexistence of the two mechanisms.

Due to this huge phenotypic variability, accurate risk stratification is fundamental in the management of these patients. While it is easier to identify patients with significant ECG abnormalities, on the other hand it is more difficult for those who show normal ECG, but they can still develop arrhythmic events [50]. The most effective strategy consists in evaluating each patient individually with a personalized approach of the syndrome. The priority remains the identification of patients at risk of sudden cardiac death, although at present asymptomatic and drug-induced patients with BrS are more under investigation then in the past. ECG abnormalities constitute the hallmark of BrS. They include repolarisation and depolarisation abnormalities in the absence of identifiable structural cardiac abnormalities or other conditions or agents known to lead to ST segment elevation in the right precordial leads [63]. Wilde and colleagues [63] describe the three types of recognised patterns in this way (Figure 2.7): type 1 is characterised by a prominent coved ST segment elevation displaying J wave amplitude or ST segment elevation of 2 mm or 0.2 mV at its peak followed by a negative T wave, with little or no isoelectric separation. Type 2 also has a high take-off ST segment elevation, but in this case, J wave amplitude (2 mm) gives rise to a gradually descending ST segment elevation (remaining 1 mm above the baseline), followed by a positive or biphasic T wave that results in a saddle back configuration. Type 3 is a right precordial ST segment elevation of 1 mm of saddle back type, coved type, or both. The QT interval is often within normal limits (in the absence of anti-arrhythmic drug therapy), but it may be prolonged. The PR interval is often increased (200 ms). Current clinical guidelines and consensus documents state that BrS is diagnosed in patients with ST segment elevation with type 1 morphology >2 mm in one or more leads among the right precordial leads V_1 and/or V_2 positioned in the second, third, or fourth intercostal space, occurring either spontaneously or after provocative drug testing with intra-venous administration of sodium channel blockers [50]. Other

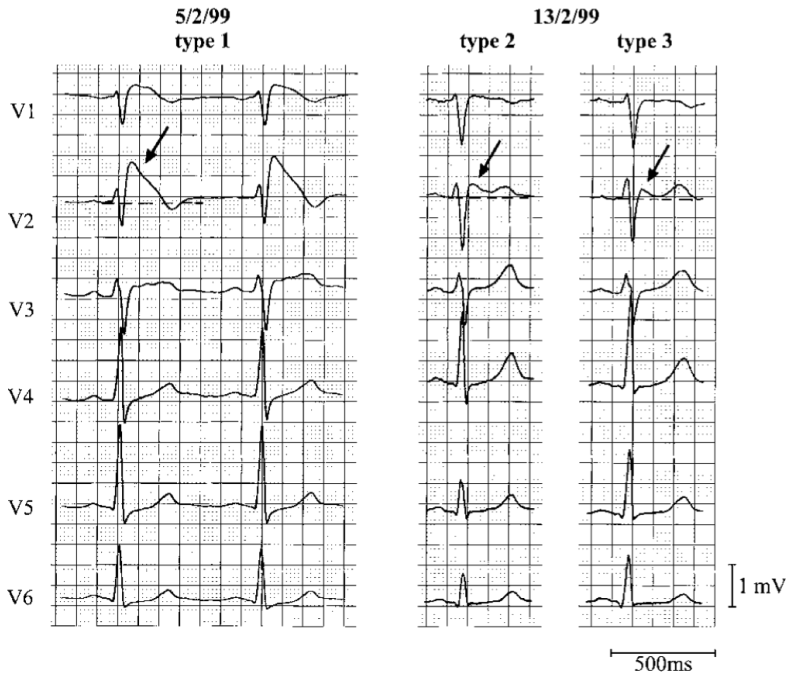

Figure 2.7: Precordial leads of a resuscitated patient with *BrS*. All 3 patterns are shown. Arrows denote the J-wave. The left panel shows a clear type 1 *ECG*. Between 7-2-99 and 13-2-99, types 2 and 3 are shown. [63].

ECG patterns may help in risk stratification, as the proposed *fragmentation of the QRS complex*. However, its added value as risk factors remains to be proved.

The most accepted therapy for patient at high risk are *ICDs*. Novel therapies such as electrophysiological-guided drug therapy or epicardial substrate ablation might be useful in selected patients [50].

As previously mentioned the two principal hypothesises explaining cellular mechanisms underlying *BrS* are the repolarisation hypothesis and the depolarisation hypothesis. The repolarisation hypothesis (Figure 2.8) suggests that an outward shift in the balance of currents in the right ventricular epicardium can result in repolarisation abnormalities [64]. According to this theory the observed *ST* segment elevation in the *ECG* of patients with *BrS* is due to a reduced inward sodium current and a prominent outward current. What happens is that the *AP* notch in the right ventricular epicardium is accentuated relative to the endocardium and it produces a transmural voltage gradient. The outward shift in the currents may also lead to a all-or-none repolarisation for certain epicardial sites, losing

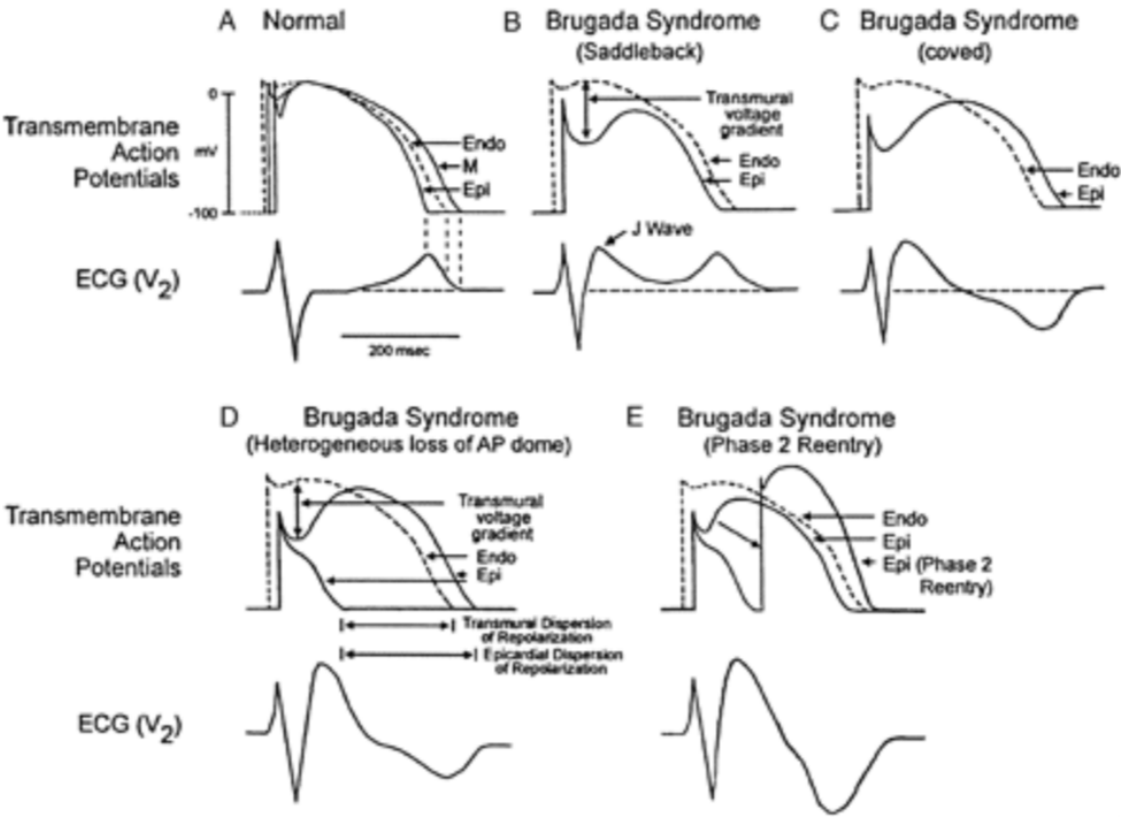

Figure 2.8: Qualitative model of the repolarisation disorder hypothesis in the *BrS* [29].

their *AP* dome and resulting in the development of a local epicardial dispersion of repolarisation. This phenomenon generates a heterogeneous repolarisation environment that is more prone to lead to phase 2 reentries and couple extrasystoles when *AP* domes migrate from sites where they are present to sites where they were lost [14]. On the other hand, the depolarisation hypothesis (Figure 2.9) claims that slow conduction in the *RVOT* has a primary role in the development of the electrocardiographic and arrhythmic manifestations of *BrS* [12]. As stated in this theory the conduction delay in the *RVOT* together with the abnormal current created by delayed depolarisation of this region causes the *ST* segment elevation seen in these patients. The repolarisation and depolarisation mechanisms underlying the development of *BrS* are not necessarily mutually exclusive, and might indeed have a synergistic role [50]. In fact, in order to explain the coexistence of the two theories, it has been proposed [4] that the *RVOT* and its nearby structures have different embryological origins compared with the rest of the heart, and consequently

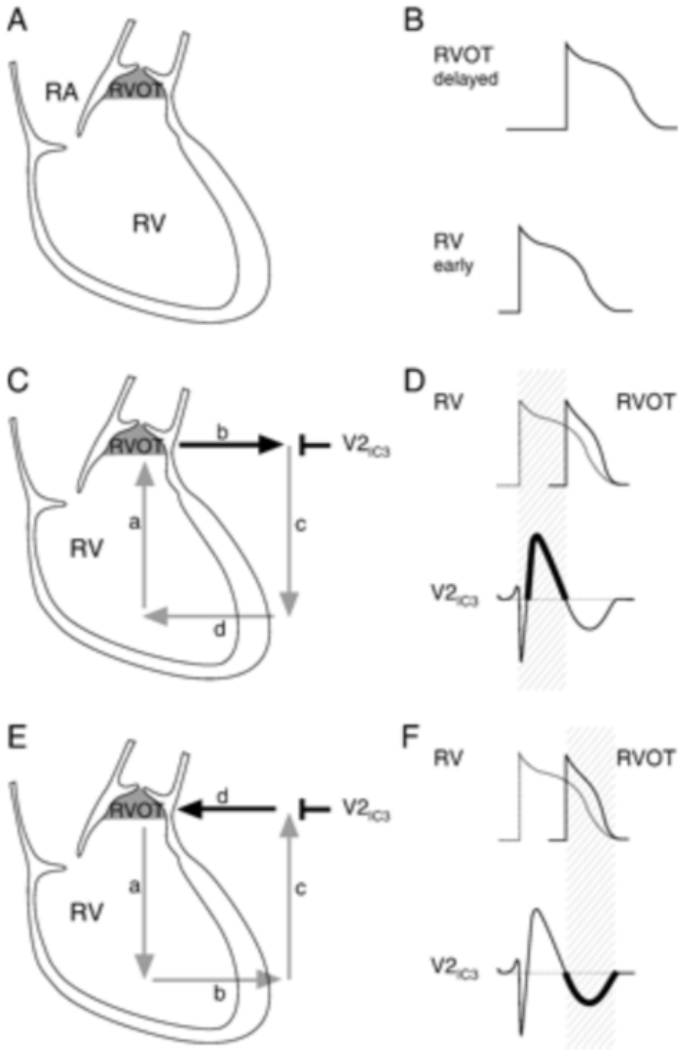

Figure 2.9: Qualitative model of the depolarisation disorder hypothesis in the *BrS* [29].

possess different physiological, anatomical, and clinical characteristics. It is also worth mentioning that mutations in the cardiac sodium channel gene *SCN5A*, have been identified in 11-28% of patients with *BrS*.

2.2.4 Long *QT* type 3 syndrome

Perez-Riera et al. describe the *LQT3* Syndrome as an autosomal dominant channelopathy (with autosomal recessive inheritance in exceptional cases) responsible for 7-10% of total *LQT* syndromes as a consequence of *SCN5A* gene mutations [41]. It is electrocardiographically characterized by a tendency to bradycardia related to age, prolonged *QT/QTc* interval, accentuated *QT* dispersion consequence of prolonged

ST segment, late onset of T wave and frequent prominent U wave because of longer repolarisation times across left ventricular wall [41]. The excessive inflow of late sodium current during the AP plateau phase is due to the disruption of fast inactivation of sodium current and it is the basic defect in *LQT3*. This abnormal inflow may cause several distinct mechanisms of arrhythmogenesis, including early after-depolarisations that may subsequently trigger Torsades De Pointes and sudden death [44].

2.3 Mathematical models and simulations

In this dissertation, we model cellular electrophysiology mechanisms specific to human ventricular myocytes. However, the use of mathematical modeling of cell electrophysiology has a long history, and numerous models are now available at all scales, describing different species, cell types and experimental conditions, to investigate cellular and tissue levels phenomena.

2.3.1 Cellular electrophysiology mathematical models

After the series of papers about the flow of electric current through the surface membrane of a giant nerve fibre, published in 1952 by Alan Lloyd Hodgkin and Andrew Huxley [21], mathematical models have acquired a central role in the investigation of cellular electrophysiology. The earliest example of cardiac cell electrophysiology model consists in the pioneering work done by Denis Noble [35]. Modifying the Hodgking-Huxley model to simulate the behaviour of Purkinje fibres in mammals, he developed the first mathematical model to reproduce the basic electrical properties of cardiac tissue. In recent years, as a consequence of the collection of more data from human cardiomyocytes, the development of more powerful electrophysiological measurement technique and the growing of available computing power, several new models (including Ten Tusscher et al. 2004 [54], Ten Tusscher et al. 2006 [55], Grandi et al. [19]) have been developed enabling deeper understanding of cardiomyocyte functions and properties. The most validated and used model of human ventricular cell has been proposed by O'Hara et al. in 2011

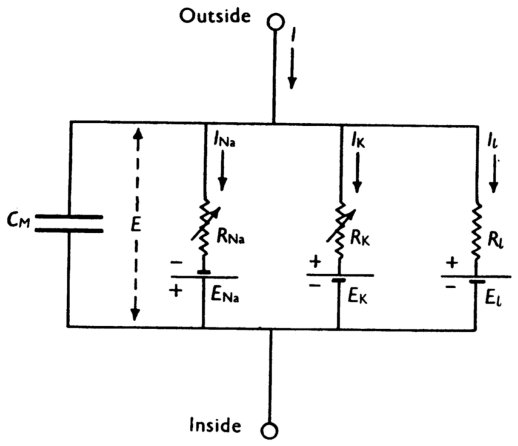

Figure 2.10: Electrical circuit representing the cell membrane [21].

(O'Hara-Rudy dynamic model, *ORd*) [36], although few minor modifications to this model have already been proposed in order to overcome certain limitations [15] [39].

Most of the recent models are based on the Hodgkin-Huxley formulation, according to which the electrical behaviour of the cell membrane may be represented by the network shown in Figure 2.10. The membrane of the myocyte is acting as a capacitor and the voltage membrane is modelled using the following equation:

$$\frac{dV}{dt} = -\frac{1}{C_m}(\sum I_j + I_{stim})$$

where t is time, C_m is the capacitance of the membrane, I_j represents the ionic current j and I_{stim} is the applied stimulus current. The current I_j is typically governed by other variables ($\boldsymbol{u}$) that account for ion-channel states and other quantities such as ion concentrations in different cellular compartments. These variables satisfy the *ODE* system:

$$\frac{d\boldsymbol{u}}{dt} = \boldsymbol{f}(\boldsymbol{u}, V)$$

where $\boldsymbol{f(u}, V)$ is a vector of functions describing the evolution of each component of $\boldsymbol{u}$.

The *ORd* model (Figure 2.11) is based on data from over 100 undiseased human hearts for steady state rate dependence and restitution of the ventricular *AP*. Essential new measurements for the *L*-type Ca^{2+} current, K^+ currents, and Na^+/Ca^{2+} exchange current from undiseased human ventricle have also been used. Those data were previously unavailable. Using the new data together with

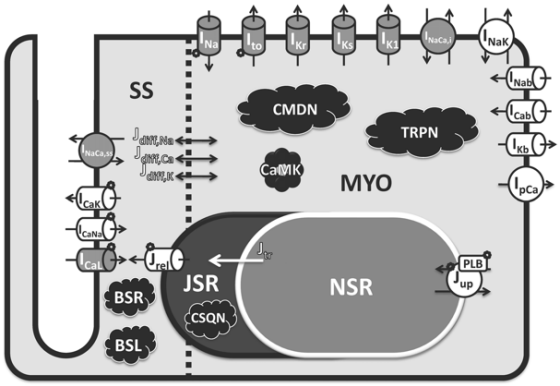

Figure 2.11: Schematic diagram of human ventricular myocyte model [36].

previously published experiments, Thomas O'Hara and colleagues developed and validated a detailed mathematical model of undiseased human ventricular myocyte electrophysiology and Ca^{2+} cycling. Moreover they created a complete dataset for transmural differences between endocardial (endo), mid-myocardial (M), and epicardial (epi) cell types (Table 2.1). The *ORd* model has been used to describe

Parameter	***Epi/Endo***
G_{NaL}	0.6
G_{to}	4.0
P_{Ca} P_{CaNa} P_{CaK}	1.2
G_{Kr}	1.3
G_{Ks}	1.4
G_{K1}	1.2
$G_{NaCa,i}$ $G_{NaCa,ss}$	1.1
G_{NaK}	0.9
G_{Kb}	0.6

Table 2.1: *ORd* Human Model Transmural Heterogeneity.

cellular electrophysiology mechanisms specific to human ventricular myocytes such as the underlying mechanisms of AP duration (APD), rate dependence, and APD restitution. The effects of Ca^{2+}/calmodulin-dependent protein kinase II ($CaMK$) on known ionic current and Ca^{2+} cycling targets have been incorporated and studied. Early afterdepolarisations ($EADs$) and alternans have been reproduced by the model [36].

As previously mentioned, few minor modifications to the *ORd* model have been proposed by the *FDA* and the *Computational Cardiovascular Science Group*. The

modifications proposed by the *FDA* involve several aspects. First of all, in 2016 Li and colleagues developed a new temperature-sensitive model of *hERG* gating in order to improve the predictivity of safety pharmacology testing by enabling the translation of room temperature *hERG* assay data to more physiological conditions [24]. They highlighted the importance of accounting for temperature-dependent *hERG* channel activity changes to permit an extrapolation of the results across temperatures. The model that they suggested has two components: a base model dealing with temperature-dependent gating changes without drug and a pharmacodynamic component simulating temperature-dependent drug binding kinetics. In 2016 the physiological component was constructed [24]. This *Markov* model can recapitulate macroscopic *hERG* channel gating behavior for a temperature range of $20°C$ to $37°C$. Then, in 2017 they published the pharmacodynamic component representing drug binding [23]. In the complete model, the pharmacodynamic component has 3 drug-bound states: open-bound (O^*), closed-bound (C^*) and open-inactivated-bound (IO^*), while in the physiological component *C1* and *C2* are closed states, *O* is open state, and the corresponding inactivated states are *IC1*, *IC2*, *IO* (Figure 2.12). In Li et al. [23] the formulation of I_{Kr} in the *ORd* model was replaced by the dynamic *hERG* model, with the I_{Kr} conductance adjusted to 0.0418 $mS/\mu F$ to better replicate original I_{Kr} behaviour. The dynamic *hERG* model was optimized to replicate the *ORd*-I_{Kr} behaviour under drug-free conditions. Finally, in 2017 Dutta and colleagues further optimized this model by refining model parameters using published human cardiomyocyte experimental data under control and drug block conditions [15]. They scaled the conductance of the main ion currents (I_{Kr}, I_{K1}, I_{Ks}, I_{NaL}, I_{CaL}) of the original I_{Kr}-*dynamic ORd* model to fit the *APD* rate dependence experimental data in control and drug block conditions from O'Hara et al. [36]. The best fit for the optimized model was achieved by scaling I_{Kr} by 1.013, I_{K1} by 1.698, I_{Ks} by 1.870, I_{NaL} by 2.661 and I_{CaL} by 1.007.

The *Computational Cardiovascular Science Group* performed few other modifications to the *ORd* model, as described in the Supplementary Material of

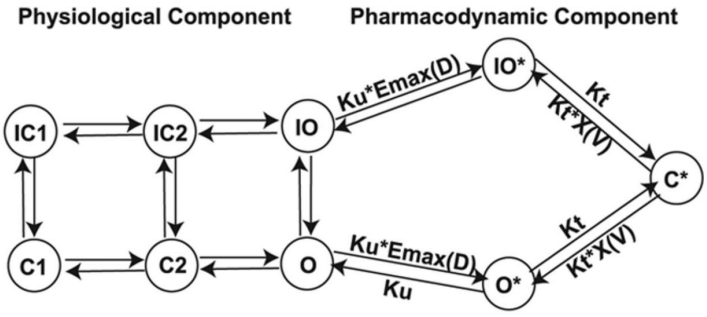

Figure 2.12: The structure of the *hERG* model [23].

Passini et al. 2016 [39], in order to better reproduce the experimental non-diseased data considered in that study. The baseline model for their investigations was the endocardial *ORd* human ventricular *AP* model together with the following modifications. The transient outward current I_{to} was increased 2.5 times. Importanlty, they modified the steady state inactivation and recovery from inactivation gates for the fast Na^+ current (h_{ss} and j_{ss}) keeping the original *ORd* formulation and optimising the channel's steady state inactivation response (half potential and slope) to match that of [54]. For the phosporylated gates, a -6.2 mV shift in their half potential of inactivation was applied. This modification on the sodium current kinetics derives from the note posted by O'Hara (see http://www.ploscompbiol.org/annotation/listThread.action?root=55207), in which he explains how to prevent propagation failure in the model. The current stimulus duration was set to 1 ms, with an amplitude of -53 $\mu A/\mu F$.

2.3.2 Tissue level mathematical models

The use of cardiac tissue electrophysiology models is further extended by encoding information about excitability at the cell level and electrical conduction at the tissue level, enabling quantitative description of *AP* propagation and a deeper understanding of the mechanisms governing the whole cardiac system. At the macroscopic scale, cardiac tissue behaves as a functional syncytium, supporting propagating waves of depolarisation and repolarisation [10]. Cardiac tissue contains excitable myocytes, whose membrane can undergo local depolarisation and trigger the opening of voltage-gated sodium channels and a rapid membrane depolarisation,

which generates an AP. Local gradients in membrane voltage produced by the AP upstroke cause current flow within the tissue. This current flow acts in turn to open voltage-gated sodium channels in neighbouring electrically connected cells, resulting in the propagation of the AP through the tissue [10]. Tissue-level cardiac electrophysiology can be modelled using the bidomain equations, a coupled system of equations describing the intracellular and extracellular potential fields through the cardiac tissue. The bidomain equations comprise two partial differential equations (*PDEs*) coupled at each point in space with a system of ordinary differential equations (*ODEs*) [40]. Electrical potential fields in intra- and extra-cellular spaces are modelled by the *PDEs*, as a reaction-diffusion system, while the concentrations of ions and other variables at the cellular level are governed by the *ODE* systems. The bidomain equations are [40]:

$$\chi(C_m\frac{\partial V}{\partial t} + I_{ion}(\boldsymbol{u}, V)) - \nabla\cdot(\sigma_i\nabla(V+\phi_e)) = I_i^{(vol)}$$

$$\nabla\cdot((\sigma_i+\sigma_e)\nabla\phi_e + \sigma_i\nabla V) = -I_{total}^{(vol)}$$

$$\frac{d\boldsymbol{u}}{dt} = \boldsymbol{f}(\boldsymbol{u}, V)$$

where

$$I_{total}^{(vol)} = I_i^{(vol)} + I_e^{(vol)}$$

ϕ_i and ϕ_e are the intracellular and extracellular electrical potentials, σ_i and σ_e are the intracellular and extracellular conductivity tensors, χ is the surface-area-to-volume ratio and C_m is the membrane capacitance per unit area. $\boldsymbol{u}$ is a set of cell-level variables, such as ionic concentrations and membrane gating variables, and $I_{ion}(\boldsymbol{u}, V)$ is the ionic current per unit surface area. Functional forms for I_{ion} and $\boldsymbol{f}$ are determined by an electro-physiological cell model. The source terms $I_i^{(vol)}$ and $I_e^{(vol)}$ are the intracellular and extracellular stimuli per unit volume. Appropriate boundary conditions are [40]:

$$\boldsymbol{n}\cdot(\sigma_i\nabla(V+\phi_e)) = I_i^{(surf)}$$

$$\boldsymbol{n}\cdot(\sigma_e\nabla\phi_e) = I_e^{(surf)}$$

where $\boldsymbol{n}$ is the outward pointing unit normal vector to the tissue, and $I_i^{(surf)}$ and $I_e^{(surf)}$ are the intracellular and extracellular currents per unit area applied across the boundary. The bidomain model of cardiac tissue can be simplified to the monodomain model by assuming that the anisotropy of the intracellular and extracellular spaces is the same [10]. So basically, it is assumed that the conductivity tensor in the extracellular space is proportional to the intracellular conductivity one. That results in a single *PDE*, coupled to the cellular electrophysiological *ODEs* [40]:

$$\chi(C_m \frac{\partial V}{\partial t} + I_{ion}(\boldsymbol{u}, V)) - \nabla \cdot (\sigma \nabla V) = I^{(vol)}$$

$$\frac{d\boldsymbol{u}}{dt} = \boldsymbol{f}(\boldsymbol{u}, V)$$

with the following boundary condition:

$$(\sigma \nabla V)\boldsymbol{n} = 0$$

where σ is the conductivity tensor. Numerical solutions are easier to obtain compared to the bidomain equations. However, the bidomain model provides a more detailed description of cardiac tissue, and the separation of intracellular and extracellular spaces is necessary to accommodate the injection of current into the extracellular space during external stimulation and defibrillation [10]. The choice between the bidomain and monodomain models depends on the purpose of the analysis and both are often used in cardiac modelling.

2.3.3 Population of models approach

Inter-subject and intra-subject physiological variability has significant implications for treating and managing heart diseases [33]. Physiological intra-subject variability exhibits itself at all levels from isolated cardiac cells to cardiac tissue level. Most importantly in terms of disease managing, the inter-subject variability is responsible for significant differences in the outcome of patients' exposure to pathological conditions or drug therapy. The variability underlying the physiological and pathological responses of different individuals has often been ignored in experimental and theoretical research [6]. In fact, experimentalists often need to average their

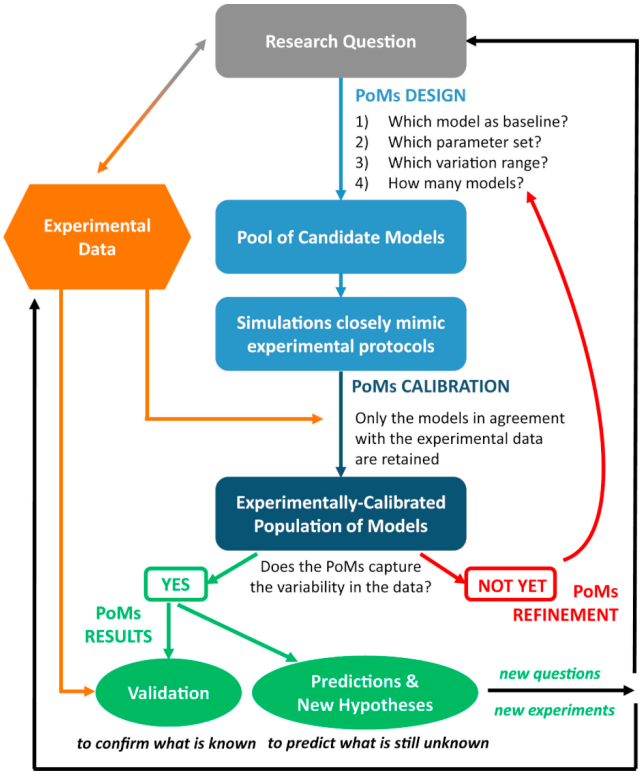

Figure 2.13: Flowchart illustrating the process behind constructing an experimentally-calibrated population of models [33].

results to minimize experimental error. Unfortunately, doing this means also to average out the effects of inter-subject variation, losing a lot of essential information. A similar approach is also used in medicine, where therapies are developed for the "typical" patient. Recently we are observing a shift towards personalised management of disease to increase the efficacy of the treatment, as well as the quality of life of patients. In silico models have proven to be a powerful tool to do so, enabling researchers to include the variability aspect. These models are able to reproduce human electrophysiology at different levels, and combing their results with clinical and experimental data can provide new insights into the mechanism underlying these differences. This has been already done in several studies (including for example [8], [6], [39]), using the population of models methodology. Experimentally-calibrated population of models means going beyond a single model and its typical behaviour to build an ensemble of models, whose behaviours show the variability in the population

that is under investigation. Moreover, experimental data are explicitly incorporated into the construction of populations. In this approach, the first step is selecting an appropriate cardiac cell model. Model parameters will be then varied to represent variability. The choice of parameters to be varied is a significant part of building a population of models. How we vary them is based on the aim of the investigation and must be taken into account when we analyse the results. The ionic currents that control the cardiac AP are primarily controlled by the ion channels through which they flow and indeed inter-individual differences in their configurations is a primary source of electrophysiological variability. In general, ion channels are produced with a consistent structure and consistent functional behaviour across a population of healthy individuals of the same species. However, the density of functional ion channels of a particular type that are present in the membrane of a cell is not expected to be as consistent, and is known to be subject to considerable variation from many sources (circadian rhythms; alteration of pacing rate; drug application; and the development of diseases that affect the heart) [5]. Substantial variation between cardiomyocytes, and between individuals, exists in ion channel densities in the cell membrane, leading to corresponding changes in the maximal flow of the ionic currents those channel conduct. Therefore, ionic current conductances are a common choice as parameters to be varied [33] in order to build a population of models that includes physiological variability. Differences between ion channel structures in different individuals also exist, however, this is usually due to a genetic mutation, and in general, unlike natural variability, functional mutations in ion channels are often pathological [5]. Choosing the ranges for parameter sampling is the following part. A large number of parameter sets is then generated, and it can be done in different ways. A common way to do so is using the Latin Hypercube sampling, a parameter sampling method that does not scale the computational cost with the number of varied parameters, allowing for an exploration of a complex parameter space [33]. After generating an initial candidate population of models, calibration steps can be applied to the population to select the models with physiological behaviour. Models whose simulated electrophysiological properties are in range

with the same properties in experimental data are selected and all the others are discarded. The experimentally-calibrated population of models can then be used to investigate disease conditions in population, to explore ionic mechanisms and to test new hypotheses. The population of models methodology has the ability to provide quantitative predictions that can be compared directly to experimental results. For example, it is possible to connect drug effects to specific ionic mechanisms, predict and explain disease phenotype and investigate potential disease therapies [33].

3 Methods

Contents

This chapter will describe the choice of the baseline cell model (Subsection 3.1.1) and the construction (Subsection 3.1.2) and analysis (Subsection 3.1.3) of the populations of single cell models. Subsection 3.2.2 and Subsection 3.2.3 will present how the populations of fibres were built and investigated.

3.1 Single cell level

To investigate the effects of the mutation on single cardiac cell electrophysiology and compare them to the activity of a healthy cell, we started our study from choosing a suitable cardiomyocyte model. Then, we moved to the population of models approach in order to include the variability that is inherent in the patients' populations that we are considering, both in healthy and pathological conditions.

3.1.1 Single cell baseline model

As mentioned in Section 2.3.3, the first step in designing a population of models is selecting an appropriate cardiac cell model. For this dissertation, we decided to use the most updated version of the *ORd* model [36]. We implemented a *MatLab* version of the cell model starting from the code provided by Prof. Yoram Rudy and colleagues on their website for the *ORd* model. We replaced the I_{Kr} formulation with the dynamic one proposed by the *FDA* and we scaled the following conductances: I_{Kr} by 1.013, I_{K1} by 1.698, I_{Ks} by 1.870, I_{NaL} by 2.661 and I_{CaL} by 1.007 [15]. Furthermore, we considered the modifications performed by the Oxford *Computational Cardiovascular Science Group* [39], including scaling the transient outward current I_{to} by 2.5 times, modifying the steady state inactivation and recovery from inactivation gates for the fast Na^+ current (h_{ss} and j_{ss}) and setting the current stimulus duration to 1 ms with an amplitude of -53 $\mu A/\mu F$. The conductance of the fast sodium current (G_{Na}) was set at 47 $mS/\mu F$. More details about these modifications are reported in Section 2.3. We decided to keep the modification on the I_{to} because this current has been reported to be larger in the right ventricle (RV) [1] and the RV is the region of the heart most affected by the mutation under investigation, as shown in [43]. Hence, the decision is to focus our study on RV with increased I_{to}. A *CellML* version of the same model was developed. *CellML* is a free, open-source, extensible markup language based on standards for defining mathematical models of cellular function [25]. It was developed to facilitate sharing and re-use of cellular models.

3.1.2 Populations of cells

As in Britton et al. [6] and in many other studies (including [39] [7] [67]), to account for biological variability a population of 10,000 non-diseased human endocardial AP models was created. The 9 conductances of the baseline model that play the biggest role in determining the human ventricular AP were varied (g_{Na}, g_{NaL}, g_{to}, g_{Kr}, g_{Ks}, g_{K1}, g_{NCX}, g_{CaL} and g_{NaK}), assuming that variability is mostly caused by cell-to-cell differences in ion channel density rather than kinetics. All these

were sampled over a range from 0-2 times the baseline value by using the *Latin Hypercube* sampling method. As explained in Britton et al. [7] this range allows models with a wide variety of underlying ionic current configurations to be evaluated and potentially accepted into the population if they passed the calibration process against human physiological data. In fact, it might be that some ionic profiles still produce normal APs in control conditions, which may have increased susceptibility to cardiac abnormalities when the mutation is applied [7].

From a numerical point of view, simulations were performed in *Matlab* using the *ODE15s* solver that solve stiff differential equations. Each simulation was run for 200 beats, to allow the AP to reach its steady state, with a cycle length of 1000 ms (1 Hz pacing frequency). We decided to keep only the values of the membrane potential and their corresponding times from the penultimate and last beat. Moreover, for each model we calculated the biomarker values of the AP trace. The following AP biomarkers (Figure 3.1) were used in this study:

- Peak membrane potential ($VmPeak$) - the peak value of the membrane potential in the first 10 ms.
- Peak membrane time ($VmTime$) - the time at which the peak membrane potential occurs.
- Resting membrane potential (RMP) - the mean membrane potential during the final 20 iterations.
- AP duration at 40/50/90% repolarisation ($APD_{40/50/90}$) - the time to the first point where the membrane potential reaches a given percentage of full repolarisation (FR), defined by the difference between peak and resting membrane potential.
- Triangulation 40-90 difference ($TRId$) - the difference between APD_{90} and APD_{40}.
- Triangulation 40-90 ratio ($TRIr$) - the ratio between APD_{40} and APD_{90}.

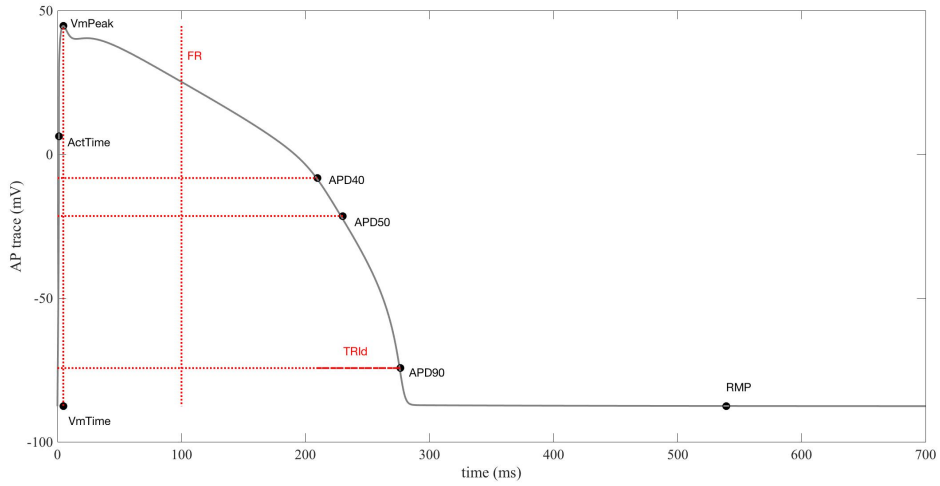

Figure 3.1: The AP biomarkers used in this dissertation, the TTP and $TRIr$ are not shown.

- Activation Time ($ActTime$) - the time of maximum derivative of transmembrane potential.
- Time To Peak (TTP) - the difference between the $VmTime$ and the $ActTime$.

Alternans were classed as a difference in APD_{90} between the final two beats of a simulation of at least 5 ms. If alternans were detected, the model was discarded. From this initial ensemble of candidate models, a calibration process against experimental non-diseased data was performed and only those models in agreement with the data were considered to build the final population.

The experimental data used to perform this process are the same as in Britton et al. [7] (Table 3.1). Those data come from experimental recordings of human APs obtained from human right ventricular trabeculae and papillary tissue preparations perfused and paced at 1 Hz. AP recordings were acquired from these preparations using conventional microelectrode techniques from 62 experiments performed using tissue preparations from 37 hearts. In further detail, the calibration step consisted in calculating the biomarker values for the AP trace of each model and to compare those values with the ranges reported in Table 3.1. The only difference compared to that table, is that we decided to completely remove the constraint on the upper bound of the $VmPeak$ to assure a proper conduction behaviour in tissue, considering

Biomarker	***Minimum***	***Maximum***
$VmPeak\ (mV)$	7.3	39.6
$VmTime\ (ms)$	3.1	14.0
$RMP\ (mV)$	-94.4	-78.5
$APD_{40}\ (ms)$	84.9	323.6
$APD_{50}\ (ms)$	106.6	349.4
$APD_{90}\ (ms)$	178.1	442.7

Table 3.1: Calibration ranges of AP biomarkers.

the role of the tissue coupling in decreasing peak magnitude compared to single cell. Models with biomarker values falling into the calibration ranges were accepted in the final population, also referred to as the control population. Models contained in this population correspond to healthy individuals. The ionic properties of these models (i.e. the scaling factors for the 9 conductances) were saved and then used to build a control population of epicardial cells. Starting from the two control populations, we applied the mutation to obtain two other populations: mutation-carrier endocardial cells and mutation-carrier epicardial cells.

The mutation under investigation is known to affect the sodium current but the exact mechanism remains unclear, as proved by the electrophysiological studies described in Subsection 2.2.2 that report opposing effects on sodium current density and kinetics. We decided to account for the sodium current remodeling by halving the conductance of the fast sodium current and doubling the conductance of the late sodium current, coherently with results obtained on mice by Remme and colleagues [45]. As a result, we obtained four populations (healthy and mutation-carrier; endocardial and epicardial cells), and for each model in each of those population we analysed its AP trace and biomarkers.

3.1.3 Analysis

We decided to analyse only those models that have also passed the calibration step performed in tissue, in order to have four populations in single cell and two populations in tissue built from the same set of parameters. This will allow us to

study by design how a certain combination of ionic conductances affects the AP morphology and properties of a single cell as well as its propagation in tissue.

Partial Correlation Coefficient analysis

Our first analysis consisted in identifying the presence of significant correlations between parameters (i.e. the scaling factors for the 9 conductances) and biomarker values, while controlling for the effects of variability in the remaining parameters. This was necessary because our populations were generated by varying multiple parameters simultaneously. Therefore, as shown by Britton and colleagues in [6] and [7], we used partial correlation to control for the effects of one or more additional variables when looking for correlations between each model parameter and any of the biomarkers computed. This allows us to determine correlations between the properties of individual ionic currents and properties of the whole AP and/or tissue biomarkers [6]. This analysis has been performed using the $MatLab$ function *partialcorr* that returns the sample linear partial correlation coefficients between pairs of variables in the input matrix, controlling for the remaining variables in that matrix.

Delta analysis

In this type of analysis we wanted to show how the differences between the epicardial and endocardial corresponding biomarkers were affected by the mutation. We computed a *delta* value for each biomarker by subtracting/dividing the epicardial value to the endocardial one and then we compared the *delta* values in the two conditions. We also performed a Partial Correlation Coefficient analysis between parameters and *delta* values.

Overlap analysis

This study consisted in analysing the distribution of the biomarkers. We plotted their values (for any healthy and mutation-carrier conditions) in $2D$ plots in order to separate the space into two disjointed regions: one occupied only by mutation-carrier models, and one by models from both conditions, called the

overlap region. We did this for each pair of biomarkers for the endocardial and epicardial populations and then we looked for the best biomarkers to perform this separation. After choosing one or more suitable biomarkers we set a threshold on that/those biomarkers and we compared the ionic properties of the mutation-carrier models belonging to the two regions, considering also the distribution of the ionic properties of the healthy population.

3.2 Tissue level

The following step was progressing the investigation from excitability at cell level to electrical conduction at tissue level. Tissue level represents for us a bridge between in-silico electrophysiological cell models and *ECG* recordings of the electrical signal propagation in the whole heart, which is generally used by clinicians as a routine modality for clinical diagnosis. Moreover, *ECG* recordings are the only experimental data available from mutation-carrier patients, and therefore we needed to generate simulation data of an equivalent type.

3.2.1 Fibre baseline model

Tissue level mathematical models describe the action potential propagation. In this case, the tissue that we consider is a 2 *cm* ventricular fibre. Contributions from the layers of cardiac tissue (endocardium, mid-myocardium and epicardium) will be investigated. Simulations were performed using *Chaste*. *Chaste* - Cancer, Heart And Soft Tissue Environment - is an open source C++ library for the computational simulation of mathematical models developed for physiology and biology [31]. Code development has been driven by two initial applications: cardiac electrophysiology and cancer development. It is a generic and efficient software package, accurately tested and validated, and specifically designed to run on large scale, high performance systems. One important feature of *Chaste* is its capability to performe cardiac electrophysiology action potential simulations using a wide range of models from the Physiome repository [11]. The mathematical formulation of the models is described in *CellML* files, including verification of units consistency

for all variables. From the *CellML* file, the model code is auto-generated at compile or run time, it never has to be manually edited. Ontological annotation are used to identify model variables describing certain biological quantities (membrane voltage, capacitance, etc.) to allow the user to import any relevant *CellML* models into the *Chaste* framework in consistent units and to interact with them via consistent interfaces [11]. Furthermore, *Chaste* provides a wide choice of numerical methods for solving the differential equations that describe the models.

First of all, we simulated a single fibre, the baseline fibre. As mentioned before, it is a 2 cm $1D$ fibre divided in 101 nodes (cells). The 100 elements that made up the fibre represent a sufficiently accurate space discretisation for computing conduction velocity and *pseudoECG* even considering the case of slow conduction. In Figure 3.2 we reported the *pseudoECGs* of a mutation-carrier model characterised by a very prolonged QRS considering a 100-element fibre and 200-element fibre. We can clearly see that the two traces are perfectly overlapping, which justified the numerical accuracy of using a 100-element fibre. Each cell was modelled using the

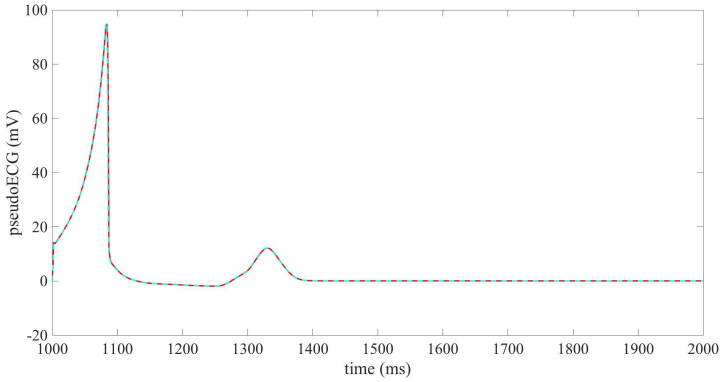

Figure 3.2: Effect of space discretisation on the *pseudoECG*. 100-element fibre (red) vs. 200-element fibre (light blue).

baseline cell model described in Section 3.1.1, which is available in both *Matlab* and *CellML*. The *CellML* version of the model was used within *Chaste* to be converted in *C++*. Then the monodomain model was applied. Before running simulations, few more parameters were varied and explored: the stimulus current, the conductivity of the fibre and the transmural heterogeneity (i.e. the % of endo-,

M- and epi-cells). We chose those parameter values analysing how much each parameter could be varied in order to maintain a conduction behaviour in agreement with human experimental data. In particular, we studied which is the impact of these parameters on the conduction velocity and on the *pseudoECG*. We chose a stimulus current of -120,000 $\mu A/cm^3$, a conductivity of 0.8 mS/cm and we built a fibre made up of 60% endocardial cells and 40% epicardial cells. The effect of the stimulus current on the conduction velocity can be seen in Figure 3.3a, which represents the range over which the value of the stimulus current can be varied while still maintaining a constant conduction velocity. Simulations showed that

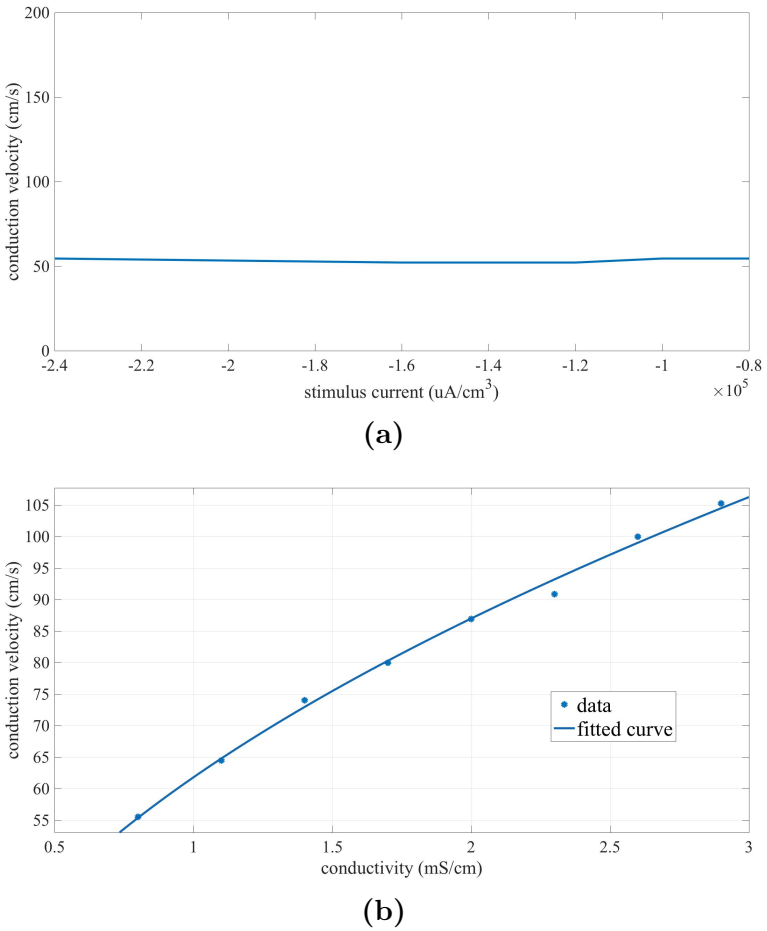

Figure 3.3: Effects of stimulus current (first panel) and conductivity (second panel) on conduction velocity in the fibre.

for a stimulus whose absolute value is greater than -80,000 $\mu A/cm^3$ the current is still conducted until the last node in the fibre, but for a smaller value (e.g.

-60,000 $\mu A/cm^3$) the stimulus current does not reach the end of the fibre and the maximum amplitude of the AP at this node is negative. Given that, in this dissertation, a stimulus of -120,000 $\mu A/cm^3$ (twice diastolic threshold) was chosen. Figure 3.3b shows the effect of the variation of conductivity on conduction velocity. Based on the observations from Figure 3.3b, it was decided to use a conductivity of 0.8 mS/cm, which was considered appropriate in order to get a physiological transmural conduction velocity in control (i.e. 55 cm/s). The final aspect that had to be considered is the distributions of endocardium, mid-myocardium and epicardium. Results of this process are shown in Figure 3.4. Based on this, we decided to omit the presence of M cells. Their presence and role in the myocardium still remain controversial. This is further supported by the fact that, given their longer APD, the presence of these cells should be reflected on the $Tend$ point of the $pseudoECG$, whilst this is not observed given the normalising effects of the tissue coupling. Moreover, our choice of omitting the presence of M cells is further based on Taggart's work. In fact, in a review published in 2014, Taggart and colleagues [51] described how acquisition of basic electrophysiological data in the intact human heart is essential to drive and complement experimental work in animal and in-silico models. In particular, they reported the work performed by several laboratories investigating whether different electrophysiological properties in cells isolated from endocardial, mid myocardial and subepicardial regions persisted in intact hearts (electrically and mechanically well coupled). They demonstrated, using a plunge electrode for obtaining transmural recordings in patients during surgery, an absence of any electro-physiological evidence of mid myocardial M cells in humans in the left ventricular wall [53]. The contrast between these results and the clear differences between M cells and endocardial and epicardial cells regularly observed in studies in isolated cells, was attributed to electrotonic cancellation of transmural electrical gradients in the intact left human ventricle [52]. In figure 3.4 a clear elevation of the ST segment can be observed when 80% of endocardial cells and 20% of epicardial cells are considered. The same happens with 70% of endocardial cells and 30% of epicardial cells. Therefore, given the aim of this study,

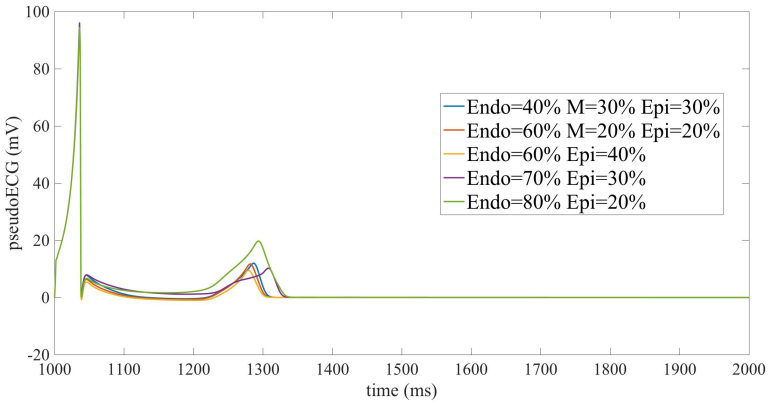

Figure 3.4: How the transmural heterogeneity affects the *pseudoECG* of the fibre.

the baseline fibre model was constructed with 60% of endocardial cells and 40% of epicardial cells. In fact, the exact partition of the cells is not the type of information that we want to model in this dissertation, while it is more important taking into account the morphology of the *pseudoECG* to provide a better characterisation of the phenotypic manifestation of the disease.

3.2.2 Populations of fibres

After establishing the setup for the baseline fibre model we could run the simulation and calculate the *pseudoECG* of the fibre and its corresponding biomarkers. The following step was introducing the variability. The stored parameters set (scaling factors for the 9 conductances varied) used to build the populations in single cell was now used to construct two populations of fibres, the control population (representing the healthy individuals) and the mutation-carrier population. Tissue simulations were then performed.

After obtaining the results, we performed a calibration process on the healthy population in order to accept only those models with a *pseudoECG* trace in agreement with human data. We implemented a two step calibration process studying both the peak voltage in the last node and the conduction velocity in the whole fibre. We checked that the peak voltage of the last node reached 0 mV to ensure the absence of conduction failure, and then we discarded the models with a conduction velocity outside the range [35 55] cm/s. Only those models that

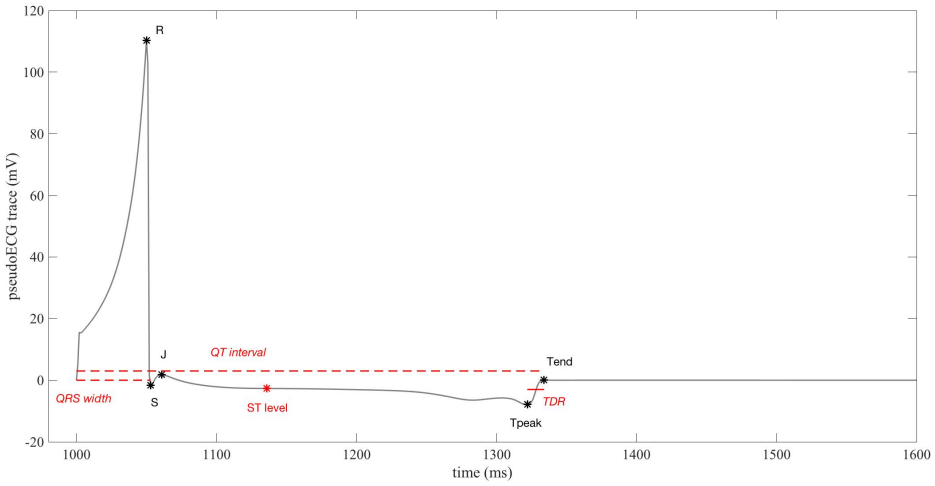

Figure 3.5: *PseudoECG* biomarkers used in this dissertation (*iCEB* not shown).

passed these calibration steps were accepted in the final populations of fibres. We then analysed the *pseudoECGs*, considering the following time points of interest in order to compute the biomarkers:

- R point - the point corresponding to the peak of the trace.
- S point - the first point after the R point where the derivative of the trace is greater than -0.5.
- J point - the point corresponding to the first peak (greater than 0) between the R point and the following 200 ms.
- T end point - the first point starting from the end of the trace where the absolute value of the derivative is greater to 0.03.
- T peak point - the point corresponding to the peak (positive or negative) between 1100 ms and the T end point.

We also considered the possible presence of biphasic T waves, in case that a negative peak was detected in the 80 ms that precede the positive T peak point, with an amplitude at least half of the T peak.

After that we computed the following *pseudoECG* biomarkers (Figure 3.5):

- QRS width ($QRSwidth$) - the time that it takes for the signal to get from the stimulus time (Q wave) to the S point.
- QT interval ($QTinterval$) - the time that it takes for the signal to get from the stimulus time (Q wave) to the T end point.
- ST level ($STlevel$) - the membrane voltage of the middle point occurring between the R point and the T peak point.
- Transmural Dispersion of Repolarisation (TDR) - the difference between the T end and T peak points.
- Index of Cardiac Electrophysiological Balance ($iCEB$) - the ratio between the QT interval and the QRS width.

The $iCEB$ is a novel biomarker proposed by Hua Rong Lu and colleagues [26] [48] to predict drug-induced cardiac arrhythmias, including ventricular tachycardia/ventricular fibrillation (VT/VF) and Torsades de Pointes (TdP) together with non-TdP like VT/VF. They speculated that: increases/decreases in QT or JT-interval were proportional to those in effective refractory period (ERP), and also changes in QRS were similar to those in conduction velocity. Therefore, the $iCEB$ derived from the ECG, should have been the equivalent of the classic λ (ERPxCV), and significant changes in $iCEB$ may have reflected an imbalance in cardiac electrophysiology, and therefore predicted cardiac arrhythmias.

3.2.3 Analysis

For the analysis of *pseudoECG* biomarkers, all models in the healthy population were considered, but only those in the mutation-carrier population exhibiting a proper propagation behaviour (absence of conduction failure), were retained for *pseudoECG* biomarker quantification. The failure was taken into account considering the peak voltage of the last node (smaller than 0 mV) or conduction velocity lower than 20 cm/s. The cellular mechanisms underlying conduction failure in the mutation were still studied.

Biomarker	***Carrier***	***Non-Carrier***
heart rate (bpm)	75±19	74±17
PQ interval (ms)	181±28	154±26
QRS duration (ms)	102±17	88±13
QTc interval (mV)	453±32	397±22
max ST elevation $V1-V3$ (ms)*	0.5(0.22-1.00)	0.25(0.00-0.62)

Table 3.2: ECG characteristics of family members. *Median(interquartile range). Confidential.

Delta analysis

The first analysis on the *pseudoECG* was focused on the morphology of the traces in order to highlight potential trends introduced by the mutation. We performed an analysis on the points of interest of the *pseudoECG* mentioned in Subsection 3.2.2. We computed the difference between the coordinates of each point in the two conditions to show how the mutation affects the *pseudoECG* morphology.

Comparison with the clinical data

The clinical data for the 1795*insD* family provided by our collaborators are heart rate, *PQ* interval, *QRS* duration, *QTc* interval and *ST* elevation (Table 3.2) reported as mean ± standard deviation. Those data are derived from a real *ECG* and therefore cannot be directly compared to our simulation data (whole heart vs. 1D fibre simulations). A possible good way to overcome these scale differences is to consider the ratio between each biomarker value in the two conditions (healthy and mutation), and then compare the ratios obtained for the clinical and simulation data.

Partial Correlation Coefficient analysis

We identified the presence of significant correlations between parameters (i.e. the scaling factors for the 9 conductances) and tissue biomarker values, while controlling for the effects of the remaining parameters. We used partial correlation to control for the effects of one or more additional variables when looking for correlations between each model parameter and any of the biomarkers computed, as previously described for the *PCC* performed in single cell. This allowed us to determine correlations between the properties of individual ionic currents and properties of the *pseudoECG*.

Overlap analysis

Similar to the analysis in single cell, this one aimed to investigate the space distribution of the *pseudoECG* biomarkers. Particularly, we focused on the QT interval and QRS width. We plotted their values for both conditions and we identified the region of overlap, in which models of both conditions were present. Then, models belonging to that region were studied in terms of biomarkers (AP and *pseudoECG* biomarkers) and ionic properties.

Rate-dependent study

Clinical data from our collaborators show that bradycardia is an important factor to consider in this investigation, in fact family members are frequently treated with pacemakers to prevent (mostly nocturnal) bradycardia with associated excessive QT prolongation. To do so, we ran tissue simulations with a longer cycle length of 1500 ms. We then performed the same analysis previously described for a cycle length of 1000 ms to study the effect of the mutation when the heart frequency was lower (e.g. during the night).

4
Results

Contents

This chapter will describe all the results achieved in this investigation. It is divided in two main sections to separate between the up-scale and down-scale investigations into the mechanisms of the *SCN5A-1795insD*. The combination of the ionic-, cellular- and tissue-properties of the models are investigated following a bidirectional flow in the analysis, from ion to tissue (up-scale) and vice versa (down-scale), in order to explain the phenotypic variability of the disease. The Figure 4.2 reports the workflow of this thesis.

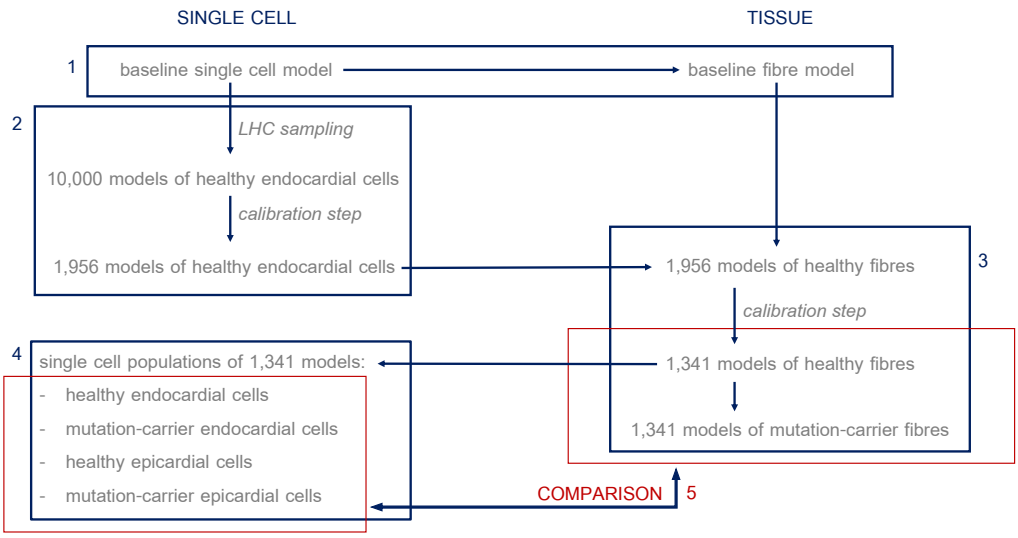

Figure 4.1: Workflow of this thesis.

4.1 Up-scale mechanisms of the *SCN5A-1795insD* mutation

4.1.1 Single cell

As described in the methods (Chapter 3), starting from the baseline single cell model we constructed a population of 10,000 models of healthy endocardial cells. We calibrated the population using the experimental data described in Subsection 3.1.2 and we discarded all the models with the AP biomarker values outside the calibration ranges considered. The results of this first step are reported in Figure 4.3, in which we can observe the AP traces of the entire initial population (10,000 models) and those of the 1,956 accepted models. Figure 4.3 shows the value of the scaling factors for the 9 model parameters that have been varied, which represent the ionic properties of the models accepted in the population. These results show that the calibration performed in single cell without any restriction on the upper bound of the $VmPeak$ leads to accepted values of the G_{NA} that are within a narrower subset of the sampled range: lower values are discarded since they do not generate a proper AP upstroke. On the other hand, the majority of accepted parameter values span closely the entire range of sampled values (up to $\pm 200\%$ of

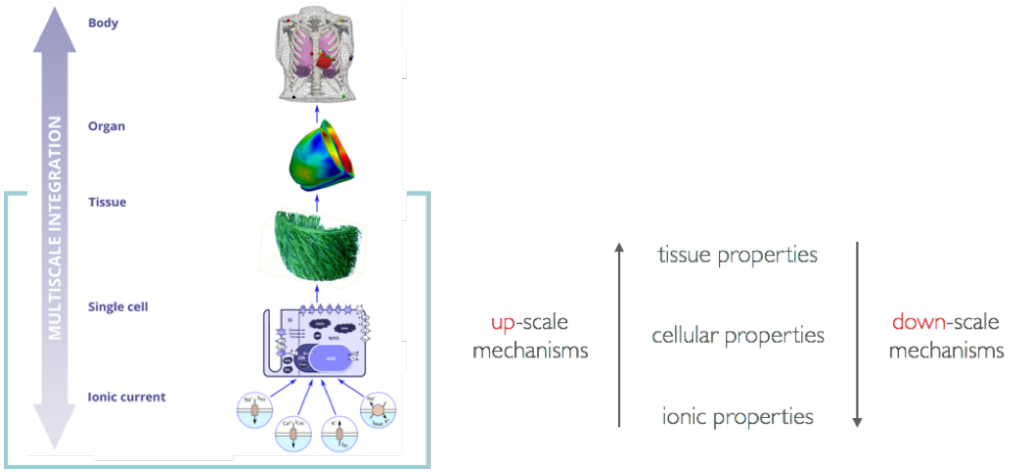

Figure 4.2: The multi-scale approach. The up-scale and down-scale flows of the analysis.

their values from the original parameter set of the baseline model). The matrix

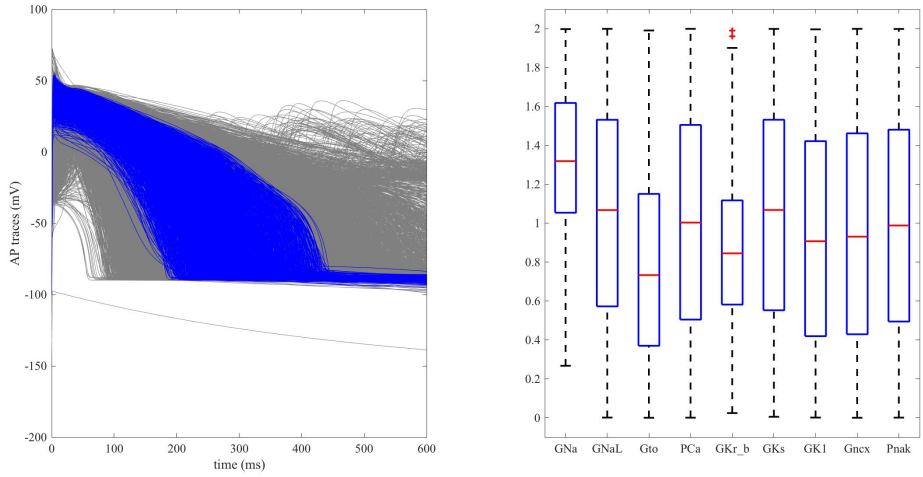

Figure 4.3: *AP* traces and ionic properties of the accepted models. Left panel: *AP* traces of the accepted models (1,956 models, in blue) against the entire initial population (10,000 models, in grey). Right panel: scaling factors for the model parameters that define the ionic properties of the accepted 1,956 models.

with the ionic properties defines the features of the single cell models as well as the features of the fibres populations. Our aim is to understand how the ionic and cellular properties associated to the *SCN5A-1795insD* mutation reflect themselves in tissue. Populations with the same number of models at both single and tissue levels are thus required to allow for such mechanistic investigations. Therefore, we discarded from this single cell population of 1,956 models those that did not pass

the calibration step in tissue. In other words, we used the matrix with the ionic properties of these 1,956 models to build a population of 1,956 healthy fibres and then we calibrated it (see Subsection 3.2.2 for additional details). From this tissue calibration step we finally obtained the number of models that made up the control population: 1,341 models. From the ionic properties of these 1,341 models we built the other single cell and fibre populations carrying the mutation. The results of the calibration process implemented in tissue will be presented in the next section. Here, we report the results for the single cell populations. These populations are four: healthy endocardial cells, healthy epicardial cells, mutation-carrier endocardial cells and mutation-carrier epicardial cells, all made up of 1,341 models. The AP traces of these populations are reported in Figure 4.4. Their AP biomarkers are shown in Figure 4.5. The effects of the mutation are consistent in the two myocardial

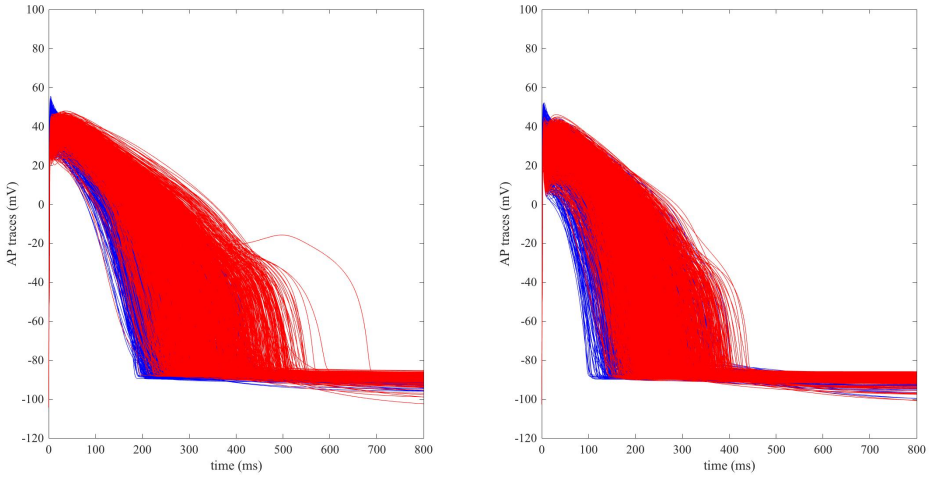

Figure 4.4: AP traces of the endocardial (left panel) and epicardial (right panel) cells in the healthy (blue) and mutation-carrier (red) populations.

layers: the peak membrane voltage is reduced and delayed, the $APDs$ are prolonged, there are no significant differences in terms of morphology of the AP since the two biomarkers that account for it, the $TRIdiff$ and $TRIratio$, do not significantly change in the two conditions, the $ActTime$ in slightly delayed and the TTP in significantly increased when the mutation is introduced (Figure 4.5). More in details, the mutation under investigation involves the cardiac sodium channel gene, affecting

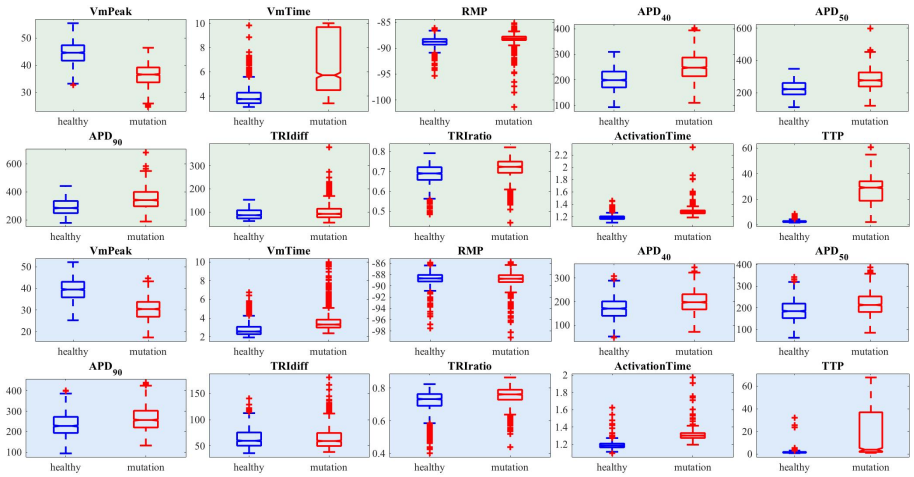

Figure 4.5: *AP* biomarker values of the endocardial (first and second rows, light green background) and epicardial (third and fourth rows, light blue background) cells in the healthy (blue) and mutation-carrier (red) condition.

the sodium current and inevitably the upstroke of the *AP*. This is reflected by the two cellular level biomarkers $VmPeak$ and $VmTime$ in both the endocardial and epicardial layers. The $VmPeak$ is significantly decreased after the introduction of the mutation, and also delayed. In particular, it is more delayed in the endocardial cells compared to the epicardium because in the epicardial layer there is a stronger transient outward potassium current to counteract the upstroke phase. The bigger TTP values in the endocardial cells reflect that the maximum voltage of the *AP* trace occurs after several millisecond from the $ActTime$. That is less significant in the epicardial layer due to the stronger transient outward potassium current. So, even if the overall trend of the biomarkers in the two myocardial layers is the same, the ratio between the mutation-carrier and healthy conditions is different, i.e the mutation affects the two layers in a different way. This transmural effect of the disease will be better analysed in the subsequent analysis but it has been clear to us from the beginning of the investigation and is one of our main findings.

We performed several analysis on the *AP* biomarkers. First of all we identified the eventual presence of significant correlations between parameters and biomarker values, while controlling for the effects of variability of the remaining parameters. The results of the *PCC* analysis are reported in Figure 4.6 and Figure 4.7. For

each biomarker, multiple parameters show significant partial correlations. The differences between the endocardial and epicardial cell populations mainly reflect the different weights of each current in the two layers. G_{Na} and G_{NaL} are the

(a)

(b)

Figure 4.6: *PCC* results for the endocardial single cell populations. First panel: healthy. Second panel: mutation-carriers.

conductances directly affected by the mutation, the first one is halved and the second one is doubled. Therefore, even if G_{Na} still correlates strongly and positively with the peak membrane potential, the magnitude of the correlation is inferior in the mutation-carrier populations. On the other hand, the contribution of the G_{NaL} to the peak potential is bigger in the mutation-carriers. Since the contribution of the G_{Na} is weaker in that population, the P_{Ca} has now a more important role in sustaining the peak. For the same reason, i.e. it is halved, the G_{Na} also contribute

(a)

(b)

Figure 4.7: *PCC* results for the epicardial single cell populations. First panel: healthy. Second panel: mutation-carriers.

less to the activation time. On the other hand, since it is doubled, the G_{NaL} provides now a bigger contribution to the time to peak in the mutation-carriers. The G_{to} correlates negatively and strongly to the peak voltage, but its contribution is inferior in the mutation-carrier populations, due to the reduced peak membrane voltage in that population. Its contribution to the $VmTime$ is inferior as well for the same reason. In particular, the G_{to} contribution to those biomarkers is always stronger in the epicardium than in the endocardium, due to its bigger value in that layer. In general, the trend between the healthy and mutation-carriers is the same in the two layers. The G_{ncx} contribute differently to the $VmPeak$ and $APDs$ in the two conditions. In the healthy one it correlates negatively to the peak membrane

potential (it works in the reverse mode during the upstroke and so it is an outward current) and positively to the $APDs$ when it's an inward current. On the other hand, the magnitude of the correlation in the mutation-carriers is reduced a lot. In fact, from the analysis on the AP and I_{NaCa} traces we observed that, due to the reduced voltage, the reverse mode of the I_{NaCa} is closing faster and therefore that inward current is smaller during the upstroke, contributing less to the voltage peak in the mutation-carrier populations. The G_{NaL} plays a bigger role in sustaining the $APDs$ in the mutation-carriers due to the direct effect of the mutation, while the P_{Ca} has now a weaker contribution to the $APDs$. In fact, the membrane voltage is reduced and therefore the I_{CaL} voltage-dependent gating is affected leading to a reduced I_{CaL}. So, multiple parameters influence each biomarker even if individual parameter values are still important for determining the exact balance of currents and, indeed, the specific AP properties of each model.

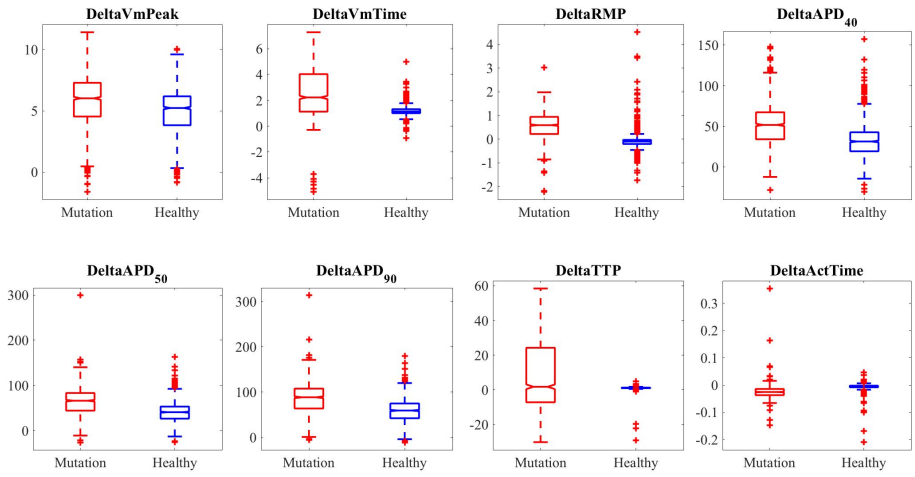

Figure 4.8: *Delta* values between each corresponding AP biomarker in endocardium and epicardium, healthy models in blue and mutation-carrier models in red.

In a subsequent analysis (*Delta* analysis) we considered the differences between the epicardial and endocardial corresponding biomarkers to study how the mutation affects the dispersion between the two layers. The results are shown in Figure 4.8. Each *delta* value is computed subtracting from the endocardial biomarker the epicardial one, where positive values mean that a biomarker is bigger in endocardium.

The median of the distribution reflects the dispersion between the two layers. Results in Figure 4.8 show that the mutation-carrier condition is generally characterised by a bigger endocardial values. That is an additional proof that the mutation affects the two myocardial layers in a different way.

We then studied the space distribution of the biomarkers and the ionic properties of the models belonging to the different regions, i.e. showing different biomarker values. We did this for each pair of biomarkers for the endocardial and epicardial populations. All the extended results are reported in Appendix A.1. For the endocardial cells the best biomarkers are those related to the peak voltage ($VmPeak$, $VmTime$ and TTP) but also all the $APDs$ (Figure A.1, Figure A.2, Figure A.3, Figure A.4). For the epicardial cells the most suitable biomarkers for this analysis are the $VmPeak$, $VmTime$ and TTP. That highlights the first main outcome: the main effect of the mutation in terms of AP prolongation occurs in the endocardial layer and not in the epicardial one. This is a really interesting point since the difference in the two layers may lead to a dispersion in the myocardium that can be revealed in tissue.

4.1.2 Tissue

We ran the simulations and calculate the *pseudoECG* of the fibre and its corresponding biomarkers. In order to progress the analysis from the single fibre to a population of fibres we used the ionic properties of the 1,956 models that have passed the calibration step performed in single cell. We built a population of 1,956 healthy fibres. Then we performed a further calibration step with the purpose of discarding the fibres that show a conduction behaviour not in agreement with human physiological data. We checked that the maximum amplitude of the last node of the fibre reached 0 mV and we kept only the models with a conduction velocity in the physiological range [35 55] cm/s. In Figure 4.9 we can see the result of this calibration step. That provided us 1,341 models. We applied the mutation on top of these models and we obtained a population of 1,341 fibres carrying the mutation (Figure 4.10). As it can be easily inferred from Figure 4.10, not all traces of the models carrying the mutation can be studied in terms of biomarkers due to their

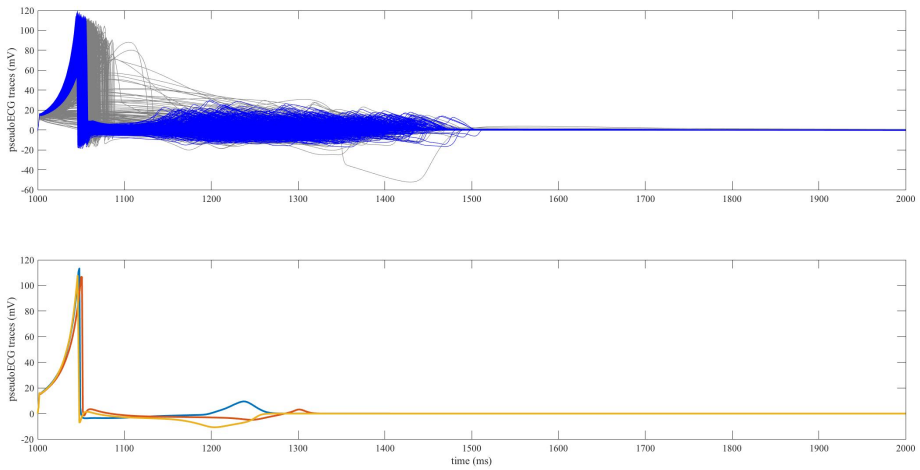

Figure 4.9: The result of the calibration step performed in tissue. First panel: *pseudoECGs* of the initial population of 1,956 healthy fibres (grey) against the 1,341 *pseudoECG* traces of the accepted models in the healthy population (blue) after the calibration. Second panel: *pseudoECGs* of models showing a positive (blue), negative (yellow) and biphasic (orange) T wave.

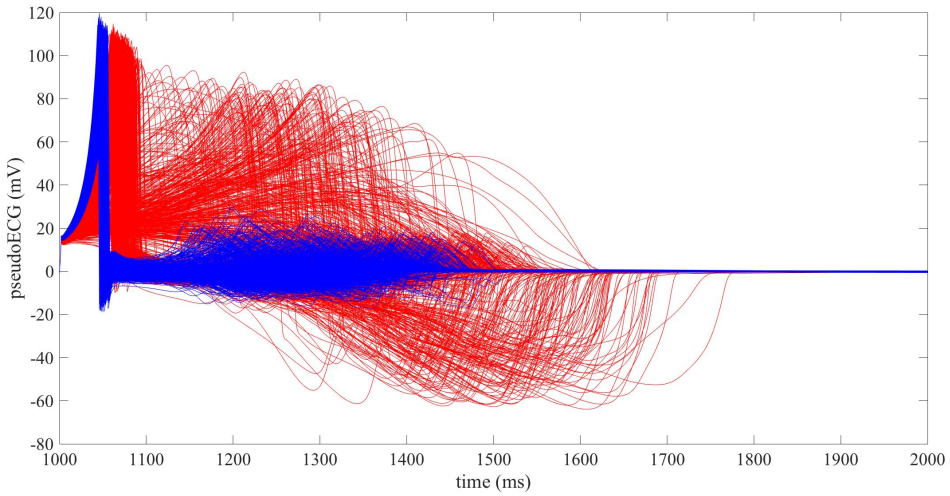

Figure 4.10: *pseduoECG* traces of the 1,341 fibres in the healthy (blue) and mutation-carrier (red) populations.

abnormal *pseudoECG* morphology. Those models are in fact showing a failure in the conduction due to the introduction of the mutation, which is a known symptom of these patients. This does not imply that the entire ventricle would manifest a conduction block, since this simulation involves just a 2 *cm* fibre, but it is a realistic representation of one of the most common features of the disease under investigation.

The models with a conduction failure were therefore not included in the subsequent analysis of biomarkers. That led to a total of 941 mutation-carrier models accepted for the analysis of the biomarkers (Figure 4.11). In Figure 4.12 we can observe the

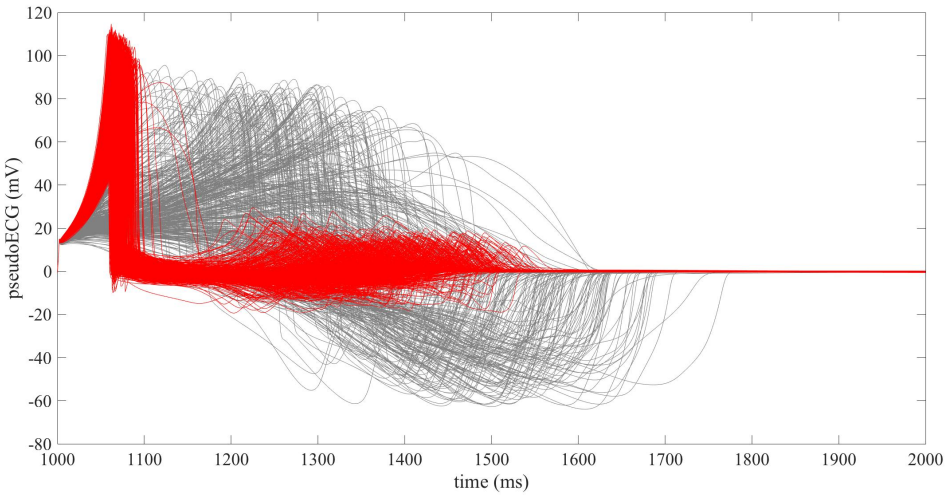

Figure 4.11: *pseduoECG* traces of the 941 (red) out of 1,341 (grey) fibres in the mutation-carrier population accepted for the analysis of the tissue biomarkers.

box plots for the tissue biomarkers of the two populations of fibres. From a first qualitative analysis we can say that the mutation-carrier population is characterised by a wider QRS and longer QT. The $iCEB$ index is smaller in the mutation-carrier population, reflecting the relevant effect of the mutation in increasing the QRS width. However, the difference in the $iCEB$ between the two populations is not very significant since both QRS and QT are both affected by the mutation. The TDR is bigger in the mutation-carrier population while we cannot see significant differences in the ST level. The last panel in Figure 4.12 reports the conduction velocity (CV) of both populations, showing a clear reduction in the mutation-carrier one.

Since the changes in the morphology of the *pseudoECG* between the two conditions are quite consistent in all models, we quantified these changes analysing the relevant points in the *pseudoECG* traces. We considered the time points and amplitudes of each point and we subtracted the corresponding coordinates in the two conditions in order to highlights potential trends (Figure 4.13). The results show that the R point is always lower and delayed, reflecting the impairment of the AP upstroke

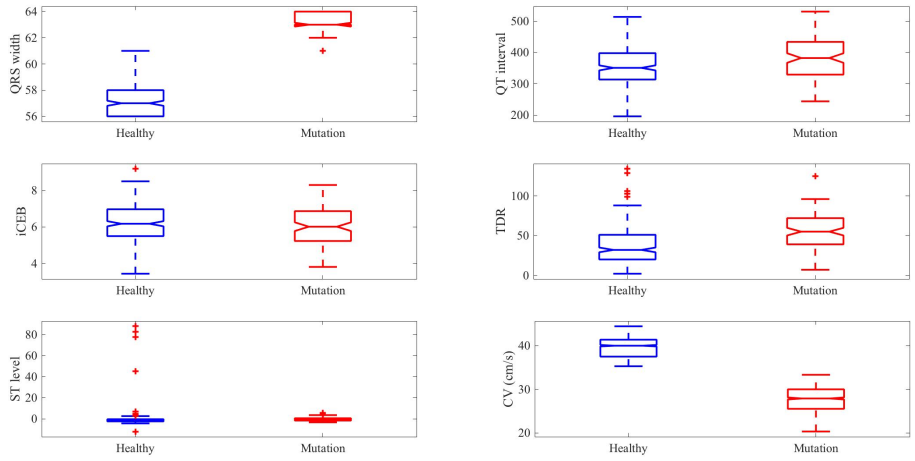

Figure 4.12: Box plots of the tissue biomarkers of the two populations of fibres, healthy in blue and mutation-carrier in red. The left bottom panel also show the conduction velocity in the two populations.

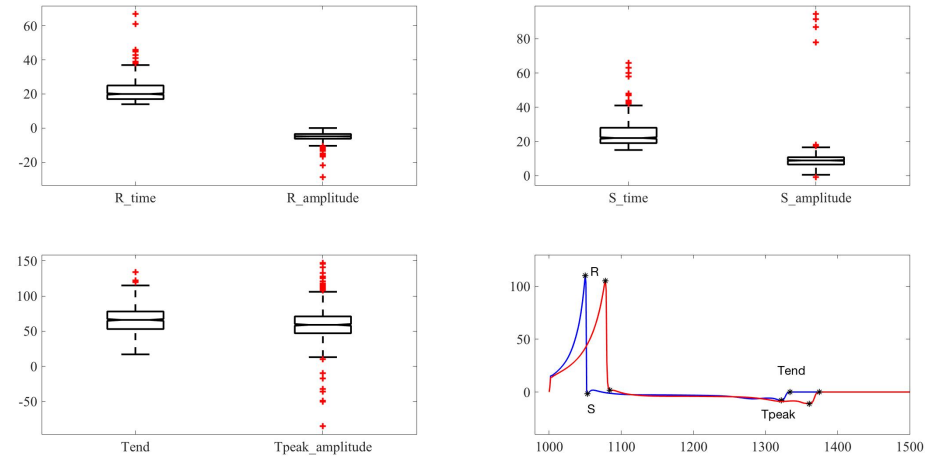

Figure 4.13: Analysis of the relevant points of the *pseudoECG* traces in the two conditions. The box plots show the values obtained for each point as the difference between its coordinates in the mutation-carrier model and in the healthy corresponding one. (Delta=Mutation-Healthy)

observed in single cell and the lower conduction velocity in the mutation-carrier models (Figure 4.12). The S point is usually higher and delayed. The points that define the TDR, the $Tpeak$ and $Tend$, are also generally delayed by the mutation.

After this initial analysis on the simulation data, we studied our results in light of the clinical data. Even if it is not possible directly compare the two different sets

of results (clinical and simulation), we can investigate the ability of our results to represent the clinical data. In order to do so, we considered the QT interval and QRS width and we computed the ratio between the mean values of each biomarker in the two conditions, both for clinical and simulation data (Table 4.1). We can consider our simulation data in agreement with the clinical one, even if the values shown in Table 4.1 are slightly different. In fact, the reason why that happens is that the modelling of the whole ventricle is simplified into a 1D 2 cm fibre characterised by a strong I_{to}. In other words, we are modelling a single fibre from the RV that is known to be the part of the heart most affected by the disease. At the same time, we are missing the contribution from the left ventricle (LV) that is instead less affected and indeed can reduced the manifestation of the disease. This is the reason why our tissue model shows a strong manifestation of the disease. In terms of QT, our simulation results quantitatively reproduced the QT prolongation in clinical data with very good accuracy. We do believe that our simulation data are indeed strong enough to provide insight on the overlapping effects of the *SCN5A-insD* mutation.

Type of data	***QRS ratio***	***QT ratio***
Clinical	1.1591	1.1411
Simulation	1.4798	1.1925

Table 4.1: Comparison between the clinical and simulation data. The values are the ratio between the mean value of the biomarker in the mutation and healthy conditions. (Ratio=Mutation/Healthy)

4.2 Down-scale mechanisms of the *SCN5A-1795insD* mutation

As previously reported, the Dutch family carrying the *SCN5A-1795insD* mutation displays profound variability in type and severity of symptoms. Among these patients there is a huge variability in their electrocardiographic signs, i.e. some carriers do not display any overt ECG changes, while others have clear conduction disease (PR and QRS prolongation) and/or QT prolongation. Also it is unclear why some patients have mostly conduction abnormalities while others have mostly

repolarisation abnormalities. The clinal data provided by our collaborators clearly show this phenomenon (Figure 4.14).

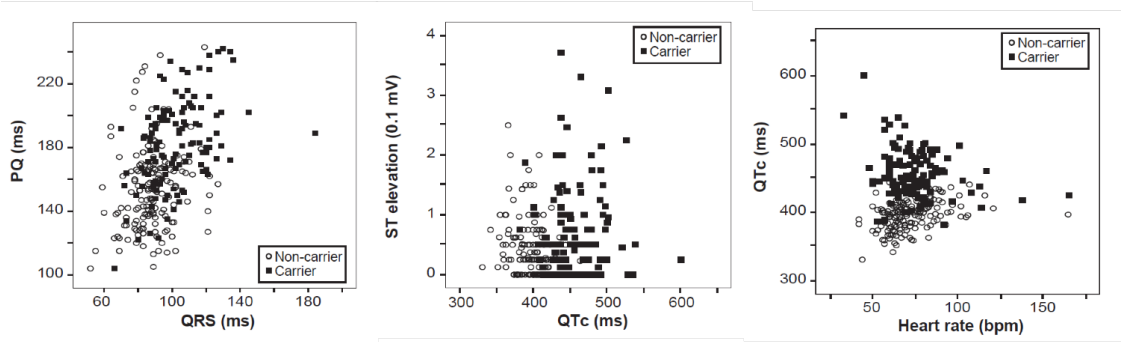

Figure 4.14: The overlap in the *ECG* biomarkers. Clinical data.

We developed a fibre tissue model of *SCN5A-1795insD* carriers in order to be able to investigate the phenotypic variability shown by these patients and gain more insight into the mechanisms underlying the mutation. As it can be observed in Figure 4.15 and Figure 4.16 a subset of mutation-carrier models is characterised by QT interval and QRS width values similar to those of the healthy models, while the remaining mutation-carrier models show a clear disease phenotype, with a prolonged QT interval and/or wider QRS. The overlap in terms of QRS in our simulated results is less evident compared to the clinical data. This is probably due to the fact that our fibre model represents the most affected part of the entire ventricle. Adding the contribution of the less affected part, i.e. the LV, would have resulted in less prolonged QRS interval. Our simulated results are indeed in agreement with the main clinical manifestations of the disease and its phenotypic variability. This supports that the considered ionic remodelling is a coherent representation of the disease, and clearly highlights the main challenges that clinicians and researchers face. Being able to classify a subject as healthy or potential mutation-carrier is of primarily importance. In fact, if a subject presents signs of QT or QRS prolongation, it is clear that additional genetic testing might be necessary. However, what if those values are within the normal ranges? Is there any other biomarker useful to classify the subject? On the other hand once it is known that a patient is

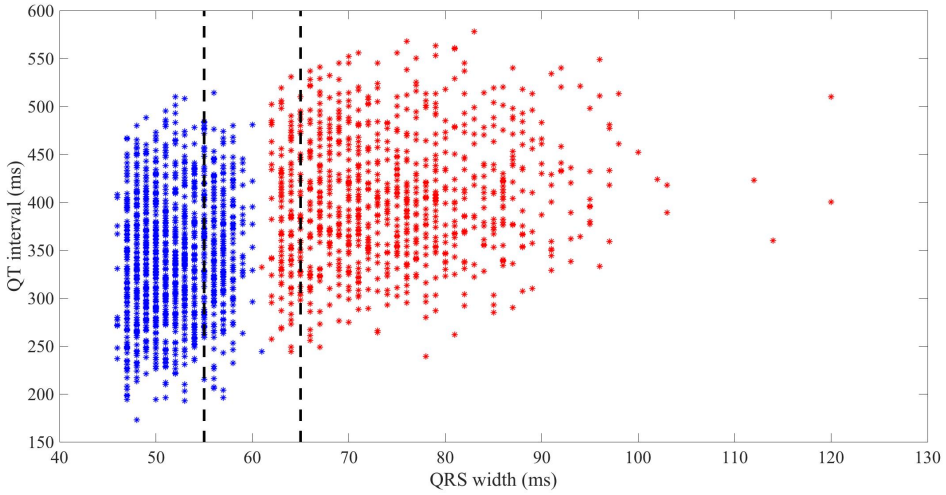

Figure 4.15: The overlap in the *pseudoECG* biomarkers. The dotted lines delimit the overlap region in terms of QRS width, defined as 60 ms ± 5 ms. Simulation data.

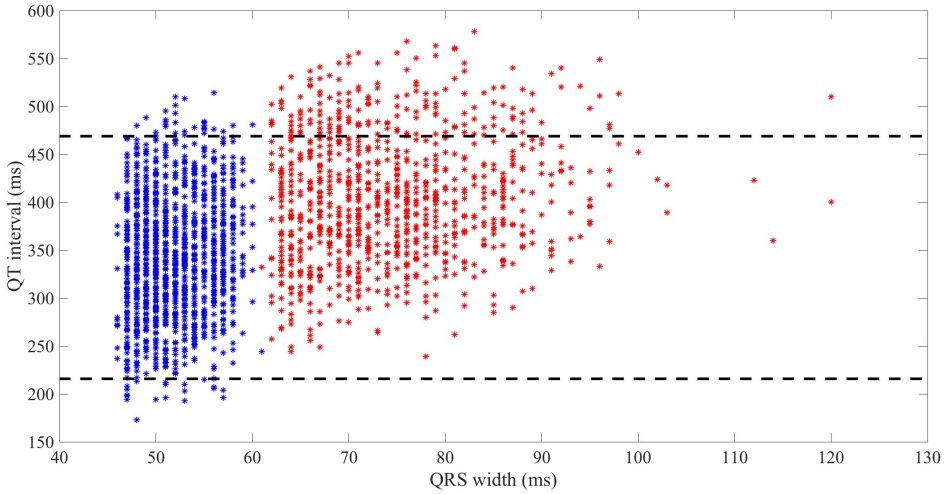

Figure 4.16: The overlap in the *pseudoECG* biomarkers. The dotted lines delimit the overlap region in terms of QT interval, defined as mean ± two times the standard deviation of the QT values in the healthy population. Simulation data.

carrying the mutation, it is also important to understand which are the mechanisms behind the variability in manifestation of the disease.

The QRS seems to be a more useful biomarker to perform a first classification of the subjects. Given the simulated results, we defined the overlap region as the region in which the models are showing a QRS value of 60±5 ms (Figure 4.15). It is worth remembering that the mutation-carrier models in that graph are only those in the mutation-carrier population that do not display conduction failure.

We considered the properties of the models belonging to the various regions of the biomarkers space shown in Figure 4.15 taking into account three different levels of analysis and the combination of thereof: from tissue-, cellular- to ionic-level (top-bottom analysis). From a mechanistic point of view, the combination of these properties is expected to explain why a certain model belongs to a particular region, i.e. why a patient carrying the mutation shows a particular phenotype. Moreover, this analysis is also useful in terms of diagnosis, to investigate which biomarkers can be considered in a situation in which a potential carrier shows a phenotype similar to a healthy subject. From now on we will refer to the region in which the models show similar values in terms of QRS width as the overlap region.

4.2.1 Conduction abnormalities

A weak fast sodium current is the main determinant for conduction failure under the *SCN5A-1795insD* mutation

When we introduced the ionic remodelling associated with the mutation in the healthy population (halving the fast sodium current and doubling the late sodium current), an immediate effect was the conduction failure exhibited by some of the models, in accordance with the clinical data that report conduction abnormalities as one of the main symptoms. Figure 4.11 shows the AP traces of mutation-carrier models with a conduction failure against those of mutation-carrier models with a proper conduction behaviour. Compared to the other mutation-carrier models, the analysis performed on these models revealed an underlying very weak fast sodium current, as well as a reduced L-type calcium current (Figure 4.17). The combination of thereof leads to a very small inward current that is not enough strong to sustain the AP propagation is tissue. In addition, the transient outward potassium current is very strong, which can also affect the CV by two different mechanisms. The first one is opposing the fast sodium current and therefore reducing the CV. The second one is decreasing the L-type calcium current, acting on its activation. In fact, the gating variable for the L-type calcium current activation is voltage dependent, therefore, if the membrane voltage is decreased due to a bigger transient outward

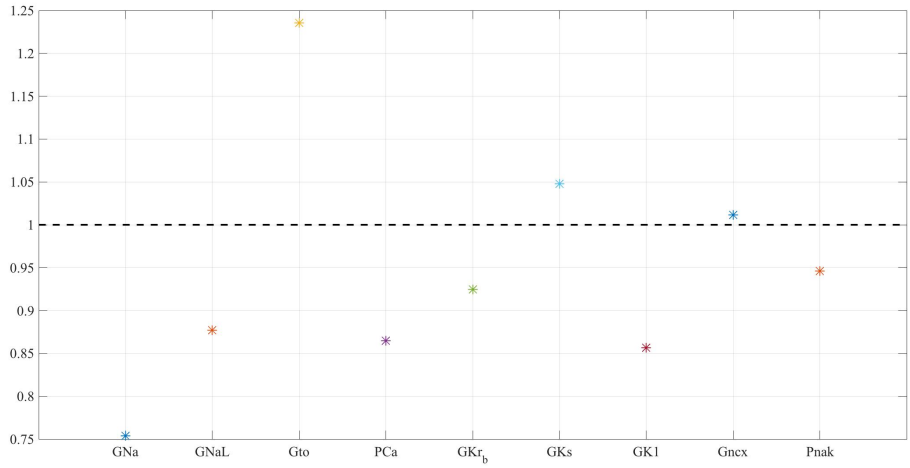

Figure 4.17: Distribution of the ratios between the median values of the parameter scaling factors in the mutation-carrier models with a conduction failure and in those with a proper conduction. The main role in determining the conduction failure is played by the fast sodium current.

potassium current, the L-type calcium current is decreased as well. The inward rectifier potassium current is also very weak and it can therefore affects the sodium current through its driving force by modulating the resting membrane potential, as it has already been reported in [28].

A strong fast sodium current preserves the conduction even in the presence of the mutation

When the mutation is introduced those models with a strong enough fast sodium current are able to preserve the conduction. Moreover, a subset of them show a range of values for the QRS width very similar to the one of the healthy population, as it is shown in Figure 4.18. The reason why these models still present a quite narrow QRS is the presence of a very strong fast sodium current (Figure 4.18). Even when it is halved due to the mutation, that current remains strong enough to avoid a conduction failure, and more interestingly, it is fundamental to sustain a QRS in overlap with data from healthy subjects.

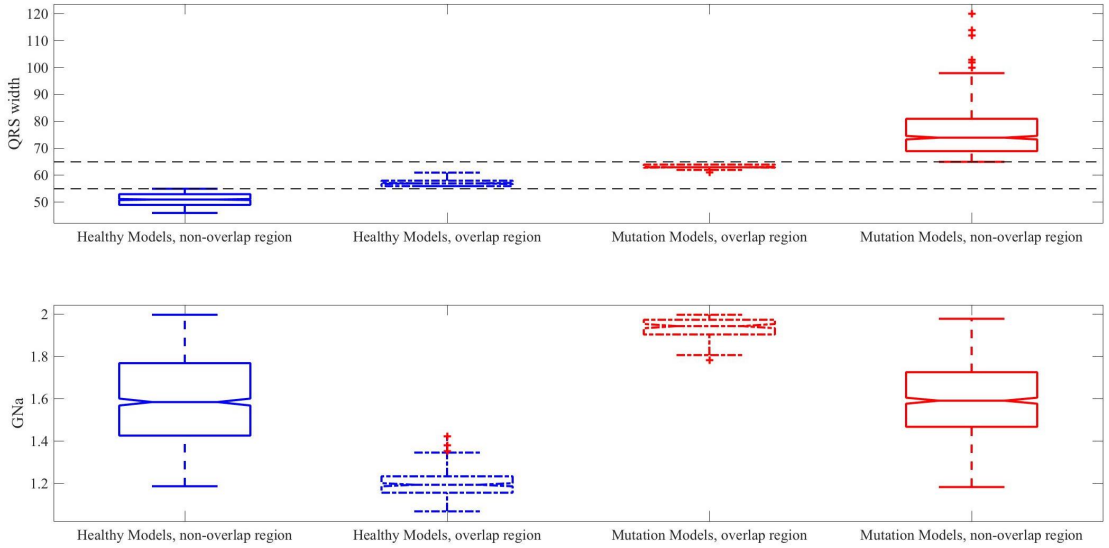

Figure 4.18: First panel: box plots of the *QRS* width values for the healthy (in blue) and mutation-carrier (in red) models in the non-overlap (first and last columns) and overlap (central columns) regions. Second panel: box plots of the scaling factors for the fast sodium current for the healthy (in blue) and mutation-carrier (in red) models in the non-overlap (first and last columns) and overlap (central columns) regions. The effect of the mutation on the fast sodium current is not shown in the picture to highlight the strong baseline value of the current before applying the mutation.

4.2.2 Repolarisation abnormalities

QT interval prolongation. Calcium blocker might not have a positive effect for the *SCN5A-1795insD* mutation

QT interval prolongation and repolarisation abnormalities are electrocardiographic signs of the disease as well. Models representing mutation-carrier patients reflect those symptoms. In fact, we can observe a prolongation in the *QT* interval (Figure 4.16 and Figure 4.19), mostly for those model outside the overlap region. To better understand which are the currents involved in the *QT* interval prolongation, we performed a *PPC* analysis, as described in Subsection 3.1.3, between the model parameters and the tissue biomarkers. The results demonstrate that the currents playing the most relevant role are the rapid delayed rectifier potassium current, the late sodium current, the L-type calcium current and the slow delayed rectifier potassium current (Figure 4.20). What is really relevant here is identifying those currents that correlate differently in the two populations. The currents that are for their nature mainly involved in sustaining the *QT* interval, mainly the I_{Kr}, do not

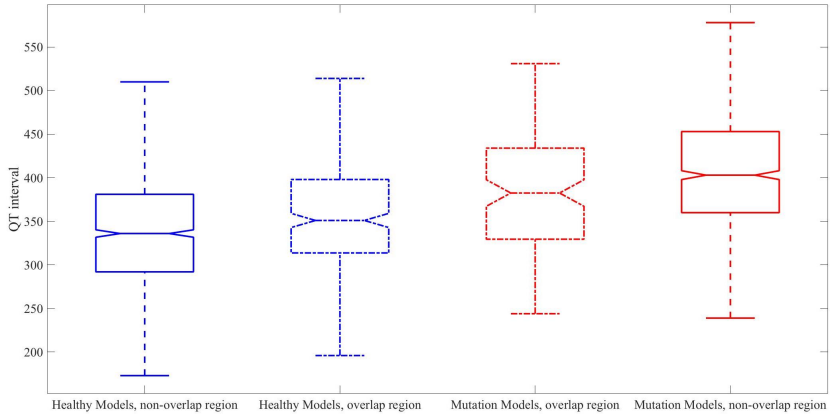

Figure 4.19: Box plots of the QT interval values for the healthy (in blue) and mutation-carrier (in red) models in the non-overlap (first and last columns) and overlap (central columns) regions.

show significant differences in the two populations in terms of correlations. From the PCC results reported in Figure 4.20, we can clearly see that the G_{NaL} and G_{Na} are those showing the biggest differences between the two populations for the QT prolongation. For the G_{NaL}, that is a direct consequence of the remodelling due to the mutation. This is a confirmation that this current plays the key role in prolonging the QT interval. For the G_{Na}, the stronger the G_{Na}, the narrower the QRS and therefore the QT. Coherently, from the PCC results, we can see

Figure 4.20: PCC results for the healthy (first 5 columns) and mutation-carrier (last 5 columns) fibre populations.

that the G_{Na} correlates negatively with the QT interval. We can also observe that it plays a bigger role in the mutation-carriers. Therefore, when the G_{Na} is halved due to the mutation, it fails its role in shortening the QT. In other words, both the G_{Na} and G_{NaL} have a bigger role in the mutation-carrier population. Weak G_{Na} results in a wide QRS and therefore a longer QT, therefore, both halved G_{Na} and doubled G_{NaL} contribute to the prolongation of QT interval under the mutation. Importantly, from the PCC analysis, we could also see that the correlation coefficients between P_{Ca} and QT interval is slightly decreased under the mutation, which means that the contribution of calcium current in APD is less significant due to the change of membrane voltage caused by the mutation, and the PCC analysis from the single cell level also showed a consistent trend. Therefore, blocking calcium current may not be effective enough for the purpose of QT shortening under this mutation. At the same time, calcium current block may impair the safety of tissue conduction as shown in Figure 4.17.

4.2.3 Possible diagnosis biomarkers

When *QT* and *QRS* are not prolonged, the *TDR* biomarker can detect the mutation-carrier models

Among the tissue biomarkers, the TDR is the one that can be more useful in discriminating between healthy subjects and mutation-carrier patients. In fact, the TDR shown by the mutation-carrier models in the region where both QT and QRS are normal (overlap region) is significantly bigger compared to the healthy subjects in the same region and also compared to the other mutation-carrier models (Figure 4.21). The dispersion in the repolarisation is mainly due to the transmural effects of the disease, which are stronger in the endocardial layer. In general, the effect of the mutation at the cellular level produce a prolongation in $APDs$ of all cells. Interestingly, in the overlap region, endocardial cells exhibit a more pronounced APD prolongation than the epicardial layer (Figure 4.22). Indeed, in this region, the more significant APD prolongation in endocardial cells results in an $APDs$ dispersion between the two layers. The T wave shape is inevitably affected by

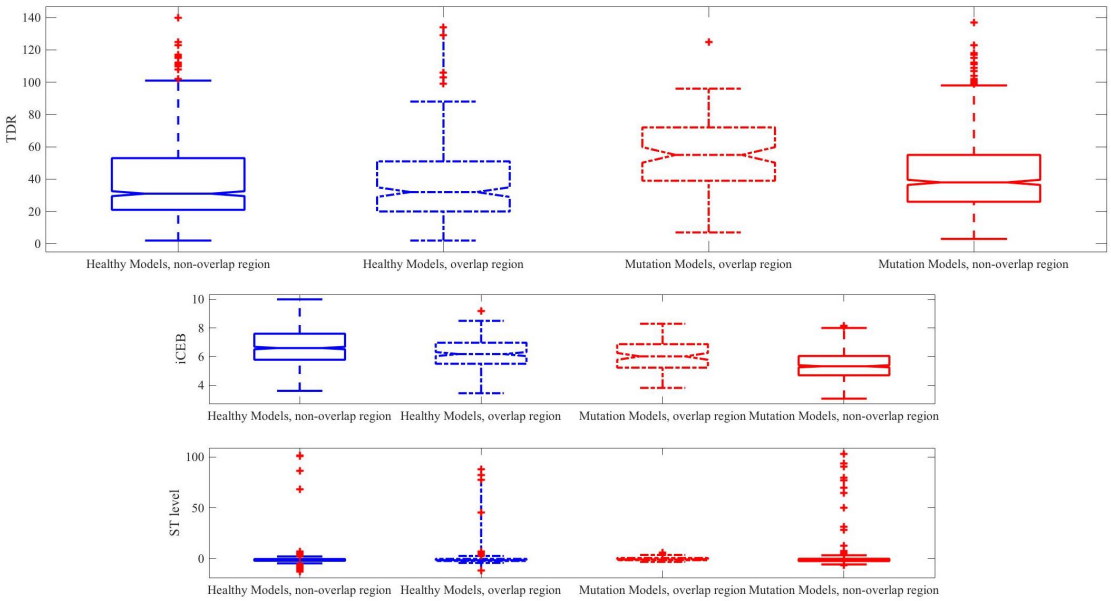

Figure 4.21: Box plots of the *TDR* values for the healthy (in blue) and mutation-carrier (in red) models in the non-overlap (first and last columns) and overlap (central columns) regions. The bottom two panels show the box plots of the *iCEB* and *STlevel* values to highlight the role of the *TDR* biomarker to detect the mutation-carrier models in the overlap region.

that, and as a consequence it is reflected in the tissue biomarker TDR (which accounts for the interval between the earliest and the latest AP repolarisation times). The more significant APD prolongation caused by the mutation on the endocardial layer is due to the transmural difference between the two layers. All potassium currents are stronger in the epicardial cell baseline model, as shown in Table 2.1. Moreover, the baseline model of an endocardial cell has a bigger late sodium current. Therefore, when the mutation is introduced and the late sodium current is doubled the repolarisation currents in the endocardium are much weaker to counteract the APD prolongation due to the late sodium current. On the other hand, in the epicardial layer the repolarisation currents are quite strong and these cells need a very big late sodium current to produce $APDs$ prolongation. In fact, as shown in Figure 4.23 the late sodium current is still not strong enough to produce a prolongation in the $APDs$ for those mutation-carrier models in the overlap region. However, it is bigger in the other mutation-carrier models that in fact show a prolongation (still inferior to that in the endocardium).

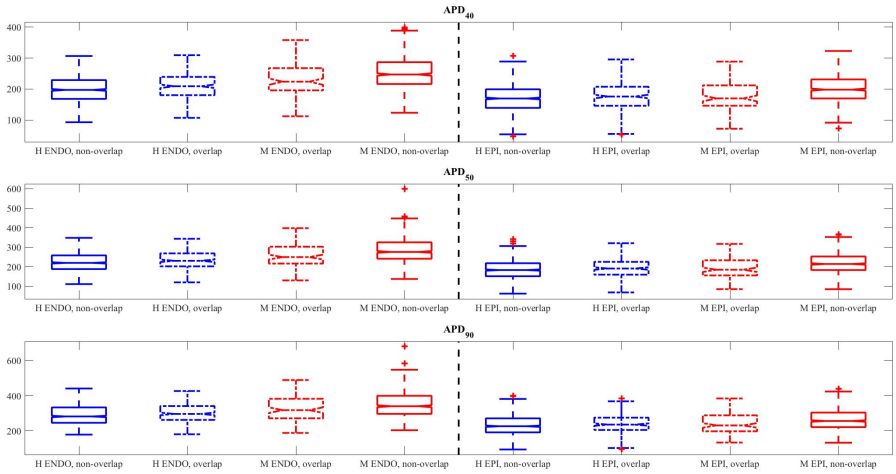

Figure 4.22: Box plots of the *APDs* values for the healthy (in blue) and mutation-carrier (in red) endocardial and epicardial (left and right panel respectively, separated by the vertical dotted line) cell models in the non-overlap (first and last columns of each panel) and overlap (central columns of each panel) regions.

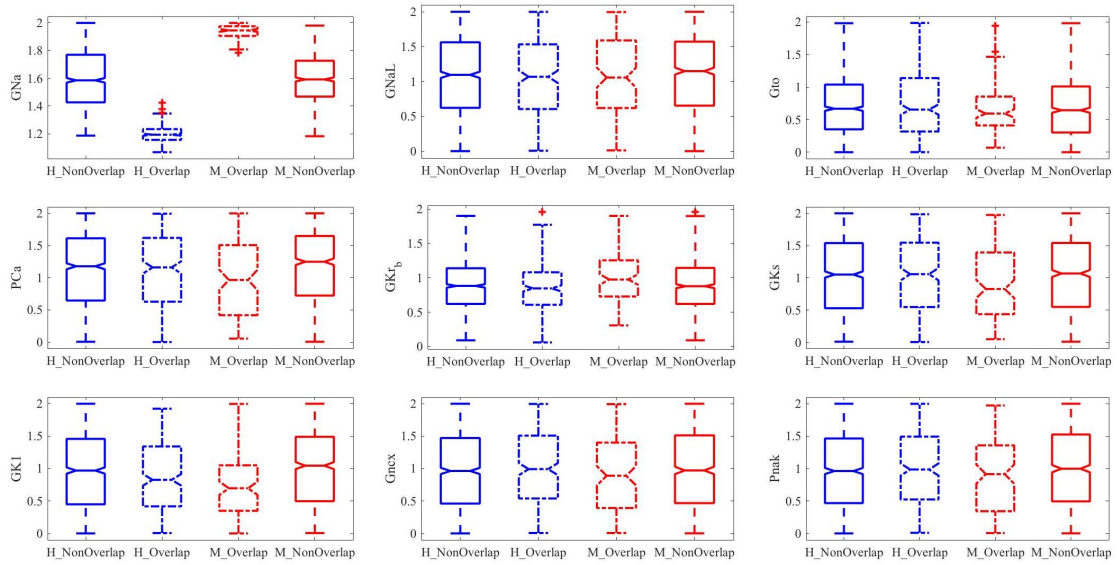

Figure 4.23: Box plots of the scaling factors of the ionic properties for the healthy (in blue) and mutation-carrier (in red) models in the non-overlap (first and last columns) and overlap (central columns) regions. The effect of the mutation on the sodium current is not shown in the picture.

4.2.4 Bradycardia-related QT-interval prolongation

Family members are frequently treated with pacemakers to prevent (mostly nocturnal) bradycardia, associated with excessive QT prolongation. We modelled this factor by performing a simulation study with a bigger cycle length at 1500 ms. Single cell results show longer APs induced by the longer cycle length, in spite of similar magnitudes of the late sodium current compared with the shorter cycle length (Figure 4.24). As a consequence, we ascribe the AP prolongation to the restitution properties of the other currents. Tissue results show increased QT

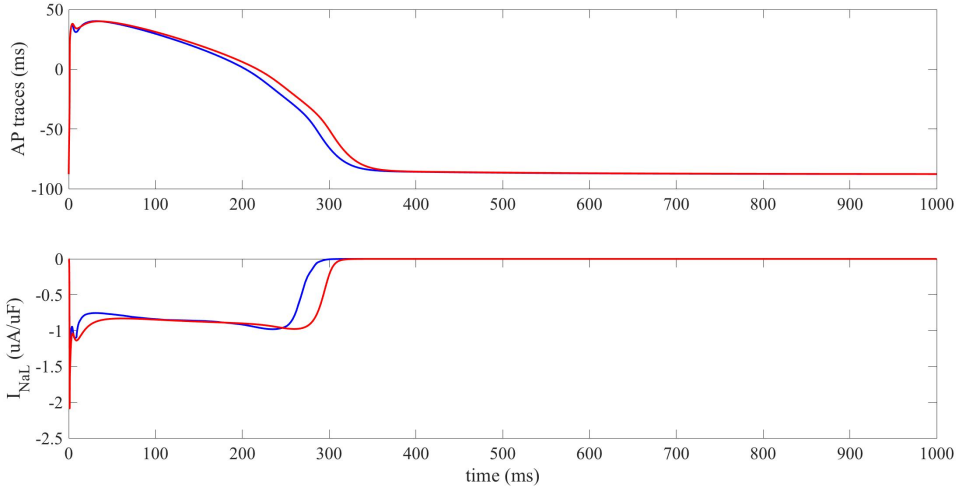

Figure 4.24: Effects of bradycardia on the AP (first panel) and late sodium current (second panel) traces. Red traces: cycle length of 1500 ms. Blue traces: cycle length of 1000 ms.

prolongation, in agreement with the clinical findings but no significant effects on the QRS width, compared with the smaller cycle length (Figure 4.25). The results obtained here are therefore in accordance with those at a slower cycle length. In fact, we could observe that a strong fast sodium current is necessary to maintain a good conduction and the stronger this current the narrower the QRS. The late sodium current is the most relevant current in determining the QT interval prolongation. Finally, the difference in the $APDs$ prolongation between the endocardium and epicardium layers is, even in this scenario, the key point for the bigger TDR in the mutation-carrier models in the overlap region. We also analysed how the $PCCs$

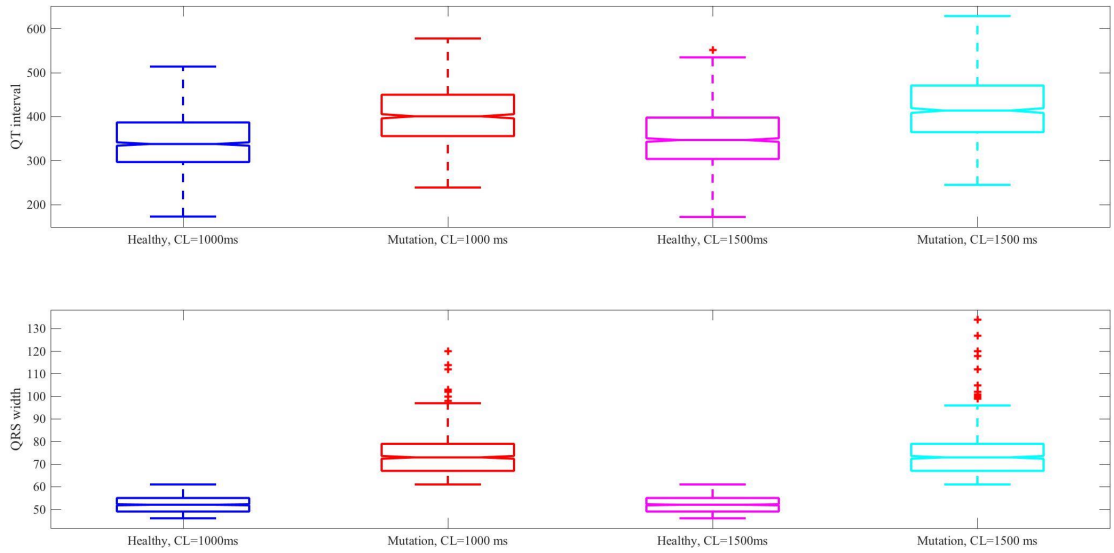

Figure 4.25: Box plots of QT interval (first panel) and QRS width (second panel) values in both population (healthy in blue and magenta; mutation-carriers in red and cyan) when bradycardia is considered (last two columns).

between the model parameters and the QT interval vary when the cycle length is increased. The PCC results for both cycle lengths are reported in Figure 4.26. PCC results are qualitatively similar between the two cycle lengths, we can therefore claim that the PCC analysis results are not rate dependent.

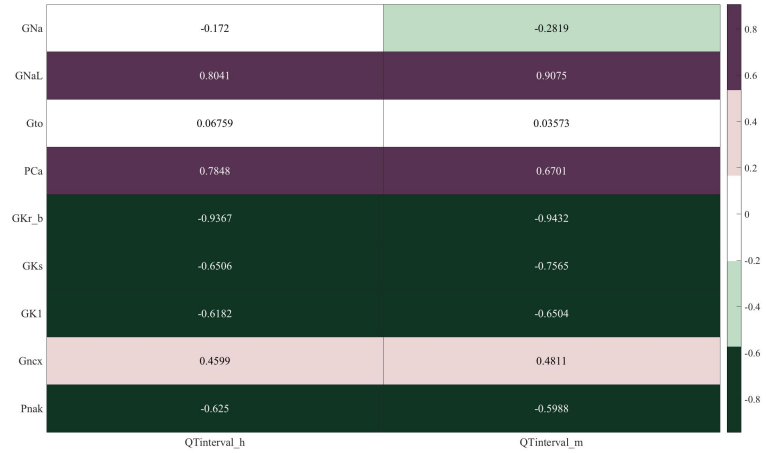

(a)

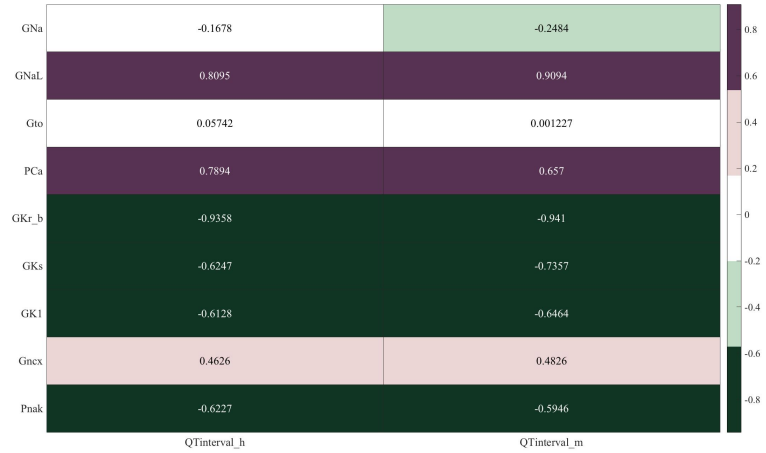

(b)

Figure 4.26: *PCC* results for different cycle length. 1000 *ms* cycle length in the first panel and 1500 *ms* cycle length in the second one. In each panel the first column represents the healthy condition and the second column the mutation-carriers.

5 Discussion

Contents

5.1 Achievements

This dissertation focused on one of the cardiac sodium channel overlap syndromes. Those syndromes are a broad spectrum of *SCN5A*-related arrhythmia syndromes. The *SCN5A* is one of the genes encoding the cardiac sodium channel alpha subunits, through which the influx of sodium ions generates the cardiac sodium current. Genetic studies have shown that mutations in the *SCN5A* gene are associated with various arrhythmia syndromes (e.g. *BrS*, *LQT* syndrome, conduction disease and cardiomyopathy) by modulating gating and other functional properties of that channel. In particular, the mutation under investigation in this work was the *SCN5A-1795insD*. Described for the first time in 1999 by Bezzina and colleagues, the main functional consequences of this mutation are a sustained sodium current throughout the *AP* plateau that prolongs cardiac repolarisation and a drastic reduction in peak sodium current density that affects the conduction velocity. Patients suffering from

this mutation show several abnormalities in their *ECG* recordings, in particular those similar to patients suffering from *LQT3* and *BrS*. During the past decades, the understanding of these sodium channelopathies has increased strongly. However, there is still a lack of knowledge regarding the biophysical properties of the mutant sodium channels and how these properties reflect themselves in patients' clinical symptoms. Up to date there are still questions left to be resolved regarding the phenotypic variability observed in the patients carrying the mutation. The family affected by the *SCN5A-1795insD* is one of the largest and best-described family worldwide. Researchers made a hug effort in characterising the biophysical properties of this mutation through the use of heterologous expression systems, developing a transgenic model of the murine equivalent mutation *1798insD* and also *hiPSC*-derived cardiomyocytes have been considered.

Our aim was to derive further insights based on mathematical modelling and computer simulations into this type of high risk life-threatening disease. Since the family that we wanted to investigate is characterized by a huge variability in terms of disease expression and severity, we chose a methodology capable to reproduce and explore such characteristics: the populations of models methodology. In addition, we needed of an approach that allowed us to progress the investigation from the single cell to the tissue level, in order to generate simulated data that could be compared to the clinical one (i.e. biomarkers extracted from *ECG* recordings). Hence our choice was to exploit a multi-scale approach in order to study the mutation effects on both single cell and fibre populations. Our simulation studies demonstrated that the designed approach was capable of recapitulating the phenotypic manifestation of the disease at both single cell and tissue scales. Building on these results, we provided mechanistic explanations on the ionic and cellular mechanisms underlying such a variability, including those mechanisms that reflect themselves on the *ECG* and could therefore become novel clinical biomarkers for the diagnosis of potential mutation carriers. Additionally, we gained further insights on possible therapeutic targets and we supplied evidence to support the depolarisation hypothesis in *BrS*. According to our results, we could confirm the role of heart rate in prolonging the

QT interval in *1795insD* mutation carriers, with implications in the increased rate of nocturnal sudden cardiac death in this group of patients.

Given the simulated results, we defined an overlap region as the region in which our mutation-carrier fibre models exhibited a QRS value in the range of maximum QRS values in the control population. We considered the models within and outside the above defined regions, and studied the combination of their tissue-, cellular- and ionic-level properties to explain the manifestations of the disease.

When we introduced in the healthy population the ionic remodelling associated with the mutation, we could highlight the key role of the sodium current in sustaining a proper conduction in the fibre, and the role of the transient outward potassium current in modulating the conduction velocity. The latter is an important novel result of the present thesis, demonstrating transient outward potassium current modulation of conduction velocity in *BrS*-related syndromes (depolarisation hypothesis) in the absence of significant changes in the notch of epicardial APs (repolarisation hypothesis). In the models that experienced conduction failure, the inward currents (sodium and calcium mainly) were always very weak and could not sustain a proper upstroke. In addition, the transient outward potassium current was very strong, affecting therefore the conduction velocity by further opposing the fast sodium current and modulating the L-type calcium current activation. On the other hand, the fibre models with a proper conduction behavior were always characterized by a strong fast sodium current. This constitutes the main biophysical mechanism underlying the variable manifestation of the disease in this group of patients affected by the same channel mutation.

From the PPC analysis between the model parameters and the tissue biomarkers we showed that the G_{NaL} and G_{Na} were the main responsible to prolong the QT interval. The doubled G_{NaL} played the largest role in prolonging the QT interval. The halved G_{Na} also contributed through prolonging the QRS. From the PCC results we also identified that the role of the P_{Ca} in sustaining the QT is significantly reduced in mutation carriers. This is due to the fact that the mutation further affects the overall calcium current, throughout a reduced peak and plateau membrane

voltage impairing L-type calcium current activation. From these results, it emerges that calcium blockers might be less effective for *1795insD* mutation-carriers than in other channelopathies as a pharmacological therapy against QT prolongation.

Combining the simulation results at the single cell and tissue levels we additionally gained further insights on the transmural effects of the mutation. We showed that this mutation produced an APD dispersion between the endocardial and epicardial layer, which is manifested in tissue through a more pronounced transmural dispersion of repolarisation (TDR). We identified the ionic mechanisms of such an increased dispersion in the site-dependent variation of the repolarisation currents. We indeed suggested studying TDR in clinical settings through ECG-related *Tpeak-Tend* interval biomarkers, since these could provide incremental information for risk stratification in these complex patients. Our results are furthermore in accordance with the recently published systematic review and meta-analysis by Tse et al. [57], in which the prognostic significance of the *Tpeak-Tend* interval with respect to arrhythmic and mortality outcomes was investigated. The pooled meta-analysis demonstrated that a prolonged *Tpeak-Tend* interval is associated with 1.14 times higher risk of ventricular tachycardia/ventricular fibrillation or sudden cardiac death and with a 5.6-fold increase in *BrS*. A prolonged *Tpeak-Tend* interval will increase the likelihood of generating unidirectional conduction block, but other factors such as slowed conduction and increased dispersion of conduction should also be considered since not reflected in the *Tpeak-Tend* interval [57]. Moreover, regarding this aspect, Osadchii and colleagues [37] published an interesting work on spatial heterogeneities in the electrical restitution in perfused guinea-pig heart. They showed that amplified regional restitution heterogeneities can determine arrhythmic vulnerability and that *JTpeak* vs. *JTend* difference in the restitution slope can approximate the regional non-uniformities in APD restitution. Importantly, in assessments of arrhythmic susceptibility, the *JTpeak* vs. *JTend* restitution would not simply duplicate some other known ECG metrics of repolarisation, such as the *Tpeak-to-Tend* interval, allowing to study changes in action potential duration over a wide range of cardiac beating rates. Minchole and colleagues [30] also proposed a

method to non-invasively quantify dispersion of APD restitution ($APDR$) slopes at tissue level by making only use of the surface ECG. They estimated the rate normalized differences in the steady-state T-wave peak to T-wave end interval and assessed its capability to reflect $APDR$ dispersion using a combination of ECG signal processing, and computational modeling and simulation. According to their results, they could well estimate non-invasively $APDR$ dispersion in ventricle.

From our simulations performed at longer cycle lengths (mimicking lower heart rates), we could confirm the increased QT prolongation observed in patients where the heart rate is lower. We observed longer APs induced by the longer cycle length, in spite of similar magnitudes of the late sodium current compared with the shorter cycle length. As a consequence, we ascribed the AP prolongation to the restitution properties of the other currents and we also concluded that late sodium current blocker might be less effective in the scenario of a slower heart rate.

From our results, the transient outward potassium current was mainly involved in modulating the conduction velocity and not the AP shape as stated in the repolarisation hypothesis of BrS. In fact, we could not observe any cellular AP shapes in agreement with that hypothesis, in spite of considering regional conditions of increased transient outward potassium current in the right ventricle. The repolarisation hypothesis claims that the so-called BrS phenotype is due to an outward shift in the balance of currents in the right ventricle epicardium (reduced inward sodium current in the presence of a prominent transient outward potassium current), which can result in repolarisation abnormalities due to the accentuated AP notch in the epicardium versus the endocardium. In our simulations, the combination of a weak G_{Na} and a strong G_{to} led to a reduced membrane voltage that affected the overall shape of the other currents through affecting the membrane voltage. We should in fact be careful and not reduce the entire activity of a channel to its maximum conductance but considering also the kinetics (voltage-dependent gating variables) and their driving forces. Regarding the role of the transient outward potassium current, it might be therefore useful to consider drug blockers to ameliorate one of the main consequences of the mutation, which is conduction

failure and more in general conduction abnormalities. However, transient outward potassium current blockers currently available in the marker (such as Quinidine) are also known to block rapid delayed rectifier potassium current, therefore also prolonging the QT interval. Quinidine has been reported to have electrophysiologic efficacy in patients with idiopathic ventricular fibrillation and *BrS* (see the extensive work done by Bernard Belhassen). However, Quinidine might not have the same positive effect on *SCN5A-1795insD* mutation-carriers, as these are characterized by a combination of *BrS* and *LQT3* symptoms. Interestingly, Hai and colleagues [20], reported the management of a difficult case of *BrS* with recurrent ventricular tachyarrhythmia that did not respond Quinidine therapy. In fact, the patient was also affected by two mutations resulting in a destabilized inactivation of the sodium current, a reduction in the peak sodium current and a persistent inward sodium current. In that case the combined therapy of Mexiletine and radiofrequency ablation successfully prevented recurrent ventricular tachyarrhythmias. Mexiletine blocks the late sodium current and has been shown to effectively shorten the QTc interval and reduce life-threating ventricular tachyarrhythmia in patients with gain-of-function mutations in the *SCN5A*. The ablation was performed in the $RVOT$ and right ventricle *Purkinje* network. Regarding late sodium current blockers, Portero and colleagues [42], also reported that the late sodium current inhibitor *GS967* decreased repolarisation abnormalities and had anti-arrhythmic effects in the absence of deleterious effects on cardiac conduction.

We also found that the main electrophysiological manifestations of the mutation were reflected on the endocardial layer. Such a layer, which is indeed characterized by a physiological stronger late sodium current and weaker repolarisation currents, was more prone to develop APD prolongation than the epicardial one. Therefore, an increased dispersion of repolarisation could develop under *SCN5A-1795insD* conditions, which can be captured at the tissue level analyzing the TDR biomarker. These results further oppose the repolarisation hypothesis, according to which the epicardial layer should exhibit the largest APD changes due to its stronger transient outward potassium current. We therefore showed two different mechanisms that

were not supported by the repolarisation hypothesis. The other proposed hypothesis for *BrS* is the depolarisation one, according to which the slow conduction in the *RVOT* has a primary role in the development of the electrocardiographic and arrhythmic manifestations of *BrS*. Ventricular arrhythmia associated to *BrS* are induced by the abnormal current created by delayed depolarisation of the *RVOT*. The delayed depolarisation of the *RVOT* with respect to the other right ventricular *APs* creates a potential difference between the right ventricle and the *RVOT*, manifested in the leads *V1* to *V3* of the clinical *ECG*. *RVOT* has for its nature less conductive reserve, so when the sodium is decreased, the conduction delays mainly occur in that region. It has been reported that radio-frequency ablation of epicardial site displaying late potentials in the *RVOT* of patients with *BrS* significantly reduced arrhythmia vulnerability.

In terms of therapeutic targets, considering all these findings, we could support the use of late sodium current blockers to shorten the *QT* interval and to reduce the *TDR*, as well as the use of transient outward potassium current blockers to improve the conduction velocity. On the other hand, our understanding about L-type calcium current blockers suggests that their use might be less effective in these patients.

5.2 Limitations

The main aim of this investigation was to reproduce and explain the phenotypic manifestation of the disease under investigation. To do so, we built populations of cells and fibres in the healthy and mutation-carrier conditions to generate simulated data to be compared with the clinical one. Our simulated *ECGs* were *pseudoECG* traces of a 1D 2 *cm* fibre of the right ventricle. This is the main limitation of this study. We focused our efforts in modelling and studying a transmural fibre of the *RVOT* that is known to be the most affected part of the heart (Figure 5.1). Therefore, in our *pseudoECGs* the effects of the mutation appeared more significant compared to real *ECGs* that account for the contribution of the whole heart. Adding the contribution of the less affected part of the heart would have resulted in simulated *ECG* traces more consistent with the real ones.

Figure 5.1: The transmural fibre of the RVOT modelled in this study.

5.3 Future work

Based on the results obtained in this investigation, we would further analyze the *JTpeak-JTend* and *Tp-Te* restitutions as integrative metrics in assessments of repolarisation dynamics, which seemed to play an important role in these patients with variable phenotypes and might help clinicians in gaining additional information when the most common biomarkers (i.e. QT and QRS) are not informative. Another interesting point is the possible role of hypertrophy. Genetic modifiers also likely play a role in mutation-carrier patients as well as environmental factors, including co-morbidity. In recent years, pacemaker treatment proved successful in the clinical management of sudden cardiac death in this group of patients, but more recently there have been a number of mutation carriers who died or had ventricular tachycardia/ventricular fibrillation despite the pacemaker. These patients were mostly older, i.e. aged >45 years, and the majority of them had hypertension and/or hypertrophy. Moreover, it has been observed from the transgenic models carrying the murine equivalent mutation that the co-existence of hypertrophy exacerbates the pro-arrhythmic phenotype. We therefore suggest considering hypertrophy into our modelling framework as an extension of our work.

Appendices

A

Supplementary material

Contents

A.1 Extended results for the overlap study in single cell

We studied the space distribution of the AP biomarkers and the ionic properties of the models belonging to the different regions, i.e. showing different biomarker values. We did this for each pair of biomarkers for the endocardial and epicardial populations. We report here all the extended results of this analysis to confirm that the overlap observed and studied in tissue is also present in single cell, further highlighting the huge variability that characterises this family.

For the endocardial cells the best biomarkers in order to perform the classification are those related to the peak voltage ($VmPeak$, $VmTime$ and TTP) but also all the $APDs$ (Figure A.1, Figure A.2, Figure A.3, Figure A.4). For each of these biomarkers we can clearly see that the mutation-carrier models can be divided in

two subgroups, one that overlaps the healthy models and one that shows abnormal values of the biomarker considered. The thresholds used to separate the mutation-carrier models in the two groups are 32 mV and 8 ms for the $VmPeak$ and $VmTime$, respectively. For the $VmPeak$ there are 1154 and 187 models in the overlap ($VmPeak$>32 mV) and non-overlap zone ($VmPeak$<32 mV); for the $VmTime$ 916 in the overlap region ($VmTime$<8ms) and 425 in the non-overlap ($VmTime$>8ms). The ionic properties of the models within these two regions are shown in Figure A.5 for the $VmPeak$ and Figure A.6 for the $VmTime$. For the TTP we set a threshold at 11 ms and we found 248 models in the overlap region (TTP<11ms) and 1093 in the non-overlap region (TTP>11ms). Indeed, most of the endocardial model show a very big TTP. The ionic properties of these models are reported in Figure A.7. As regard the biomarkers related to the AP duration, the $APDs$, we show here the APD_{90}. We set a threshold at 450 ms and we obtained 1201 models in the overlap region (APD_{90}<450 ms) and 140 in the non overlap region (APD_{90}>450 ms). The ionic properties are in Figure A.8.

For the epicardial cells the most suitable biomarkers for this analysis are the $VmPeak$, $VmTime$ and TTP. That highlights the first main outcome: the main effect of the mutation in terms of AP prolongation occurs in the endocardial layer and not in the epicardial one. This is a really interesting point since the difference in the two layers may lead to a dispersion in the myocardium that can be revealed in tissue. In Figure A.9 , Figure A.10 and Figure A.11 we report the distribution of these three epicardial biomarkers against all the other. We set the following thresholds: 25 mV for the $VmPeak$, 7 ms for the $VmTime$ and 7 ms for the TTP. The overlap regions are consisting of 1168, 1272 and 717 for the $VmPeak$, $VmTime$ and TTP respectively. In the non-overlap regions there are 173, 69 and 624 models. In Figure A.12, Figure A.13 and Figure A.14 we report the ionic properties of the models belonging to the various regions of the space.

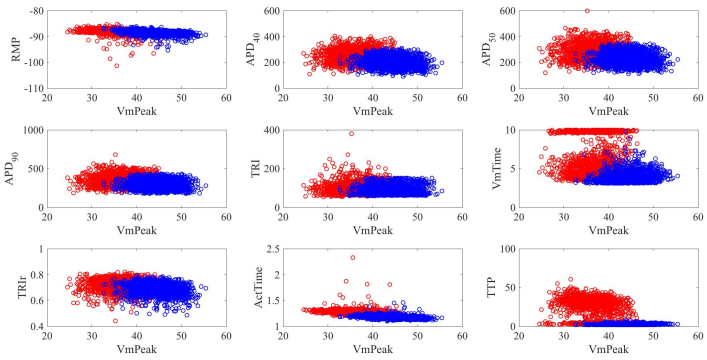

Figure A.1: Scatter plots for the values of the $VmPeak$ biomarker against all the other biomarkers in the two conditions (healthy in blue and mutation-carrier in red). Endocardial cells.

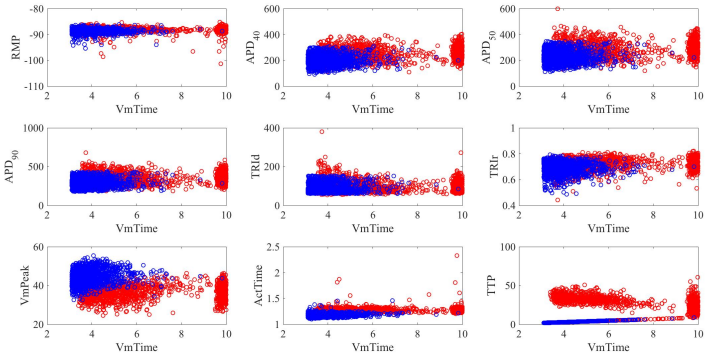

Figure A.2: Scatter plots for the values of the $VmTime$ biomarker against all the other biomarkers in the two conditions (healthy in blue and mutation-carrier in red). Endocardial cells.

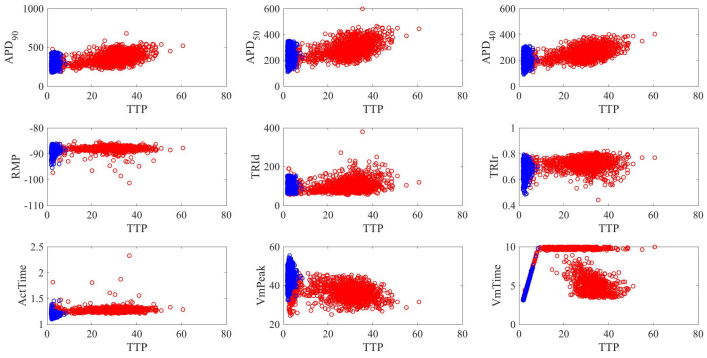

Figure A.3: Scatter plots for the values of the TTP biomarker against all the other biomarkers in the two conditions (healthy in blue and mutation-carrier in red). Endocardial cells.

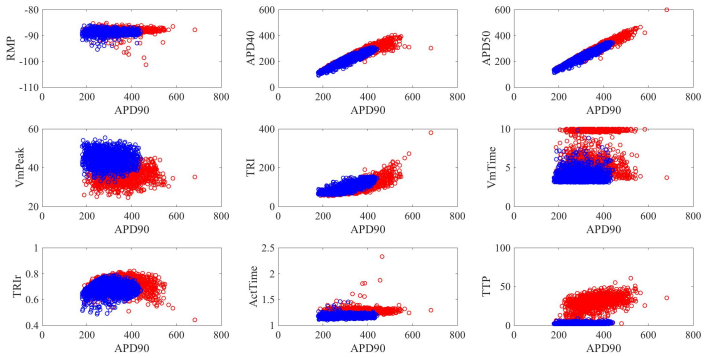

Figure A.4: Scatter plots for the values of the APD_{90} biomarker against all the other biomarkers in the two conditions (healthy in blue and mutation-carrier in red). Endocardial cells.

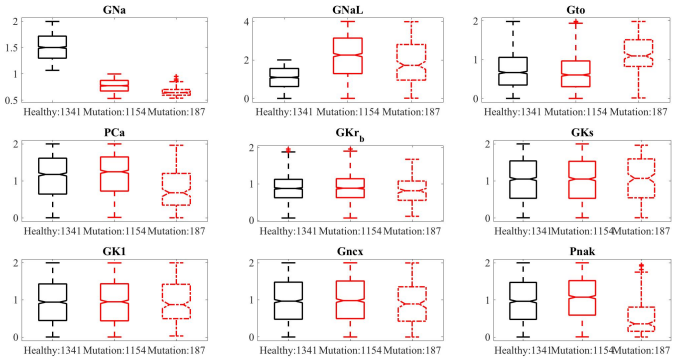

Figure A.5: Box plots for the ionic properties of the mutation-carrier models that do (red solid line) and do not (red dotted line) overlap the healthy ones (black line) in $VmPeak$. The effect of the mutation on the sodium conductances is shown in the figure. Endocardial cells.

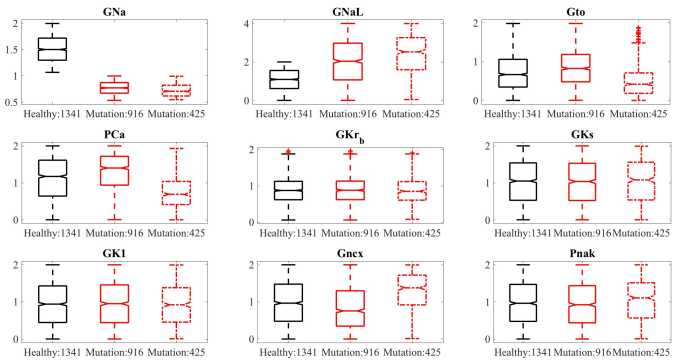

Figure A.6: Box plots for the ionic properties of the mutation-carrier models that do (red solid line) and do not (red dotted line) overlap the healthy ones (black line) in $VmTime$. The effect of the mutation on the sodium conductances is shown in the figure. Endocardial cells.

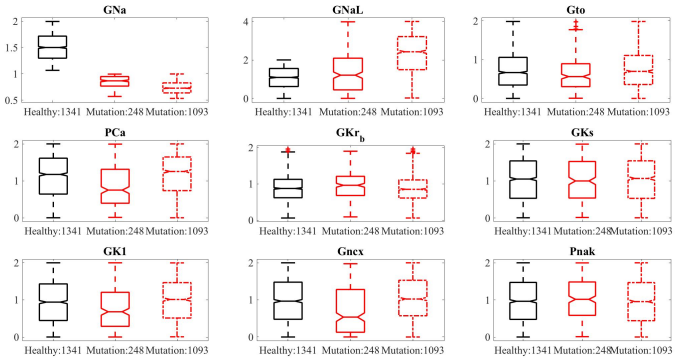

Figure A.7: Box plots for the ionic properties of the mutation-carrier models that do (red solid line) and do not (red dotted line) overlap the healthy ones (black line) in TTP. The effect of the mutation on the sodium conductances is shown in the figure. Endocardial cells.

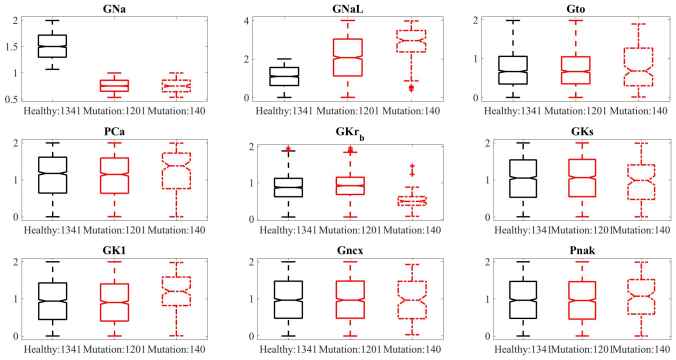

Figure A.8: Box plots for the ionic properties of the mutation-carrier models that do (red solid line) and do not (red dotted line) overlap the healthy ones (black line) in APD_{90}. The effect of the mutation on the sodium conductances is shown in the figure. Endocardial cells.

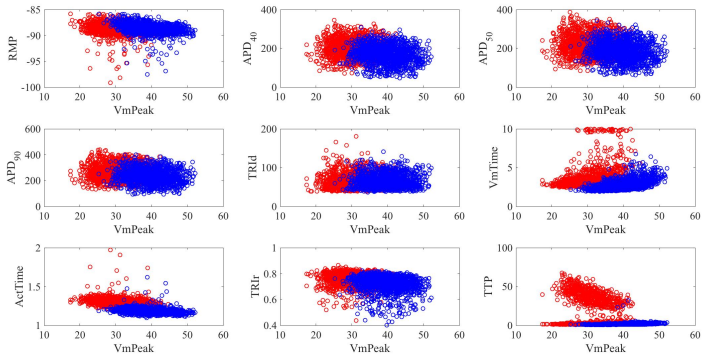

Figure A.9: Scatter plots for the values of the $VmPeak$ biomarker against all the other biomarkers in the two conditions (healthy in blue and mutation-carrier in red). Epicardial cells.

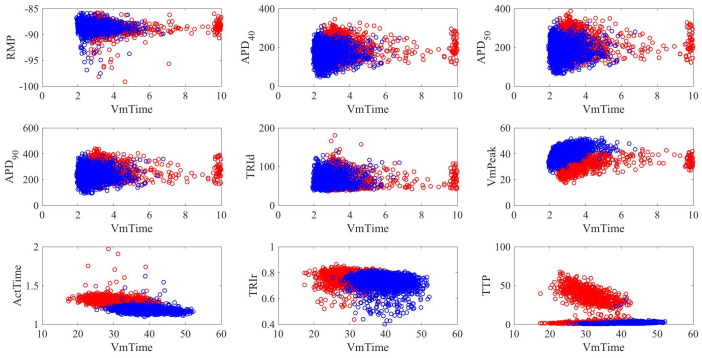

Figure A.10: Scatter plots for the values of the $VmTime$ biomarker against all the other biomarkers in the two conditions (healthy in blue and mutation-carrier in red). Epicardial cells.

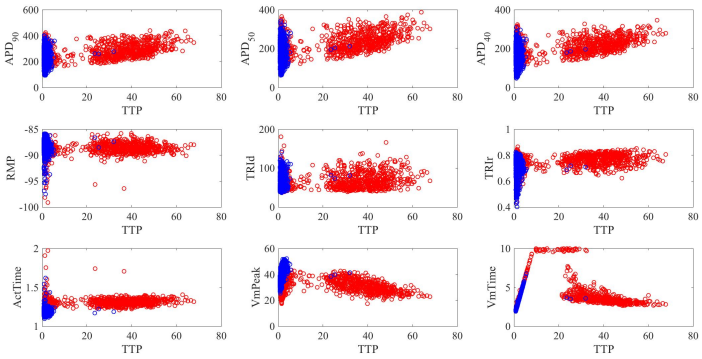

Figure A.11: Scatter plots for the values of the TTP biomarker against all the other biomarkers in the two conditions (healthy in blue and mutation-carrier in red). Epicardial cells.

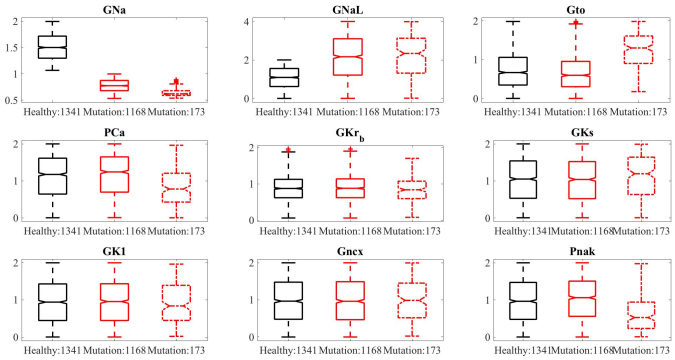

Figure A.12: Box plots for the ionic properties of the mutation-carrier models that do (red solid line) and do not (red dotted line) overlap the healthy ones (black line) in $VmPeak$. The effect of the mutation on the sodium conductances is shown in the figure. Epicardial cells.

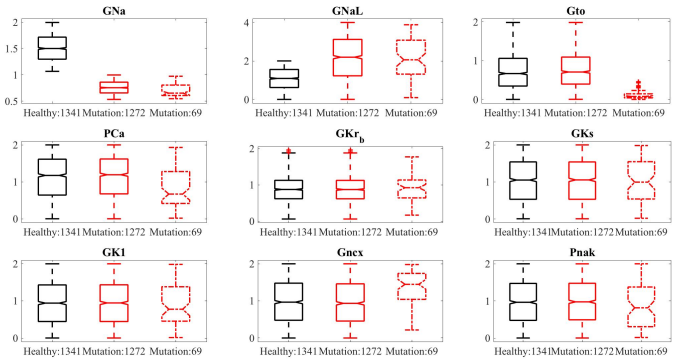

Figure A.13: Box plots for the ionic properties of the mutation-carrier models that do (red solid line) and do not (red dotted line) overlap the healthy ones (black line) in $VmTime$. The effect of the mutation on the sodium conductances is shown in the figure. Epicardial cells.

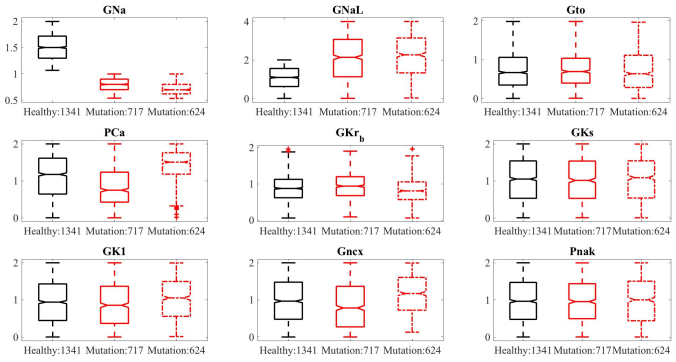

Figure A.14: Box plots for the ionic properties of the mutation-carrier models that do (red solid line) and do not (red dotted line) overlap the healthy ones (black line) in TTP. The effect of the mutation on the sodium conductances is shown in the figure. Epicardial cells.

A.2 Extended results for the bradycardia study

Family members are frequently treated with pacemakers to prevent (mostly nocturnal) bradycardia with associated excessive QT prolongation. In this investigation, the relationship between the effects of the mutation and the heart rate is taken into account considering a longer cycle length, 1500 ms, in the simulations. As previously mentioned, the results achieved in this scenario are in agreement with those obtained with a smaller cycle length and moreover with the clinical evidences according to which a slower heart rate is a risk factor for these patients. We report here all the results from these simulations.

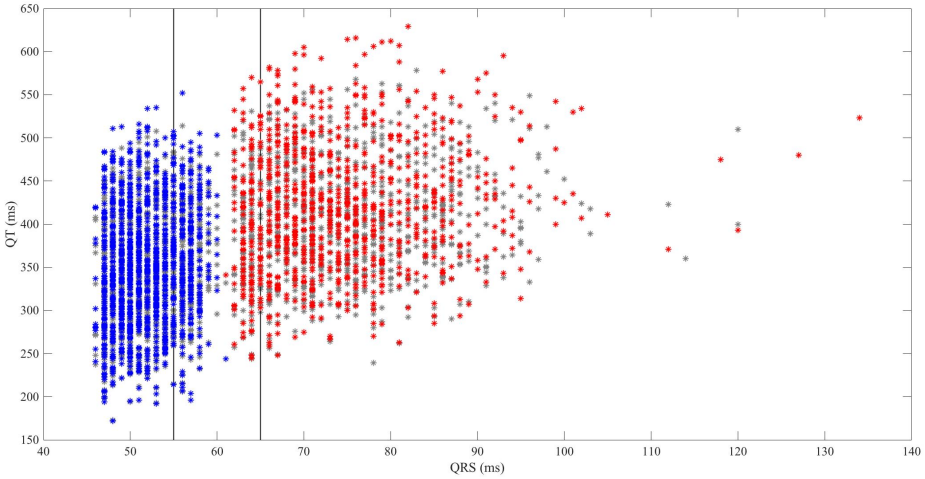

Figure A.15: QT and QRS values obtained with a longer cycle length. In grey the QT and QRS values for a 1000 ms cycle length and in blue (healthy) and red (mutation-carrier) the corresponding values with a 1500 ms cycle length.

In Figure A.15 we can observe how the distributions of the QT interval and QRS width values are affected by the mutation. The overall distribution of the points is the same compared to the smaller cycle length and we can still notice the presence of a region in which models of both conditions overlap. However, in agreement with clinical data, the QT interval is now more prolonged while the QRS width is mostly the same (Figure A.16). Performing the same classification done for the 1000 ms cycle length, we obtained an overlap region in terms of QRS

values made up of 264 healthy models and 117 mutation-carriers models, whose ionic properties are reported in Figure A.17.

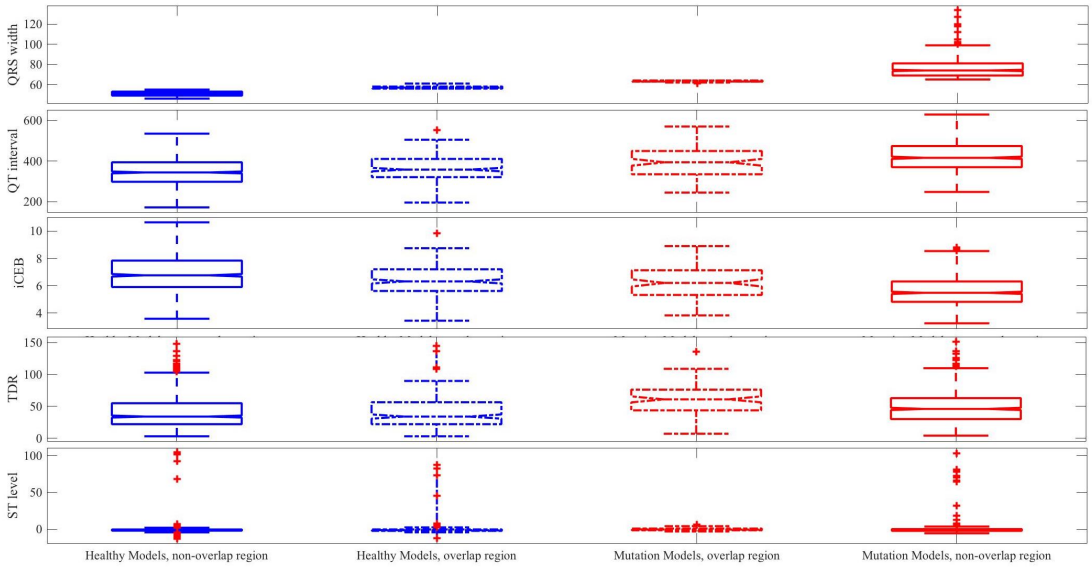

Figure A.16: Box plots of tissue biomarker values in the non-overlap (first and last columns) and overlap (central columns) regions. 1500 ms cycle length.

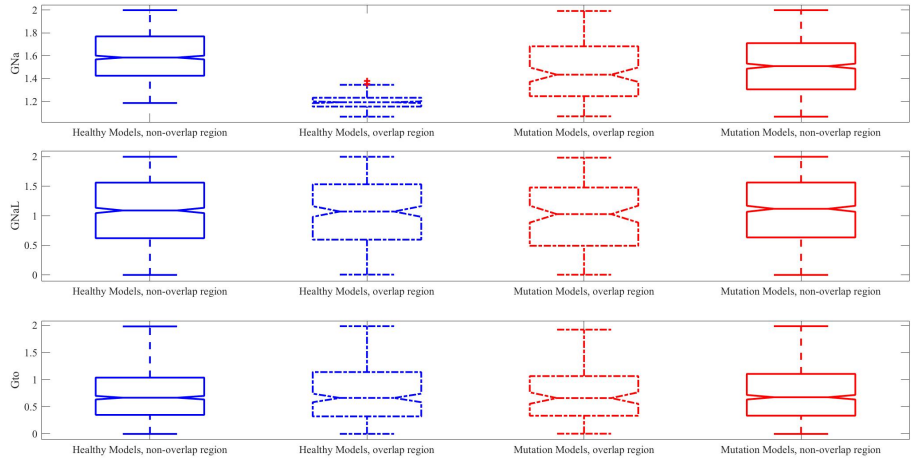

(a)

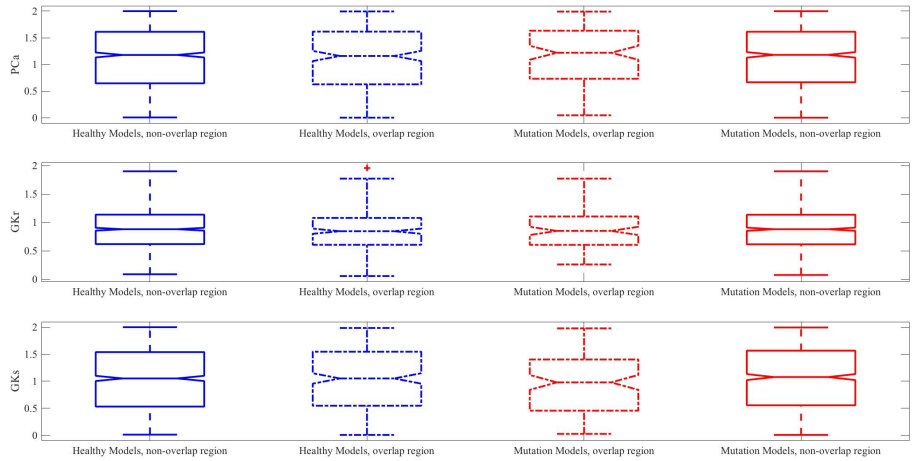

(b)

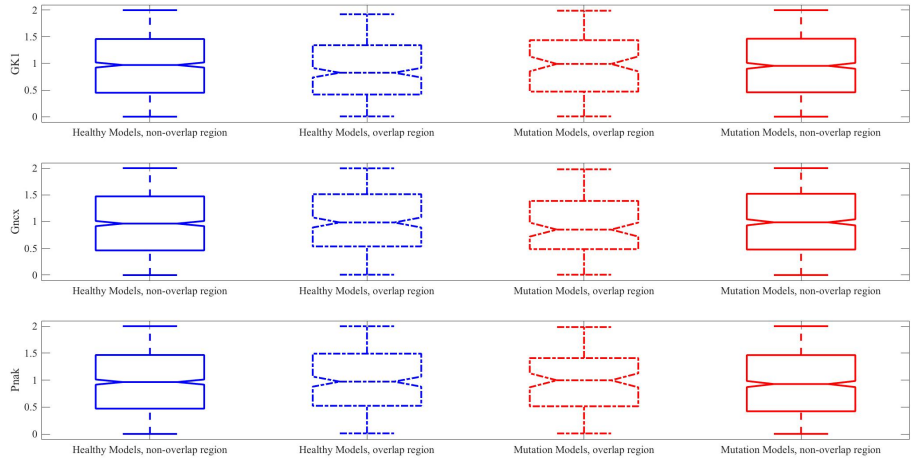

(c)

Figure A.17: Box plots of the scaling factors for I_{Na}, I_{NaL} and I_{to} in (a), I_{CaL}, I_{Kr} and I_{Ks} in (b) and I_{K1}, I_{ncx} and I_{NaK} in (c), in the non-overlap (first and last columns) and overlap (central columns) regions. 1500 ms cycle length.

A.3 The transmural dispersion of repolarisation study

The transmural dispersion of repolarisation (TDR) is defined as the interval between the earliest and latest AP repolarisation times and can be approximated by the interval between the peak and the end of the T wave [18]. We analysed this particular aspect comparing the *pseudoECG* trace and the AP propagation through the fibre nodes. We also investigated how the TDR varies with the T wave morphology, in particular taking into account what happens when this wave is positive, negative or biphasic. The T wave of the *pseudoECG* is the tissue level phenomenon that reflects the differences in the repolarisation phase across the myocardium. Figure

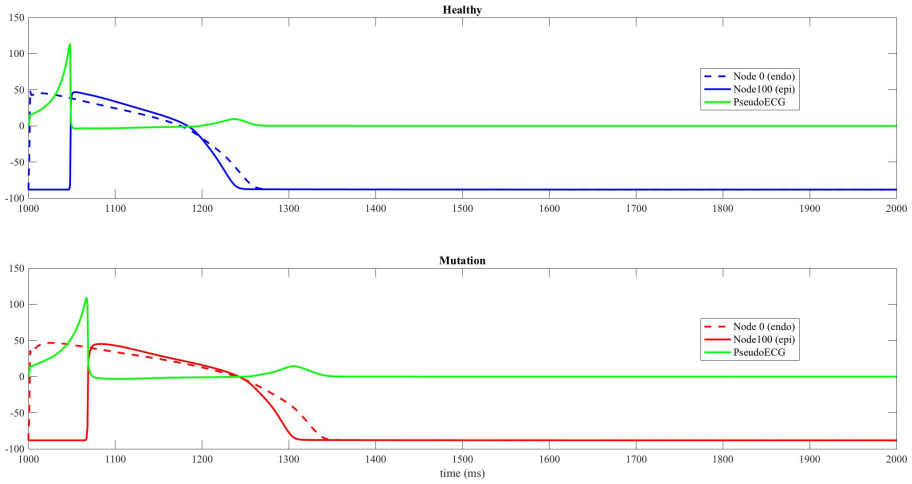

Figure A.18: The AP propagation and its corresponding *pseudoECG* when the T wave is positive. The first panel shows an healthy model and the second panel its corresponding mutation-carrier model.

A.18, Figure A.19 and Figure A.20 show the cellular mechanisms that underlie a positive, negative and biphasic T wave, respectively. Those figures compare the AP trace time course of the first and last nodes (i.e. endocardium and epicardium). The morphology of the T wave is determined by a combination of factors, including the differences in the AP duration, AP prolongation and delay in the $ActTime$ of the different cells. Figure A.21a shows how the TDR varies when the T wave

morphology changes. In particular, Figure A.21b highlights the TDR changes considering the overlap and non-overlap regions.

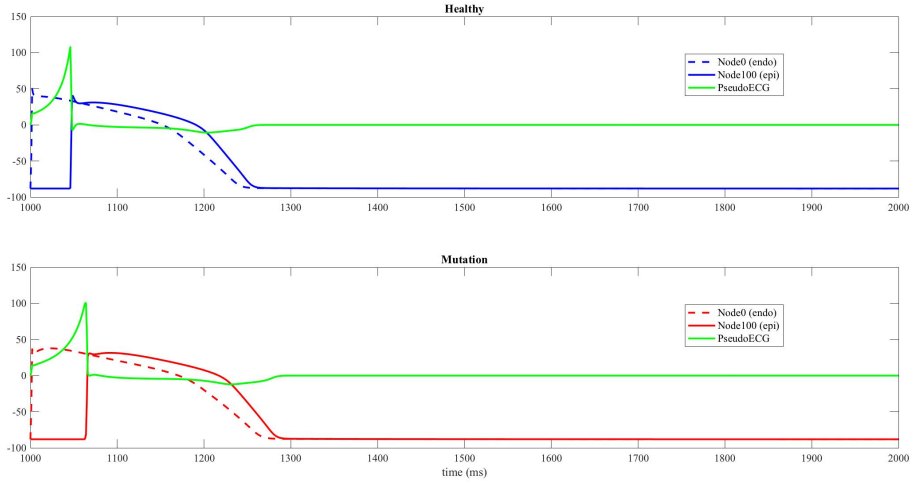

Figure A.19: The AP propagation and its corresponding $pseudoECG$ when the T wave is negative. The first panel shows an healthy model and the second panel its corresponding mutation-carrier model.

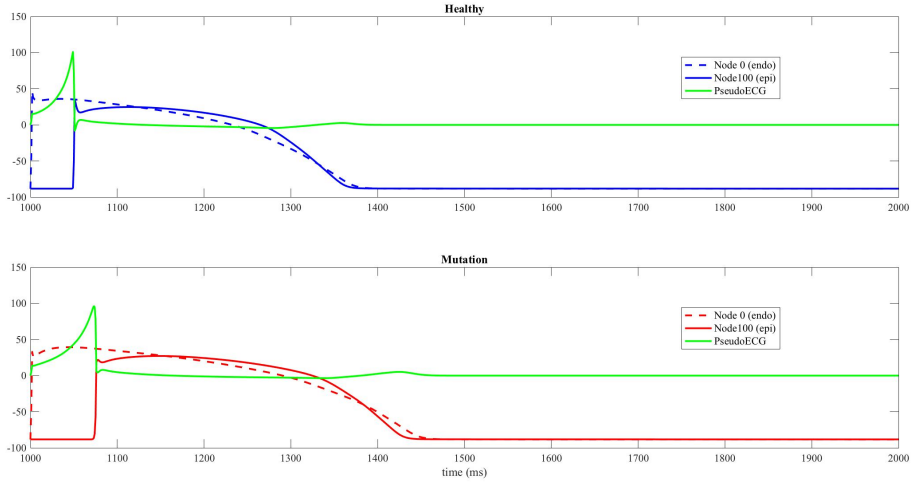

Figure A.20: The AP propagation and its corresponding $pseudoECG$ when the T wave is biphasic. The first panel shows an healthy model and the second panel its corresponding mutation-carrier model.

Models characterised by a negative T waves have a smaller TDR in the overlap region compared to the entire populations and for these models we don't see significant differences in the two conditions (healthy and mutation-carrier) in terms

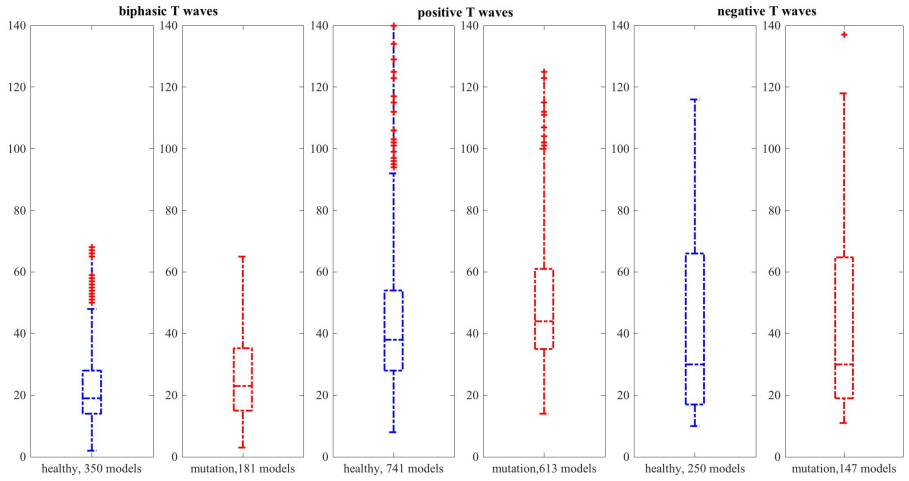

(a)

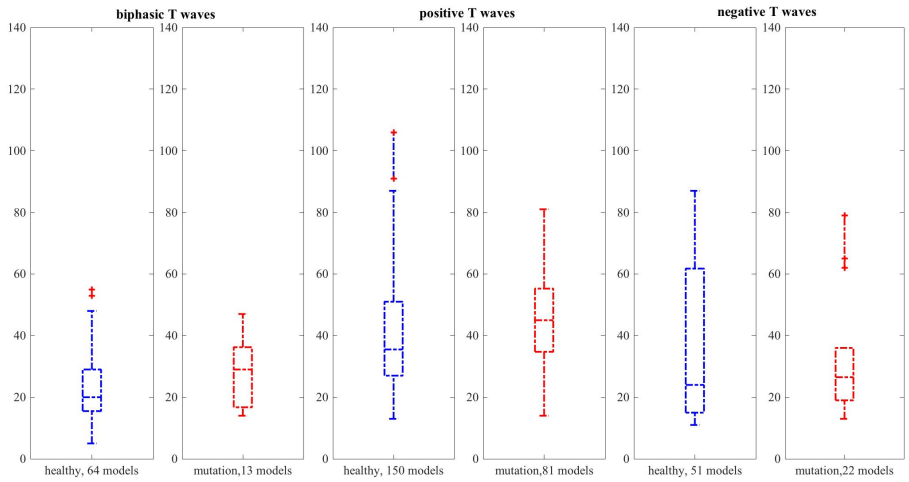

(b)

Figure A.21: How the morphology of the T wave affects the TDR. The first panel considers the entire populations, while the second one considers only those models in the overlap region.

of TDR. Models with positive or biphasic T waves show bigger TDR when the mutation is applied and moreover, these models show a bigger TDR when they belong to the overlap region. This result confirm that the TDR should be studied in clinical settings to provide further information on those potential patients that overlap with the healthy subjects.

Bibliography

[1] R A Bassani. Transient outward potassium current and ca2+ homeostasis in the heart: beyond the action potential. *Braz J Med Biol Res*, 39(3):393–403, Mar 2006.

[2] C Bezzina, M W Veldkamp, M P van Den Berg, A V Postma, M B Rook, J W Viersma, I M van Langen, G Tan-Sindhunata, M T Bink-Boelkens, A H van Der Hout, M M Mannens, and A A Wilde. A single na(+) channel mutation causing both long-qt and brugada syndromes. *Circ Res*, 85(12):1206–1213, Dec 1999.

[3] C R Bezzina, M B Rook, W A Groenewegen, L J Herfst, A C van der Wal, J Lam, H J Jongsma, A A M Wilde, and M M A M Mannens. Compound heterozygosity for mutations (w156x and r225w) in scn5a associated with severe cardiac conduction disturbances and degenerative changes in the conduction system. *Circ Res*, 92(2):159–168, Feb 2003.

[4] M Borggrefe and R Schimpf. J-wave syndromes caused by repolarization or depolarization mechanisms a debated issue among experimental and clinical electrophysiologists. *J Am Coll Cardiol*, 55(8):798–800, Feb 2010.

[5] O J Britton. *Combined experimental and computational investigation into inter-subject variability in cardiac electrophysiology*. PhD thesis, 2015.

[6] O J Britton, A Bueno-Orovio, K Van Ammel, H R Lu, R Towart, D J Gallacher, and B Rodriguez. Experimentally calibrated population of models predicts and explains intersubject variability in cardiac cellular electrophysiology. *Proc Natl Acad Sci U S A*, 110(23):E2098–105, Jun 2013.

[7] O J Britton, A Bueno-Orovio, L Virág, , A Varró, and B Rodriguez. The electrogenic na+/k+ pump is a key determinant of repolarization abnormality susceptibility in human ventricular cardiomyocytes: A population-based simulation study. *Frontiers in Physiology*, 8:278, 2017.

[8] O J Britton, A Bueno-Orovio, L Virag, A Varro, and B Rodriguez. Effect of inter-subject variability in determining response to ikr block in human ventricular myocytes. In *Computing in Cardiology 2014*, pages 869–872, 2014.

[9] C E Clancy and Y Rudy. Na(+) channel mutation that causes both brugada and long-qt syndrome phenotypes: a simulation study of mechanism. *Circulation*, 105(10):1208–1213, Mar 2002.

[10] R H Clayton, O Bernus, E M Cherry, H Dierckx, F H Fenton, L Mirabella, A V Panfilov, F B Sachse, G Seemann, and H Zhang. Models of cardiac tissue electrophysiology: progress, challenges and open questions. *Prog Biophys Mol Biol*, 104(1-3):22–48, Jan 2011.

[11] J Cooper, R J Spiteri, and G R Mirams. Cellular cardiac electrophysiology modeling with chaste and cellml. *Front Physiol*, 5:511, 2014.

[12] R Coronel, S Casini, T T Koopmann, F J G Wilms-Schopman, A O Verkerk, J R de Groot, Z Bhuiyan, C R Bezzina, M V Veldkamp, A C Linnenbank, A C van der Wal, H L Tan, P Brugada, A A M Wilde, and J M T de Bakker. Right ventricular fibrosis and conduction delay in a patient with clinical signs of brugada syndrome: a combined electrophysiological, genetic, histopathologic, and computational study. *Circulation*, 112(18):2769–2777, Nov 2005.

[13] R P Davis, S Casini, C W van den Berg, M Hoekstra, C A Remme, C Dambrot, D Salvatori, D W Oostwaard, A A M Wilde, C R Bezzina, A O Verkerk, C Freund, and C L Mummery. Cardiomyocytes derived from pluripotent stem cells recapitulate electrophysiological characteristics of an overlap syndrome of cardiac sodium channel disease. *Circulation*, 125(25):3079–3091, Jun 2012.

[14] G Dendramis, C Antzelevitch, P Brugada, C Paleologo, M S Baccillieri, and C De Asmundis. *Brugada Syndrome: Diagnosis, Clinical Manifestations, Risk Stratification and Treatment*. 12 2015.

[15] S Dutta, K C Chang, K A Beattie, J Sheng, P N Tran, W W Wu, M Wu, D G Strauss, T Colatsky, and Z Li. Optimization of an in silico cardiac cell model for proarrhythmia risk assessment. *Front Physiol*, 8:616, 2017.

[16] P C Franzone, L F Pavarino, and S Scacchi. *Mathematical Cardiac Electrophysiology*. Springer, 2014.

[17] A Frustaci, S G Priori, M Pieroni, C Chimenti, C Napolitano, I Rivolta, T Sanna, F Bellocci, and M A Russo. Cardiac histological substrate in patients with clinical phenotype of brugada syndrome. *Circulation*, 112(24):3680–3687, Dec 2005.

[18] K Gima and Y Rudy. Ionic current basis of electrocardiographic waveforms: a model study. *Circ Res*, 90(8):889–896, May 2002.

[19] E Grandi, F S Pasqualini, and D M Bers. A novel computational model of the human ventricular action potential and ca transient. *J Mol Cell Cardiol*, 48(1):112–121, Jan 2010.

[20] J J Hai, C K Wong, P H Chan, H F Tse, T C Yung, and C W Siu. Quinidine for brugada syndrome: Panacea or poison? *HeartRhythm Case Rep*, 2(6):486–490, Nov 2016.

[21] A L Hodgkin and A F Huxley. A quantitative description of membrane current and its application to conduction and excitation in nerve. *J Physiol*, 117(4):500–544, Aug 1952.

[22] M Hoekstra, C L Mummery, A A M Wilde, C R Bezzina, and A O Verkerk. Induced pluripotent stem cell derived cardiomyocytes as models for cardiac arrhythmias. *Front Physiol*, 3:346, 2012.

[23] Z Li, S Dutta, J Sheng, P N Tran, W Wu, K Chang, T Mdluli, D G Strauss, and T Colatsky. Improving the in silico assessment of proarrhythmia risk by combining herg (human ether-a-go-go-related gene) channel-drug binding kinetics and multichannel pharmacology. *Circ Arrhythm Electrophysiol*, 10(2):e004628, Feb 2017.

[24] Z Li, S Dutta, J Sheng, P N Tran, W Wu, and T Colatsky. A temperature-dependent in silico model of the human ether-a-go-go-related (herg) gene channel. *J Pharmacol Toxicol Methods*, 81:233–239, Sep-Oct 2016.

[25] C M Lloyd, M D B Halstead, and P F Nielsen. Cellml: its future, present and past. *Prog Biophys Mol Biol*, 85(2-3):433–450, Jun-Jul 2004.

[26] H R Lu, G X Yan, and D J Gallacher. A new biomarker–index of cardiac electrophysiological balance (iceb)–plays an important role in drug-induced cardiac arrhythmias: beyond qt-prolongation and torsades de pointes (tdps). *J Pharmacol Toxicol Methods*, 68(2):250–259, Sep-Oct 2013.

[27] D Malan, S Friedrichs, B K Fleischmann, and P Sasse. Cardiomyocytes obtained from induced pluripotent stem cells with long-qt syndrome 3 recapitulate typical disease-specific features in vitro. *Circ Res*, 109(8):841–847, Sep 2011.

[28] P Marinov, B Rodriguez, and A Bueno-Orovio. Rate dependence of the ina-ik1 complex on human ventricular conduction velocity under hypokalemia and hyperkalemia conditions. Computing in Cardiology, 2017.

[29] P G Meregalli, A A M Wilde, and H L Tan. Pathophysiological mechanisms of brugada syndrome: Depolarization disorder, repolarization disorder, or more? *Cardiovascular Research*, 67(3):367–378, 2005.

[30] A Minchole, E Pueyo, J F Rodriguez, E Zacur, M Doblare, and P Laguna. Quantification of restitution dispersion from the dynamic changes of the t-wave peak to end, measured at the surface ecg. *IEEE Trans Biomed Eng*, 58(5):1172–1182, May 2011.

[31] G R Mirams, C J Arthurs, M O Bernabeu, R Bordas, J Cooper, A Corrias, Y Davit, S J Dunn, A G Fletcher, D G Harvey, M E Marsh, James M Osborne, P Pathmanathan, J Pitt-Francis, J Southern, N Zemzemi, and D J Gavaghan. Chaste: an open source c++ library for computational physiology and biology. *PLoS Comput Biol*, 9(3):e1002970, 2013.

[32] Greg Moran. The heart. cardiology teaching package. a beginners guide to normal heart function, sinus rhythm, common cardiac arrhythmias.

[33] A Muszkiewicz, O J Britton, P Gemmell, E Passini, C Sanchez, X Zhou, A Carusi, T A Quinn, K Burrage, A Bueno-Orovio, and B Rodriguez. Variability in cardiac electrophysiology: Using experimentally-calibrated populations of models to move beyond the single virtual physiological human paradigm. *Prog Biophys Mol Biol*, 120(1-3):115–127, Jan 2016.

[34] H Nakaya. Scn5a mutations associated with overlap phenotype of long qt syndrome type 3 and brugada syndrome. *Circ J*, 78(5):1061–1062, 2014.

[35] D Noble. A modification of the hodgkin–huxley equations applicable to purkinje fibre action and pace-maker potentials. *J Physiol*, 160:317–352, Feb 1962.

[36] T O'Hara, L Virag, A Varro, and Y Rudy. Simulation of the undiseased human cardiac ventricular action potential: model formulation and experimental validation. *PLoS Comput Biol*, 7(5):e1002061, May 2011.

[37] O E Osadchii. Arrhythmogenic drugs can amplify spatial heterogeneities in the electrical restitution in perfused guinea-pig heart: An evidence from assessments of monophasic action potential durations and jt intervals. *PLoS One*, 13(1):e0191514, 2018.

[38] E Passini. *Computational Modelling of Cardiac Electrophysiology: from Cell to Bedside*. PhD thesis, University of Bologna, 2015.

[39] E Passini, A Minchole, R Coppini, E Cerbai, B Rodriguez, S Severi, and A Bueno-Orovio. Mechanisms of pro-arrhythmic abnormalities in ventricular repolarisation and anti-arrhythmic therapies in human hypertrophic cardiomyopathy. *J Mol Cell Cardiol*, 96:72–81, Jul 2016.

[40] P Pathmanathan, M O Bernabeu, R Bordas, J Cooper, A Garny, J M Pitt-Francis, J P Whiteley, and D J Gavaghan. A numerical guide to the solution of the bi-domain equations of cardiac electrophysiology. *Prog Biophys Mol Biol*, 102(2-3):136–155, Jun-Jul 2010.

[41] A R Perez-Riera, R Barbosa-Barros, R Daminello Raimundo, M P da Costa de Rezende Barbosa, I C Esposito Sorpreso, and L C de Abreu. The congenital long qt syndrome type 3: An update. *Indian Pacing Electrophysiol J*, Oct 2017.

[42] V Portero, S Casini, M Hoekstra, A O Verkerk, I Mengarelli, L Belardinelli, S Rajamani, A A M Wilde, C R Bezzina, M W Veldkamp, and C A Remme. Anti-arrhythmic potential of the late sodium current inhibitor gs-458967 in murine scn5a-1798insd+/- and human scn5a-1795insd+/- ipsc-derived cardiomyocytes. *Cardiovasc Res*, 113(7):829–838, Jun 2017.

[43] P G Postema, P M Van den Berg, J P Tintelen, F Van den Heuvel, M Grundeken, N Hofman, W van der Roest, E A Nannenberg, I Krapels, C Bezzina, and A A M Wilde. Founder mutations in the netherlands. 17:422–428, 11 2009.

[44] C A Remme. Cardiac sodium channelopathy associated with scn5a mutations: electrophysiological, molecular and genetic aspects. *J Physiol*, 591(17):4099–4116, Sep 2013.

[45] C A Remme, A O Verkerk, D Nuyens, A C G van Ginneken, S van Brunschot, C N W Belterman, R Wilders, M A van Roon, H L Tan, A A M Wilde, P Carmeliet, J M T de Bakker, M W Veldkamp, and Connie R Bezzina.

Overlap syndrome of cardiac sodium channel disease in mice carrying the equivalent mutation of human scn5a-1795insd. *Circulation*, 114(24):2584–2594, Dec 2006.

[46] C A Remme and A A M Wilde. Scn5a overlap syndromes: no end to disease complexity? *Europace*, 10(11):1253–1255, Nov 2008.

[47] C A Remme, A A M Wilde, and C R Bezzina. Cardiac sodium channel overlap syndromes: different faces of scn5a mutations. *Trends Cardiovasc Med*, 18(3):78–87, Apr 2008.

[48] T Robyns, H R Lu, D J Gallacher, C Garweg, J Ector, R Willems, S Janssens, and D Nuyens. Evaluation of index of cardio-electrophysiological balance (iceb) as a new biomarker for the identification of patients at increased arrhythmic risk. *Ann Noninvasive Electrocardiol*, 21(3):294–304, May 2016.

[49] A Royer, T A B van Veen, S Le Bouter, C Marionneau, V Griol-Charhbili, A L Leoni, M Steenman, H V M van Rijen, S Demolombe, C A Goddard, C Richer, B Escoubet, T Jarry-Guichard, W H Colledge, D Gros, J M T de Bakker, A A Grace, D Escande, and F Charpentier. Mouse model of scn5a-linked hereditary lenegre's disease: age-related conduction slowing and myocardial fibrosis. *Circulation*, 111(14):1738–1746, Apr 2005.

[50] J Sieira, G Dendramis, and P Brugada. Pathogenesis and management of brugada syndrome. *Nat Rev Cardiol*, 13(12):744–756, Dec 2016.

[51] P Taggart, M Orini, B Hanson, M Hayward, R Clayton, H Dobrzynski, J Yanni, M Boyett, and P D Lambiase. Developing a novel comprehensive framework for the investigation of cellular and whole heart electrophysiology in the in situ human heart: historical perspectives, current progress and future prospects. *Prog Biophys Mol Biol*, 115(2-3):252–260, Aug 2014.

[52] P Taggart, P Sutton, Z Chalabi, M R Boyett, R Simon, D Elliott, and J S Gill. Effect of adrenergic stimulation on action potential duration restitution in humans. *Circulation*, 107(2):285–289, Jan 2003.

[53] P Taggart, P M Sutton, T Opthof, R Coronel, R Trimlett, W Pugsley, and P Kallis. Transmural repolarisation in the left ventricle in humans during normoxia and ischaemia. *Cardiovasc Res*, 50(3):454–462, Jun 2001.

[54] K H W J ten Tusscher, D Noble, P J Noble, and A V Panfilov. A model for human ventricular tissue. *Am J Physiol Heart Circ Physiol*, 286(4):H1573–89, Apr 2004.

[55] K H W J ten Tusscher and A V Panfilov. Alternans and spiral breakup in a human ventricular tissue model. *Am J Physiol Heart Circ Physiol*, 291(3):H1088–100, Sep 2006.

[56] C Terrenoire, K Wang, K W C Tung, W K Chung, R H Pass, J T Lu, J C Jean, A Omari, K J Sampson, D N Kotton, G Keller, and R S Kass. Induced pluripotent stem cells used to reveal drug actions in a long qt syndrome family with complex genetics. *J Gen Physiol*, 141(1):61–72, Jan 2013.

[57] G Tse, M Gong, W T Wong, S Georgopoulos, K P Letsas, V S Vassiliou, Y S Chan, B P Yan, S H Wong, W K K Wu, A Ciobanu, G Li, J Shenthar, A M Saguner, S Ali-Hasan-Al-Saegh, A Bhardwaj, A C Sawant, P Whittaker, Y Xia, G X Yan, and T Liu. The tpeak - tend interval as an electrocardiographic risk marker of arrhythmic and mortality outcomes: A systematic review and meta-analysis. *Heart Rhythm*, 14(8):1131–1137, Aug 2017.

[58] M P van den Berg, J W Viersma, G C M Beaufort-Krol, M T E Bink-Boelkens, C R Bezzina, M W Veldkamp, J Brouwer, J Haaksma, J P van Tintelen, I M van Langen, A A Wouda, and A A M Wilde. A large family characterised by nocturnal sudden death. *Neth Heart J*, 10(7-8):304–312, Aug 2002.

[59] M P van den Berg, A A Wilde, T J W Viersma, J Brouwer, J Haaksma, A H van der Hout, I Stolte-Dijkstra, T C R Bezzina, I M Van Langen, G C Beaufort-Krol, J H Cornel, and H J Crijns. Possible bradycardic mode of death and successful pacemaker treatment in a large family with features of long qt syndrome type 3 and brugada syndrome. *J Cardiovasc Electrophysiol*, 12(6):630–636, Jun 2001.

[60] C C Veerman, A A M Wilde, and E M Lodder. The cardiac sodium channel gene scn5a and its gene product nav1.5: Role in physiology and pathophysiology. *Gene*, 573(2):177–187, Dec 2015.

[61] M W Veldkamp, P C Viswanathan, C Bezzina, A Baartscheer, A A Wilde, and J R Balser. Two distinct congenital arrhythmias evoked by a multidysfunctional na(+) channel. *Circ Res*, 86(9):E91–7, May 2000.

[62] P C Viswanathan and J R Balser. Inherited sodium channelopathies: a continuum of channel dysfunction. *Trends Cardiovasc Med*, 14(1):28–35, Jan 2004.

[63] A A M Wilde, C Antzelevitch, M Borggrefe, J Brugada, R Brugada, P Brugada, D Corrado, R N W Hauer, R S Kass, K Nademanee, S G Priori, and J A Towbin. Proposed diagnostic criteria for the brugada syndrome: consensus report. *Circulation*, 106(19):2514–2519, Nov 2002.

[64] G X Yan and C Antzelevitch. Cellular basis for the brugada syndrome and other mechanisms of arrhythmogenesis associated with st-segment elevation. *Circulation*, 100(15):1660–1666, Oct 1999.

[65] J Zhang, F Sacher, K Hoffmayer, T O'Hara, M Strom, P Cuculich, J Silva, D Cooper, M Faddis, M Hocini, M Haissaguerre, M Scheinman, and Y Rudy. Cardiac electrophysiological substrate underlying the ecg phenotype and electrogram abnormalities in brugada syndrome patients. *Circulation*, 131(22):1950–1959, Jun 2015.

[66] T Zhang, S L Yong, J K Drinko, Z B Popovic, J C Shryock, L Belardinelli, and Q K Wang. Lqts mutation n1325s in cardiac sodium channel gene scn5a causes cardiomyocyte apoptosis, cardiac fibrosis and contractile dysfunction in mice. *Int J Cardiol*, 147(2):239–245, Mar 2011.

[67] X Zhou, A Bueno-Orovio, M Orini, B Hanson, M Hayward, P Taggart, P D Lambiase, K Burrage, and B Rodriguez. In vivo and in silico investigation into mechanisms of frequency dependence of repolarization alternans in human ventricular cardiomyocytes. *Circ Res*, 118(2):266–278, Jan 2016.

...Grazie ai miei genitori, anche se un grazie non potrebbe mai bastare. Grazie alla dolcezza e infinita saggezza della mia mamma, grazie al mio papà che mi fa sentire al sicuro e protetta da tutto. Alle mie sorelle che mi hanno insegnato cosa significhi amare qualcuno più di se stessi. Grazie ad Andrea che con infinito amore mi supporta e sopporta da sempre ormai, grazie perché guardiamo nella stessa direzione. Grazie a te lassù, spero tu sia orgoglioso di me.